

# SCIENTIFIC RESEARCH LABORATORIES

AD695492

## Corrosion of Servo Valves by an Electrokinetic Streaming Current

T. R. Beck

D. W. Mahaffey

J. H. Olsen

This document has been approved  
for public release and its  
distribution is unlimited.

D D C  
OCT 29 1969  
150

D1-82-0839

CORROSION OF SERVO VALVES BY AN ELECTROKINETIC  
STREAMING CURRENT

By

T. R. Beck,<sup>\*</sup> D. W. Mahaffey,<sup>\*\*</sup> and J. H. Olsen<sup>†</sup>

<sup>\*</sup>Solid State Physics Laboratory

<sup>\*\*</sup>Plasma Physics Laboratory

<sup>†</sup>Flight Sciences Laboratory

Boeing Scientific Research Laboratories  
Seattle, Washington

September 1969

CORROSION OF SERVO VALVES BY AN ELECTROKINETIC  
STREAMING CURRENT

By

T. R. Beck, D. W. Mahaffey and J. H. Olsen

ABSTRACT

Corrosion driven by electrokinetic currents was found to be responsible for damage to steel servo valves operating in phosphate ester fluids. Calculations and test results supporting this conclusion and measurements of the electrokinetic and electrochemical properties of the steel to fluid interface are described. Possible fluid additives for reducing the damage are discussed.

TABLE OF CONTENTS

1.0	Introduction
2.0	Summary
3.0	Conclusions
4.0	Recommendations
5.0	Cavitation
5.1	Bubble Collapse Mechanism
5.2	Experiments
5.3	Conclusions
6.0	Particle Erosion
7.0	Streaming Current
7.1	Theory of Streaming Current Production
7.1.1	Flow in a Tube
7.1.2	Accelerating Flow
7.1.3	The Hydrodynamic Solution
7.2	Experiment
7.2.1	Klinkenberg Apparatus
7.2.2	Wall Current Measurements with Phosphate Ester Fluids
7.2.3	Wall Current Measurements with Other Fluids
7.3	Conclusions
8.0	Conductivity of Fluids
8.1	Experiments
8.2	Theory
8.3	Conclusions
9.0	Electrochemistry in Phosphate Ester Fluids
9.1	Parallel-Electrode Cell Experiments
9.2	Needle-to-Plane Cell Corrosion Experiments
9.3	Anode Polarization in Phosphate Ester Fluids
9.4	Conclusions
10.0	Coupled Streaming Current and Spark Discharge

## 11.0 Coupled Streaming Current and Corrosion

- 11.1 High Pressure Flow Experiments
  - 11.1.1 Disk to Ring Current
  - 11.1.2 Cathodic Protection
  - 11.1.3 Insulating Specimen
- 11.2 Comparison of Theory and Experiment
  - 11.2.1 Comparison of Actual Metal Removal to Theory
  - 11.2.2 Flow Damage in Various Fluids
- 11.3 The Effect of Water Addition
- 11.4 Electrochemical Mechanism of Corrosion
- 11.5 Conclusions

## 12.0 Acknowledgment

## 13.0 References

## 14.0 Appendix

- 14.1 Nomenclature
- 14.2 Errors in the Theory due to Fluid Conductivity
- 14.3 Diffusivity of Charge Carriers in Phosphate Ester Fluids
- 14.4 Electrolyte Resistance in Cells
- 14.5 Measurement of Corrosion Profile from 28 1/2 Hour Run
- 14.6 Electrode Film Resistivity and Growth Rate
- 14.7 High Pressure Flow System

## 1.0 INTRODUCTION

Since about 1965 a problem of rapid and severe damage has been observed in the valves of some hydraulic systems using synthetic phosphate ester based hydraulic fluids. Some of the systems suffering from this problem are General Electric control systems for steam turbines [1], and the hydraulic systems of Hawker Siddeley Trident [2] and Boeing airplanes [3]. U. S. military airplanes which use MIL-H-5606, a hydrocarbon mixture, have not experienced severe damage. However, MIL-H-5606 is not used in commercial aircraft because of its greater flammability.

Figure 1-1a is a schematic of an airplane slide and sleeve servo valve. In Boeing airplanes such valves are typically made from hardened steel. In operation the pressure drop across the metering edge is from about 3000 psi upstream to about 300 psi downstream and in the nominally closed position there is a hydraulic fluid flow rate of about 100 cc per minute through the metering orifices formed by the clearance between the slide and sleeve. Damage occurs at and just upstream of the metering edges. Figure 1-1b is a photograph of a damaged area on a Boeing 737 flap valve and Fig. 1-1c is an enlargement of this area. This damage causes an increasingly large closed position flow rate which may ultimately reach the hydraulic system pump capacity.

Cavitation, particle erosion, electrical discharge machining and corrosion of the metal surface had been variously suggested as causes of the damage. Electrokinetic potentials had previously been measured in flowing phosphate ester hydraulic fluids, but their connection with valve damage was unexplained. It had been observed that the damage could be

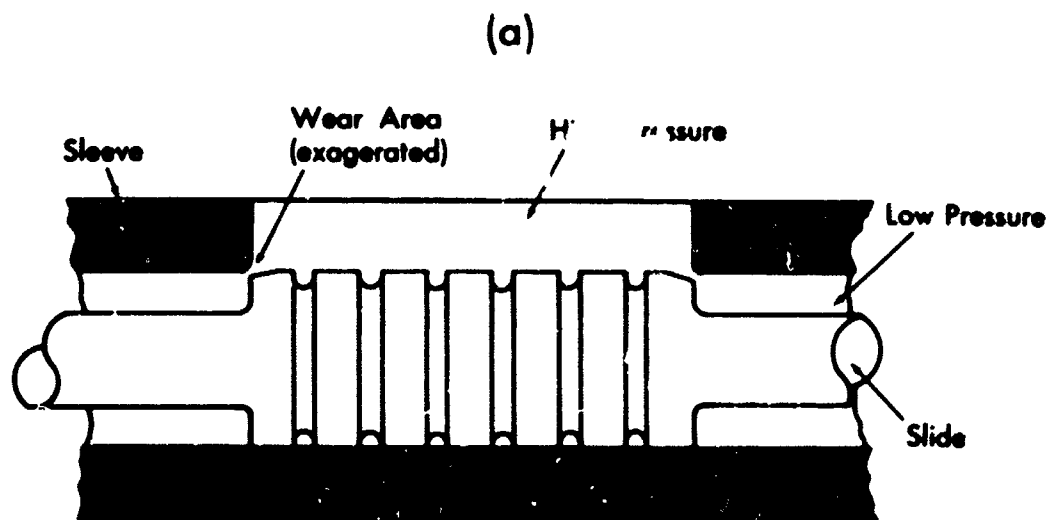


Fig. 1-1. a) Valve schematic; b) damaged areas on slide; c) enlargement of damaged area.

reduced by treating the fluid by filtration through fuller's earth [1] or by addition of water [2]. The fuller's earth treatment was thought to remove ions affecting corrosion and the water addition was thought to influence cavitation through vapor pressure changes. None of these suggestions could explain all the observed data.

This document reports the results of an investigation which was undertaken to determine the damage mechanism and to provide background information which may assist in elimination of the damage. A brief summary of the investigation is given in Sec. 2 and the most important conclusions concerning the damage mechanism are listed in Sec. 3 and recommendations for eliminating the damage are given in Sec. 4. Sections 5 through 11 contain detailed descriptions of the investigation. Supplementary data and calculations are provided in the appendices.



## 2.0 SUMMARY

A laboratory system was developed which simulated the flow conditions in hydraulic valves. The flow rate and geometry of the system was accurately reproducible. Damage identical in appearance to that in the valves was produced. Increasing the back pressure while maintaining constant flow eliminated cavitation but not damage. This proved that cavitation was not the primary damage mechanism. Experiments using a one-micron membrane filter to remove foreign particles indicated that particle erosion was not the primary process as the presence of this filter did not stop the damage. Optical observations and measurements with a small electrode inserted in the wall at the orifice failed to show the presence of sparks. However, a small steady current was observed flowing from the electrode. This current normal to the wall, herein termed the wall current, is produced by the generation of an electrical streaming current in an accelerating fluid flow, and causes electrochemical corrosion damage of the metal. The wall current was quantitatively accounted for from measured values of the electrical properties of the fluid and a calculation involving hydrodynamic and electrokinetic theory.

Supporting evidence for this corrosion mechanism includes the following observations: The current measured from an electrode in the wear area is more than sufficient to account for the amount of metal removed by electrochemical corrosion; damage could be eliminated on the specimen through the application of an electrical current from an external source to cancel that produced by the flow; an insulating aluminum oxide specimen, which should not be subject to electrochemical pitting corrosion, was not damaged even under cavitating conditions; the damage observed with various

hydraulic fluids was related to their electrical properties; corrosion damage similar to that in valves was obtained electrochemically without fluid flow.

During the course of the investigation a considerable body of supplemental information pertinent to the problem was obtained. A white insulating film was observed on both the anode and cathode of an electrochemical cell and near the orifice in the flow experiments. The thickness of the film increased with increasing water content. This may be an important factor in the reduction of damage when water is added to the fluid because the film formation affects the flow rate of the fluid and may affect the flow of electrical current from the metal. The electrical conductivity of the hydraulic fluid affects the amount of damage observed. It is believed that either a substantial increase or a substantial decrease in conductivity would significantly decrease the amount of damage. Experiments and analysis suggest that the conductivity of the fluid is due to hydrolysis products. These products may contribute to the generation of the streaming current. Filtration through fuller's earth is believed to remove these hydrolysis products. Some experiments were performed to determine the effect of changes in fluid composition on streaming current and electrochemical properties. The results of these experiments were consistent with the proposed damage mechanism.

### 3.0 CONCLUSIONS

1. The damage to airplane hydraulic system valves using phosphate ester fluids is primarily due to corrosion driven by electrical currents caused by the fluid flow.
2. Cavitation plays a minor role, if any.
3. Particle erosion if present plays a secondary role.
4. Electrical discharge machining is not a primary damage mechanism.
5. The magnitude and location of the electrical currents can be predicted for various fluids by means of an equation relating the fluid properties, and the hydrodynamic and electrokinetic conditions.
6. The amount of corrosion produced by the current is a function of fluid composition because some species in the fluid may react more readily than the steel valve.
7. The advantages of water addition for corrosion reduction must be balanced against the disadvantage of increased film formation.
8. The damage is a consequence of a chain of events enumerated above, and may be eliminated by breaking the chain at any one of its links.

#### 4.0 RECOMMENDATIONS

The mechanism of the valve damage has been identified, which completes the experimental investigation at BSRL, but workable solutions remain to be found that are compatible with the whole hydraulic system.

The primary recommendation is that modifications be made to the hydraulic fluid rather than to the valve geometry or material, because other requirements on the valves preclude this approach. Moreover, hydraulic fluids already exist which do not cause electrochemical pitting corrosion. On this basis, the following specific recommendations are made:

1. Develop new specifications for hydraulic fluids regarding tolerances for streaming current and wall current.
2. Use BSRL developed instruments to screen new fluids and the effect of additives or treatments. These instruments are
  - a) Wall current measuring device (Sec. 7.2)
  - b) Needle-to-plane electrochemical cell (Sec. 9.2)
  - c) Wear test apparatus (Sec. 5.2)
3. Re-evaluate selection of hydraulic fluid for new airplane fleets considering the damage and deposit mechanisms described in this report.
4. For the existing commercial fleet already committed to phosphate ester based fluids evaluate the following possible cures:
  - a) Removal of chlorine containing compounds (Sec. 9.2)
  - b) Addition of conducting ionic species (Secs. 8.2 and 14.2)
  - c) Increase of fluid stability to hydrolysis (Sec. 8.2)

- d) In addition to (c) investigation of agents more effective than fuller's earth to remove hydrolysis products
- e) Addition of neutral surfactants (Sec. 7.2)
- f) Addition of reversible redox couples (Sec. 9.2).

## 5.0 CAVITATION

Cavitation is the formation of vapor cavities in a flowing liquid at points where the pressure falls below the vapor pressure of the liquid. Cavitation occurs in hydraulic valves used in airplanes, but it does not necessarily cause damage. Damage from cavitation is thought to be the result of high stresses caused by violent collapse of vapor bubbles as they enter a region of high pressure. The stresses are determined by the details of the bubble collapse.

### 5.1 Bubble Collapse Mechanism

The final stresses produced by a collapsing bubble depend on the fluid properties, the initial bubble size, and the pressure of the surrounding liquid. Among other parameters, the ratio of viscous forces to pressure forces is important. It is expressed as [4]

$$C = \frac{4\nu}{R_0 \sqrt{\frac{(P_\infty - P_0)}{\rho}}} \quad 5-1$$

where  $\rho$  is the liquid density,  $\nu$  the kinematic viscosity,  $R_0$  the initial radius, and  $(P_\infty - P_0)$  the difference between the liquid pressure and the pressure within the bubble.

S. S. Shu [4] has shown that for  $C > .46$  the viscous forces are dominant and cause the collapse to require an infinite time. Under these circumstances no high stresses occur.

A minimum value for  $C$  can be estimated for a valve operating with phosphate ester fluids. The maximum value for  $R_0$  is about 5 microns because the bubble must fit in the clearance between the slide and sleeve

(Fig. 1-1a). The largest available pressure downstream of the minimum pressure point to drive the collapse is 300 psi. The density and kinematic viscosity of phosphate ester fluids are 1g/cc and .1cm<sup>2</sup>/sec respectively. The computed value of C is then .2. This is close enough to the critical value of .46 that viscous forces may significantly cushion the peak collapse pressures. These large viscous forces may prevent cavitation damage to the valves and explain the lack of cavitation damage in the cavitating flow experiment described below.

## 5.2 Experiments

The apparatus shown in Fig. 5-1 was constructed to simulate the constricted flow in a valve and yet produce damage on a polished flat plate for easy observation. The blocks were made of 52100 steel hardened to R<sub>c</sub> 62. The metering area was determined by the size of the inlet hole and the .001" mylar gasket between the blocks. The flow for these and all other high pressure flow experiments was provided by the pumping system described in Appendix 14.7.

Flow in the absence of cavitation was obtained by raising the pressure level of the flow until the lowest pressure at any point in the flow was greater than the vapor pressure of the liquid. The above apparatus was operated with Skydrol<sup>\*</sup> 500A with 7000 psi upstream of the lip and 4300 psi downstream for a period of 2 1/2 hours. The absence of cavitation was verified by the absence of sound output to a microphone at back pressures greater than 1000 psi.

---

\* A phosphate ester fluid manufactured by the Monsanto Chemical Company.

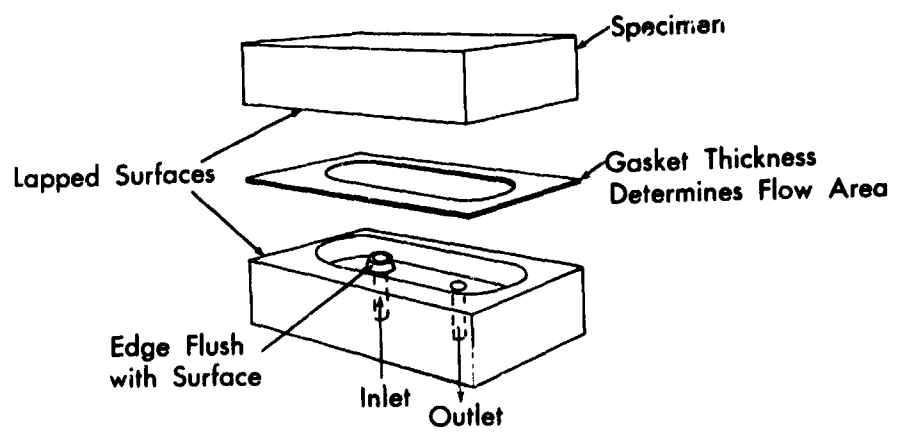


Fig. 5-1. Damage test apparatus.



The damage produced on the flat plate in the absence of cavitation is shown in Fig. 5-2. The positions of the edges of the metering lip are superimposed on the photo to show the damage location relative to the lip. All damage occurred upstream of or just within the orifice, whereas cavitation wear must occur downstream of the minimum pressure point in the region of collapsing bubbles. In a second experiment with strong cavitation noise at a pressure drop from 3000 to 50 psi, no increase in damage rate was observed either upstream or downstream of the orifice.

### 5.3 Conclusions

In the above experiment cavitation damage, if any, is insignificant compared to damage from other mechanisms. Viscous damping of the bubble collapse is the mechanism thought to prevent damage.



Fig. 5-2. a) Damage on plate with lip position outlined.  
b) Enlargement of damaged area.

## 6.0 PARTICLE EROSION

Erosion by bombardment with solid particles is a well known phenomenon and is used in sandblasting processes. Airplane hydraulic systems are equipped with filters, but a small amount of particle contamination still circulates with the fluid. Usual aircraft filters are bulk filters which catch particles in a fiber mat. Much finer filtration can be achieved in the laboratory with a membrane filter which catches particles on the surface of a membrane of known pore size. A one-micron membrane filter placed immediately upstream of the apparatus of Fig. 5-1 caused no observable decrease in damage rate. Particle erosion was, therefore, not considered further during the search for the damage mechanism.

## 7.0 STREAMING CURRENT

### 7.1 Theory of Streaming Current Production

Consider the electrical effects at a metal surface in a motionless fluid. Three locations of interest are illustrated in Fig. 7-1. They are: the metal surface,  $M$ ; the center of a layer of ions from the fluid bound to the metal,  $O$ ; and the outer edge of a diffuse charge layer,  $\delta$ . The diffuse and bound charges are referred to as an electrical double layer [5]. The net charge at  $O$  results from two effects. First, the positive and negative ions in the fluid will, in general, differ in their adsorption on the metal resulting in a net charge (negative in Fig. 7-1) bound to the surface by chemical or Van der Waal's forces. Second, any charges within the metal (positive in Fig. 7-1) can shift the equilibrium of the adsorption through electrostatic forces. The total charge at the surface (sum of charges at  $O$  and  $M$ ) creates an electric field to draw charges of the opposite sign (positive in Fig. 7-1) from the bulk of the fluid toward the surface. At the same time molecular diffusion tends to spread these charges evenly throughout the fluid. The balance between electrical conduction and diffusion determines the thickness,  $\delta$ , of the resulting exponential distribution of free charge in the diffuse outer portion of the double layer.

A fluid motion parallel to the wall sweeps the free charges of the diffuse layer downstream resulting in a current, the streaming current. The charges at  $O$  remain bound to the wall. The electrical double layer is usually very thin (several hundred Angstroms in phosphate ester hydraulic fluids) compared to a hydrodynamic boundary layer so that the velocity profile causing the current may be regarded as linear in  $y$ . If we

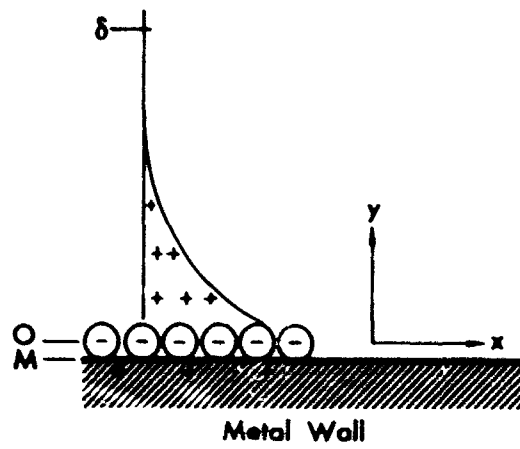


Fig. 7-1. Important levels in the electrical double layer.

consider a parallel shear flow over an infinite flat metal plate, the current density parallel to the plate is given by

$$J = \rho Ky \quad 7-1$$

where  $Ky$  is the fluid velocity. The charge density,  $\rho$ , is related to the potential,  $\phi$ , in the thin double layer by Poisson's equation

$$\frac{\partial^2 \phi}{\partial y^2} = - \frac{\rho}{\epsilon \epsilon_0} \quad 7-2$$

Combining Eqs. 7-1 and 7-2 and integrating by parts from the bound charge layer to  $\delta$  where  $\phi$  becomes constant in  $y$ , the current per unit length flowing in the thin layer on the plate is found to be

$$J_s = \int_0^{\delta} J dy = \epsilon \epsilon_0 K (\phi_{\delta} - \phi_0) = \epsilon \epsilon_0 \zeta K \quad 7-3$$

The result 7-3 is independent of the particular charge profile in the double layer and depends only on the potential difference,  $\zeta$ , between the bound charge layer at 0, and the fluid outside the double layer.

#### 7.1.1 Flow in a Tube

For low velocity flow in a uniform circular tube,  $K$ , is related to the tube dimensions and the pressure drop by

$$K = \frac{a \Delta P}{2 \eta l} \quad 7-4$$

where  $a$  is the radius of the tube,  $l$  is the length,  $\eta$  is the dynamic viscosity of the liquid and  $\Delta P$  is the pressure difference between the ends of the tube.

The total streaming current,  $I_s$ , is given by the  $J_s$  times the tube circumference

$$I_s = \frac{\pi a^2 \Delta P}{\eta l} \epsilon \epsilon_0 \zeta \quad 7-5$$

This result was given by Klinkenberg [5] and is used to calculate  $\zeta$  from the results of the simple flow experiment described in Sec. 7.2.1.

### 7.1.2 Accelerating Flow

Now, suppose that the flow is not a parallel shear flow, but that  $K$  is a function of position due to fluid acceleration. If the length scale for the variations in  $K$  is much larger than the double layer thickness, the above relations can be used to relate local values of the parameters, and  $J_s$  can be regarded as a surface current flowing in a thin sheet. However, conservation of charge requires that a divergence of the surface current be compensated by a current flow normal to the surface from either the fluid,  $J_f$ , or the metal wall,  $J_w$ , or both. If  $K$  varies only with  $x$  as in Fig. 7-2

$$J_w - J_f = \frac{\partial J_s}{\partial x} = \epsilon \epsilon_0 \zeta \frac{\partial K}{\partial x} \quad 7-6$$

Here,  $\zeta$  has been assumed constant. The assumption should be a good approximation for low velocities and current measurements described later suggest that it is valid at high velocities.

The wall current density,  $J_w$ , causes electrochemical reactions at the interface, one of which could be corrosion of the metal (e.g.  $\text{Fe} \rightarrow \text{Fe}^{++} + 2e^-$ ). The resistance to the flow of  $J_w$  depends on the reaction kinetics at the metal and the resistance of any deposited films (see 14.2, 14.6). The resistance to  $J_f$  depends on the fluid conductivity.

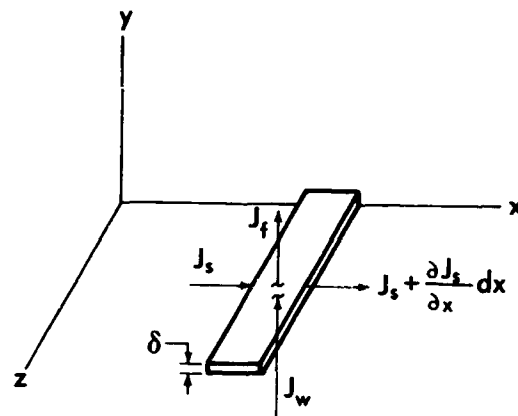


Fig. 7-2. Relation between surface currents and normal currents.



If the conductivity is sufficiently low,  $J_f$  will be negligible. We will calculate  $J_w$  on this basis. The current density  $J_w$  is then

$$J_w = \epsilon \epsilon_0 \zeta \frac{\partial K}{\partial x} \quad 7-7$$

where  $K$  is obtained from the hydrodynamic solution. The influence of fluid conductivity is discussed in Appendix 14.2.

### 7.1.3 The Hydrodynamic Solution

As indicated in Fig. 1-1a, the slide diameter is much larger than the orifice formed by the clearance between the slide and sleeve. The flow can, therefore, be approximated by a two-dimensional flow in a  $90^\circ$  converging channel (Fig. 7-3). Fortunately, one of the few exact solutions to the Navier-Stokes equations is for this problem. The problem was solved by Jeffrey [6] and independently by Hamel [7]. In the solution as formulated by Millsaps and Pohlhausen [8] the velocity is given by

$$v = \frac{v}{r} F(\theta) \quad 7-8$$

where  $F(\theta)$  is expressed in terms of elliptic functions. The wall shear is

$$K = \left. \frac{1}{r} \frac{\partial v}{\partial \theta} \right|_0 = \frac{v}{r^2} F'(0) \quad 7-9$$

$F'(0)$  and the Reynolds number based on the flow per unit length of sink were calculated from solutions for various channel centerline velocities in a  $90^\circ$  channel using the formulation of Millsaps and Pohlhausen. The relation between  $F'(0)$  and Reynolds number is shown in Fig. 7-4. The relation

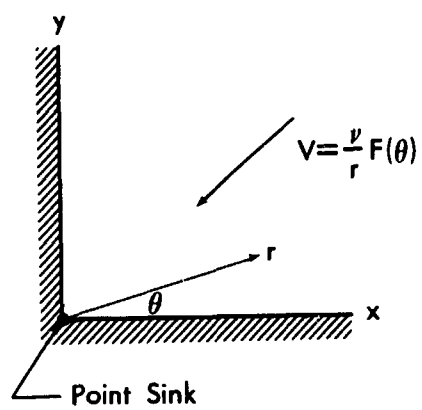


Fig. 7-3. The hydrodynamic flow field.

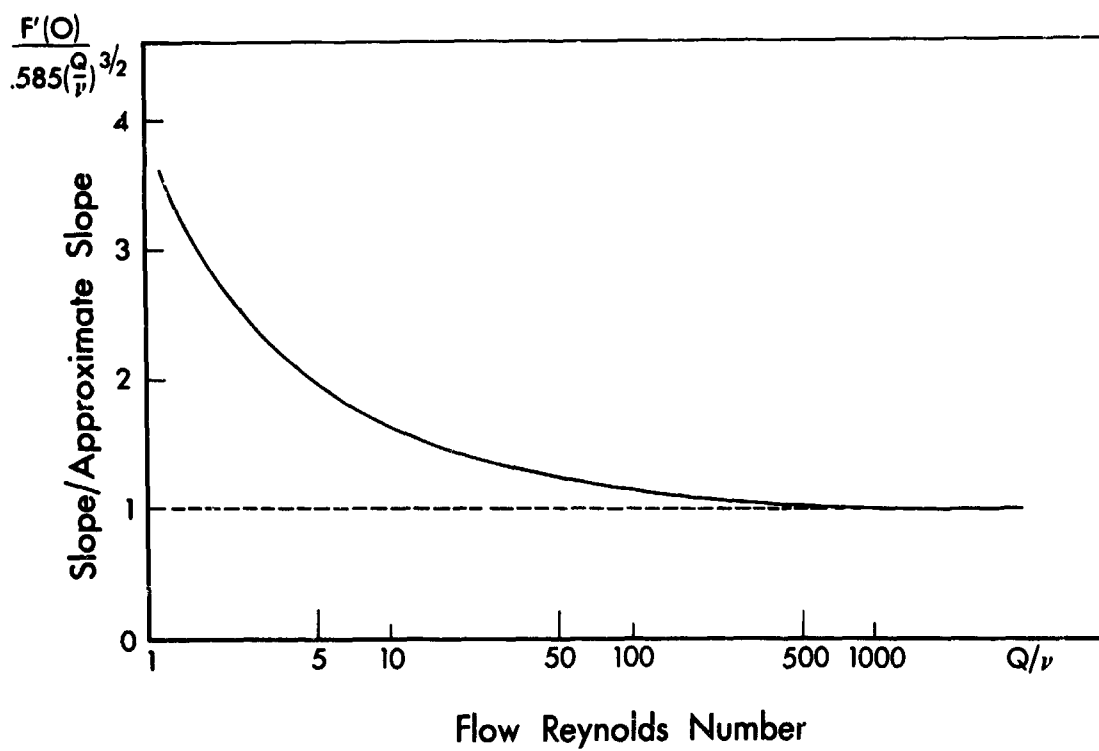


Fig. 7-4. Wall shear as a function of Reynolds number.

$$F'(0) = .585 \left( \frac{Q}{v} \right)^{3/2} \quad 7-10$$

is seen to be a good approximation at large Reynolds numbers.

Equations 7-8 and 7-9 are valid far from the orifice and become poor approximations at the orifice. We would expect the shear to follow Eq. 7-9 to the neighborhood of the orifice and then level off and decrease within the orifice where the accelerations are less severe.

#### The Wall Current Density\*

At the metal surface  $\cos\theta = 1$ , and the  $r$  appearing in Eq. 7-9 is equal to  $x$  so that Eqs. 7-7, 7-9 and 7-10 can be combined to give the current density as a function of sink strength,  $Q$ , and distance,  $x$ , from the sink.

$$J_w = \frac{1.17\epsilon\epsilon_0\zeta v}{x^3} \left( \frac{Q}{v} \right)^{3/2} \quad 7-11$$

$J_w$  is the wall current density flowing from the metal to 0 (Fig. 7-1) causing the corrosion.

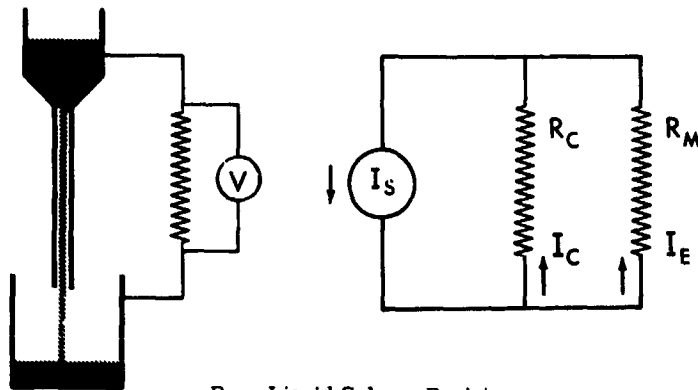
## 7.2 Experiment

### 7.2.1 Klinkenberg Apparatus

Measurements were made of the streaming current  $I_s$  (Eq. 7-5) in various hydraulic fluids. From these measurements the value of the significant parameter  $\epsilon\zeta$  can be determined from Eq. 7-5. The apparatus, after Klinkenberg [5], used for the measurement of  $I_s$  and its equivalent circuit is illustrated in Fig. 7-5.

---

\* Levich [9] presents a related treatment for surface current density generated by mercury amalgam drops falling through an electrolyte.



$R_C$  = Liquid Column Resistance

$R_M$  = Meter Input Resistance

$I_S$  = Streaming Current

$I_C$  = Conduction Current Up  
Liquid Column

$I_E$  = Measured Current

$$\begin{aligned} \text{and} \quad I_S &= I_E + I_C \\ I_C R_C &= I_E R_M \\ I_S &= I_E \left( 1 + \frac{R_M}{R_C} \right) \end{aligned}$$

Fig. 7-5. a) Klinkenberg apparatus for measuring streaming current.  
b) Equivalent circuit.

The upper and lower cans, each of two liter capacity were made of stainless steel as was a 50 cm long, 3 mm i.d. tube welded to the upper can. The liquid under test was stored in the upper can for a sufficiently long time to allow any electrical charges to leak to ground. The liquid was then permitted to fall under gravity into the lower can and the streaming current was measured using a Keithley 610A electrometer. This meter has a high input impedance which affects the total current flowing in the circuit, as illustrated in Fig. 7-5. By making measurements on two ranges of the meter having different input resistances  $R_m$ , and using the equation at the bottom of Fig. 7-5, the streaming current  $I_s$  can be determined.

First measurements on Skydrol 500A gave a positive value for  $I_s$  of the order of  $10^{-11}$  amps. Some concern was felt that such small currents may simply be due to extraneous effects and not represent a real streaming current. Figure 7-6 shows the results of an experiment in which small excess pressures were applied to the upper can to increase the flow velocity. From Eq. 7-5 it may be seen that  $I_s$  should be proportional to  $\Delta P$ . The flow velocity should be proportional to  $\Delta P$  so that a graph of  $I_s$  versus flow velocity should be a straight line. A reasonably good straight line fit was obtained in Fig. 7-6, indicating that the measured currents were indeed streaming currents.

When Skydrol 500A is filtered through fuller's earth there is a significant reduction in damage to the valves. Measurements made on such filtered Skydrol showed that the streaming current  $I_s$  was reduced by a factor of more than 100.

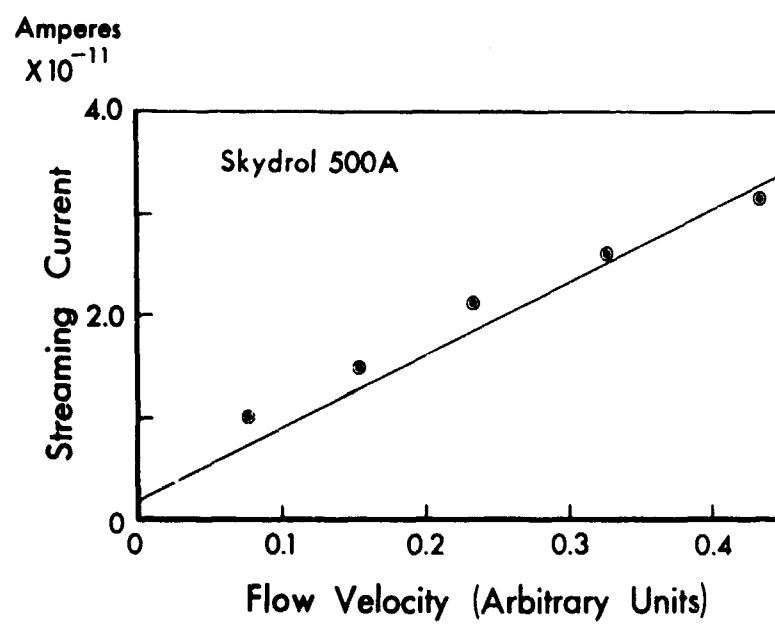


Fig. 7-6. Streaming current versus flow velocity.

Table 7-1 shows the values of  $\epsilon\zeta$  which were determined for various hydraulic fluids. Two examples of Aerosafe 2300\* were measured, both having the same lot number but coming from different containers. It may be noted that a factor of four difference was observed in the  $\zeta$  potential of the two samples, indicating some different history or contamination. Such variations in fluid properties may account for some of the apparent randomness of valve damage in aircraft. (See the conductivity measurements in Sec. 8.1.)

It is known that the addition of water to Skydrol 500A reduces damage to valves so that the effect of the addition of water was of interest. (The effect on conductivity is shown in Fig. 8-1 in the section on conductivity.) The effect on the value of  $\epsilon\zeta$ , as determined from streaming current measurements was not accurately reproducible, but the usual tendency was to approximately double the value of  $\epsilon\zeta$  on the addition of 0.2% water and with additional water no further significant change was observed.

The effect of some additives other than water to Skydrol 500A was also tested. The object of the experiment was to determine the possibility of changing the  $\zeta$  potential by the addition of certain neutral or positively charged surface active species which would displace or counteract the negatively charged surface active species already present in the hydraulic fluid.

---

\* Phosphate ester hydraulic fluid, Stauffer Chemical Company.



Table 7-1  
 Approximate Electrical Parameters  
for Hydraulic Fluids

	<u><math>\epsilon</math></u>	<u><math>\zeta</math></u>	<u><math>\epsilon\zeta</math></u>
Skydrol 500A	8	50mV	400
Skydrol 500A Filtered through fuller's earth	8	<.5mV	<4
Skydrol 500C	8	25mV	200
Aerosafe 2300			
Container (a)	8	25mV	200
Container (b)	8	100mV	800
MIL #5606 B(2)	2	33mV	66
SST Hydraulic Fluid			<u>&lt; 20</u>

The addition of 2 cc of a 25% aqueous solution of tetramethyl ammonium hydroxide to 500 cc of Skydrol 500A changed the sign of the measured streaming current and increased its magnitude by about a factor of ten. This implies a corresponding change in sign and increase in magnitude in the  $\zeta$  potential. The addition of 2 cc of a neutral nonyl phenyl type surface active ingredient to 500 cc of Skydrol 500A reduced the value of the  $\zeta$  potential by approximately a factor of two. These measurements indicate that it is possible to modify the electrokinetic properties of the hydraulic fluids by the use of appropriate additives.

#### 7.2.2 Wall Current Measurements with Phosphate Ester Fluids

Measurements of the wall current were performed with the apparatus shown in Fig. 7-7 rather than with the more complicated geometry of the servo valves. The flow field is similar to that in the valves. The fluid is accelerated in the 90° converging channel formed by the hypodermic tube and the flat plate toward the small orifice flowing from the metal slug was measured as a function of pressure drop across the device. The total wall current can be estimated from the theory by integrating Eq. 7-11 from  $x = \infty$  in to  $x = g$  and multiplying by the tube circumference.

$$I_w = \pi D \int_g^{\infty} J_w dx = \frac{.585 \pi D v c c_o \zeta}{g^2} \left( \frac{Q}{v} \right)^{3/2} \quad 7-12$$

The exact inner limit of the integration depends on a more accurate knowledge of the flow near the gap, but Eq. 7-12 should give at least a good estimate.

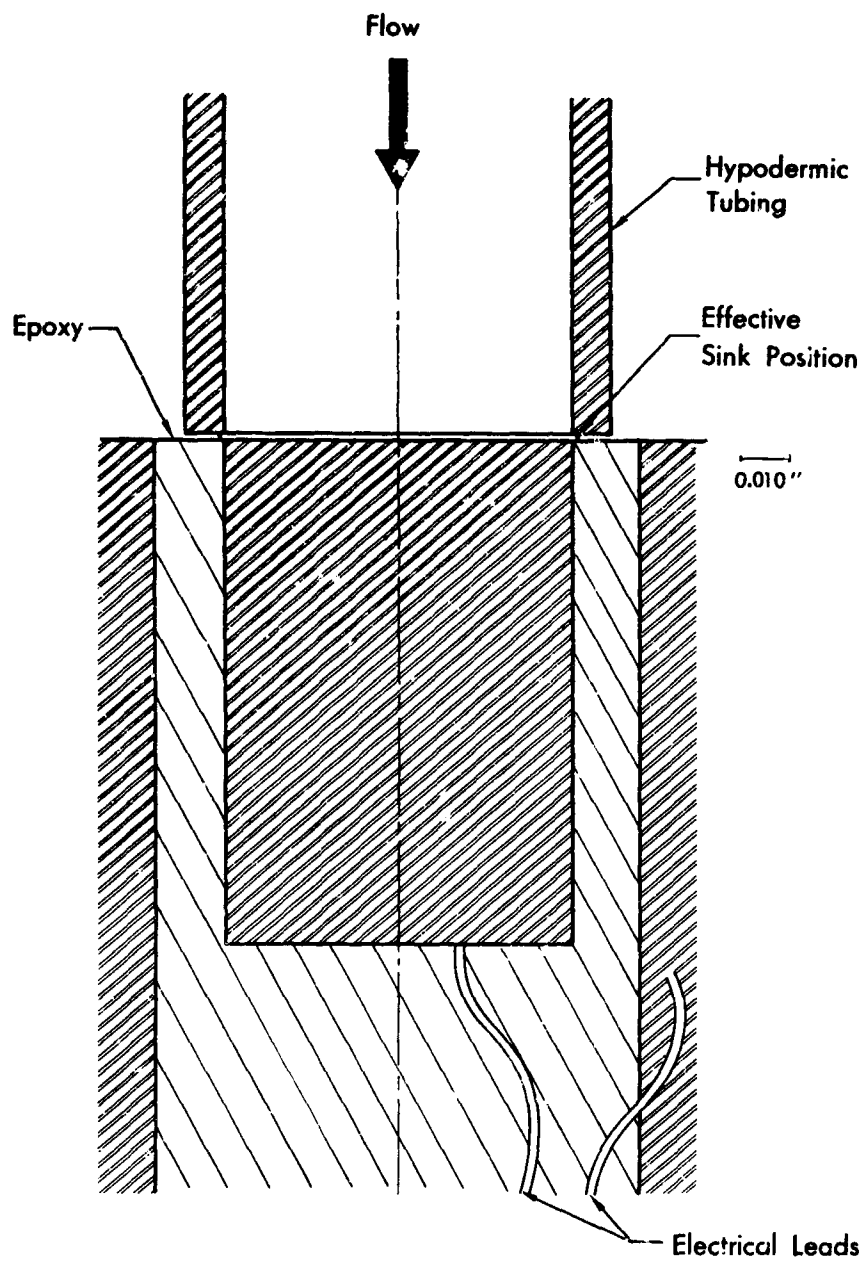


Fig. 7-7. Wall current measurement apparatus.

Equation 7-12 predicts that  $I_w$  should vary as  $Q^{3/2}$ . Since  $Q$  varies as  $\sqrt{\Delta P}$ ,  $I_w$  should vary as  $\Delta P^{3/4}$ . Figure 7-8 is an experimental plot of  $I_w$  versus  $\Delta P$  together with a  $3/4$  power curve fitted to one point. The good agreement between data and theory suggests that the assumption of constant  $\zeta$  potential was correct.

The value of  $I_w$  calculated from Eq. 7-12 is  $.25\mu A$  at a flow of 11 cc/sec. The value of the  $\zeta$  potential of the fluid was measured to be .025 volt with the apparatus described in Sec. 7.2.1. The current measured with the apparatus of Fig. 7-7 was  $2.2\mu A$ . The factor of nine difference can probably be attributed to improper choice of the lower limit for the integration. A sink located  $1/3$  g rather than g beyond the edge of the metal slug would bring the calculated current up to the measured value.

During the current measurements the fluid flow rate and current were observed to decrease with time after first starting the flow. The flow reduction was due to formation of a whitish film in the neighborhood of the orifice. After several minutes of flow the current and flow would reach a steady level. The measurements reported above were performed at that steady level. Further discussion of the film is given in Secs. 9, 11.3 and 14.6.

### 7.2.3 Wall Current Measurements with Other Fluids

Table 7-2 allows a comparison between phosphate ester fluids and other hydraulic fluids. No film formation was observed in these other fluids. The first point of interest is that the wall currents are less for the SST fluid and MIL-H-5606. Yet, the wall current does not vary

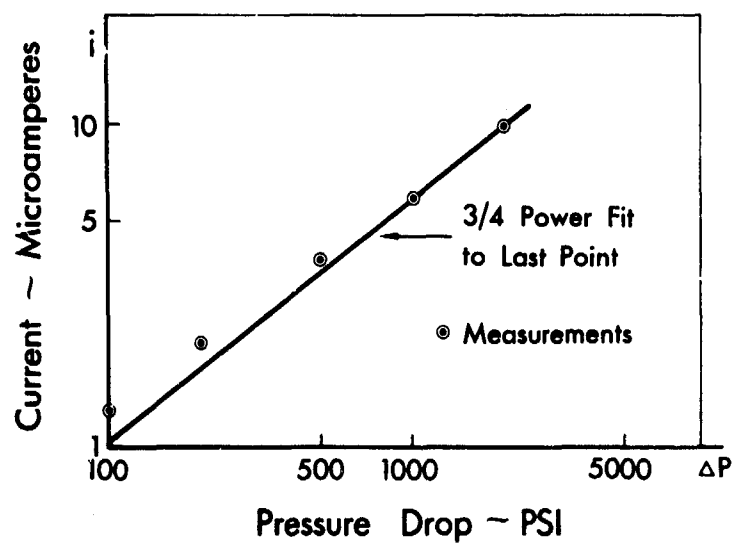


Fig. 7-8. Relation between current and pressure drop.

Table 7-2

Comparison of Three Fluids

<u>Type of Fluid</u>	<u>Electrical Conductivity</u>	<u><math>\epsilon\zeta</math></u>	<u><math>I_w</math> at 2000 psi</u>
Phosphate Ester	$10^{-7}$ mho/cm	400 mV	1.0 $\mu$ A
SST (Humble WSX- 7597)	$10^{-11}$	less than 20 mV	.002 $\mu$ A
MIL-H-5606	less than $10^{-13}$ mho/cm	66 mV	less than .001 $\mu$ A

linearly with  $\epsilon\zeta$  as predicted by Eq. 7-12. The reason is that Eq. 7-12 is based on the assumption that the electrical double layer is thin compared to both the hydrodynamic boundary layer thickness and the length scale of variations along the wall. Neither of these conditions is met by fluids of extremely low conductivity and the resulting error is in a direction that causes Eq. 7-12 to predict a higher than observed wall current. Further discussion of the effect of conductivity is in Sec. 14.2.

### 7.3 Conclusions

1. Well established principles of hydrodynamic and electrokinetic theory can be combined to quantitatively explain the current flows observed in phosphate ester fluids.
2. The  $\zeta$  potential of the electrical double layer in the phosphate ester fluids seems to be roughly independent of the fluid flow rate.
3. Additives can be used to change the  $\zeta$  potential of phosphate ester fluids.
4. A more detailed argument is required to quantitatively explain current flows in fluids of much lower or higher conductivity.
5. A more detailed hydrodynamic argument is required to predict current density in the neighborhood of the orifice and to avoid *ad hoc* assumptions as to the effective sink position.



## 8.0 CONDUCTIVITY OF FLUIDS

Because fluid conductivity plays a role in the streaming and wall current mechanism, measurements of conductivity were made and the effects of several additives and temperature were determined. An analysis of the data was made in an effort to determine the nature of the conducting species in phosphate ester fluids.

### 8.1 Experiments

The A.C. conductivity of several hydraulic fluids was measured in a glass conductivity cell with platinized platinum electrodes. Frequencies from  $10^3$  to  $10^5$  Hertz were used. In addition, some relative values were obtained from the D.C. conductances of different fluids in the electrochemical cells described in Sec. 9.0.

The conductivity of Skydrol 500A which was used in many of the experiments described in this report was approximately  $10^{-7} \text{ohm}^{-1} \text{cm}^{-1}$ . Relative conductivities of various hydraulic fluids are presented in Table 8-1. The as-received phosphate ester fluids had conductivities of the same order of magnitude while the MIL #5605 B(2), a hydrocarbon fluid, had a conductivity at least six orders of magnitude smaller. Hydraulic fluid under evaluation for the SST had a conductivity about four orders of magnitude less than that of Skydrol. Filtration of Skydrol 500A through fuller's earth, an adsorbing clay material, decreased the conductivity by about an order of magnitude indicating significant removal of the conducting species.\* The conductivity of Aerosafe 2300 fluid from

---

\* Based on data obtained from the Commercial Airplane Division.

Table 8-1

Relative Conductivity of Hydraulic Fluids

	<u>Relative Conductivity</u>	<u>Method</u>
Skydrol 500A	1.4	A.C.
Skydrol 500A Filtered through fuller's earth	$\sim 0.1$	A.C.
Skydrol 500C	$\sim 0.5$	A.C.
Aerosafe 2300		
Container (a)	0.7	A.C.
Container (b)	2.8	A.C.
MIL # 5606 B(2)	$<10^{-6}$	A.C.
Purified tributyl phosphate	$\sim 0.5$	D.C.
SST Fluid	$\sim 10^{-4}$	A.C.

two different 5-gallon cans from the same lot differed by a factor of four indicating some different history, or contamination (see also Table 7-1). The conductivity of distillation-purified tributyl phosphate, a typical phosphate ester, was about one-half that of the formulated fluids. This suggests that the phosphate ester contributes a significant portion of the conductivity to the formulated fluids.

The effect of some additives on conductivity is indicated in Figs. 8-1 and 8-2, in which conductivity relative to the value with no additive is plotted versus the molar concentrations of the additive. Addition of 1.1 mole/liter of water (2%) nearly triples the conductivity of Skydrol 500A according to the A.C. conductivity measurement. The somewhat smaller increase observed in the D.C. measurement may be in part due to films formed on the electrodes (Sec. 9.1). Aerosafe 2300 and Aerosafe basestock appeared to have a smaller increase in conductivity with water addition than Skydrol 500A. (Basestock is a mixture of phosphate esters without other additives.) Hydroquinone increases conductivity of Skydrol 500A on a molar basis more than water. It is seen in Fig. 8-2 that pyridine and nitromethane in small amounts decrease conductivity, although pyridine increased conductivity at higher concentrations.

Addition of 2 cc of a 25% aqueous solution of tetramethyl ammonium hydroxide per liter of Skydrol 500A in the streaming current measurements increased the conductivity by about a factor of 10. Addition of this solution to the fluid in the high-pressure flow experiments resulted in formation of a precipitate which clogged the filter. The initial decrease in conductivity with added pyridine and nitromethane may be due to

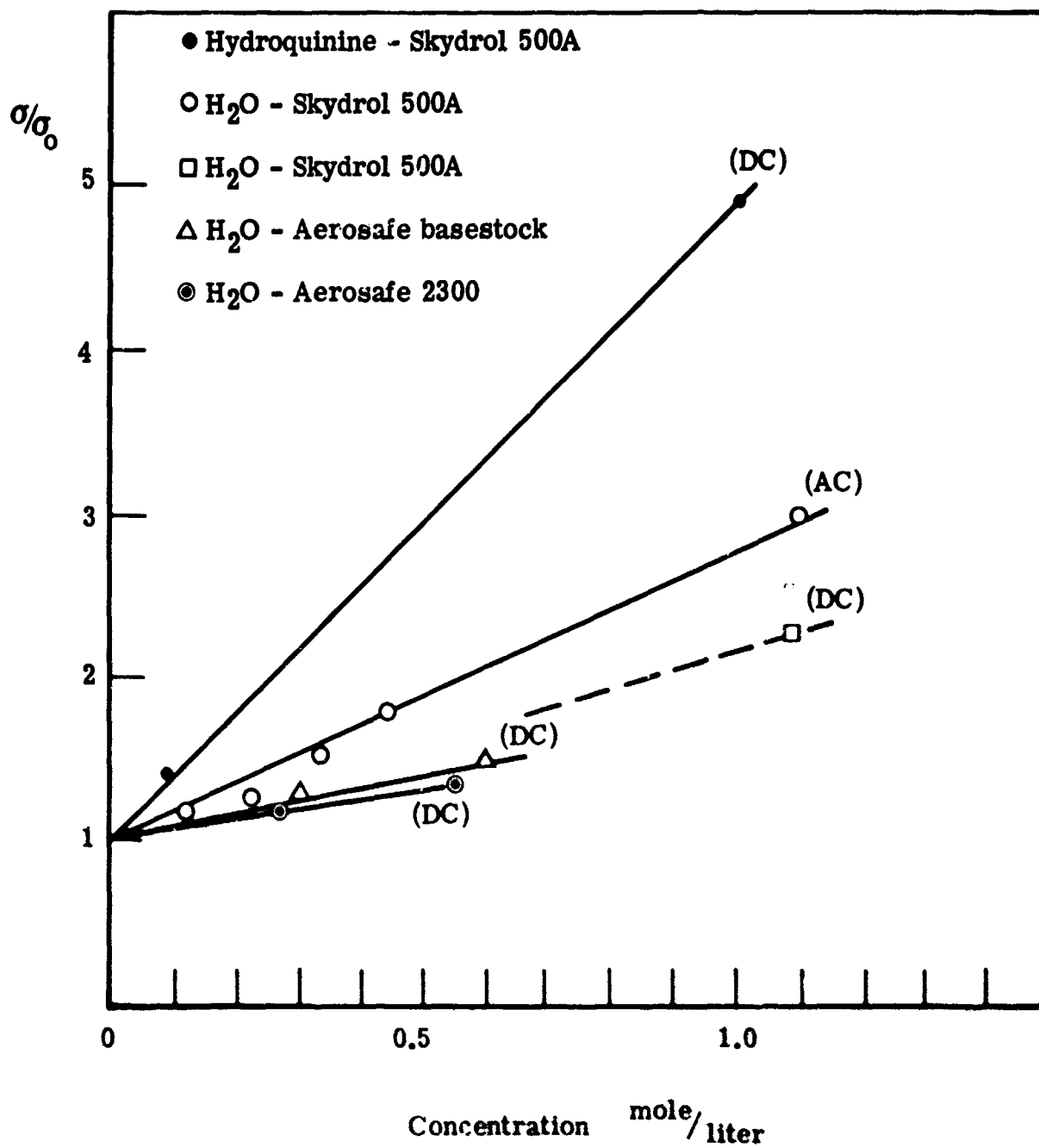


Fig. 8-1. Effect of added water and hydroquinone on the conductivity of fluids.

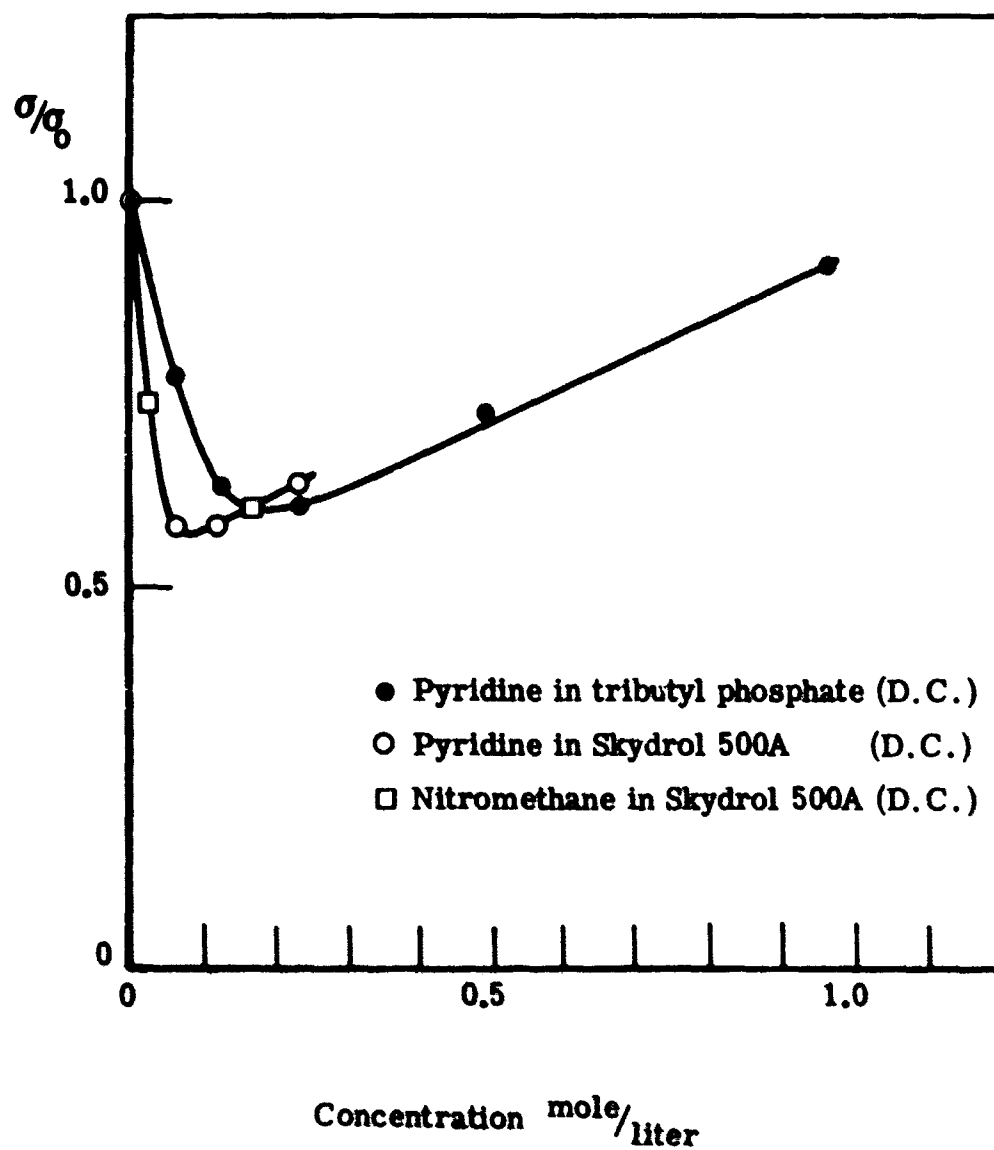


Fig. 8-2. Effect of pyridine and nitromethane on fluid conductivity.

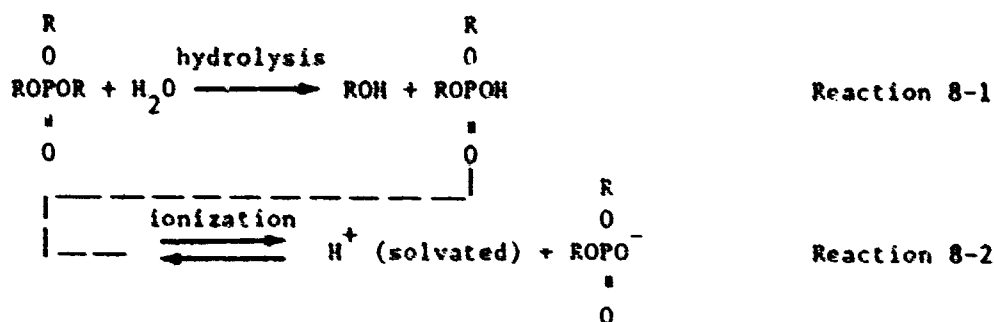
formation of a complex with the conducting species analogous to formation of a precipitate with tetramethyl ammonium hydroxide.

Conductivity increases with temperature as shown in Fig. 8-3. The basestock, the formulated fluid and the fluids with 1% added water have a similar relationship of relative conductivity to temperature. During the period at 130°C the wet formulated fluid showed a 30% decrease in conductivity, probably due to removal of the added water by vaporization. Bubbles were observed in this fluid at a temperature above 100°C during heating and fumes were observed. The basestock had a 20% increase in conductivity when held at 150°C and this relative increase persisted down to room temperature on cooling. Hydrolysis of the phosphate ester at the high temperature is suspected as the cause of this increased conductivity.

## 8.2 Theory

The conducting species are either ions produced from an impurity or additive, or ions produced from the phosphate esters. Distillation-purified tributyl phosphate had a conductivity of the same order of magnitude as the formulated fluids suggesting the latter possibility. An analysis of the conductivity will be made on this basis, although it is recognized that other impurity conducting species are possible.

The hydrolysis and ionization may be represented as follows:



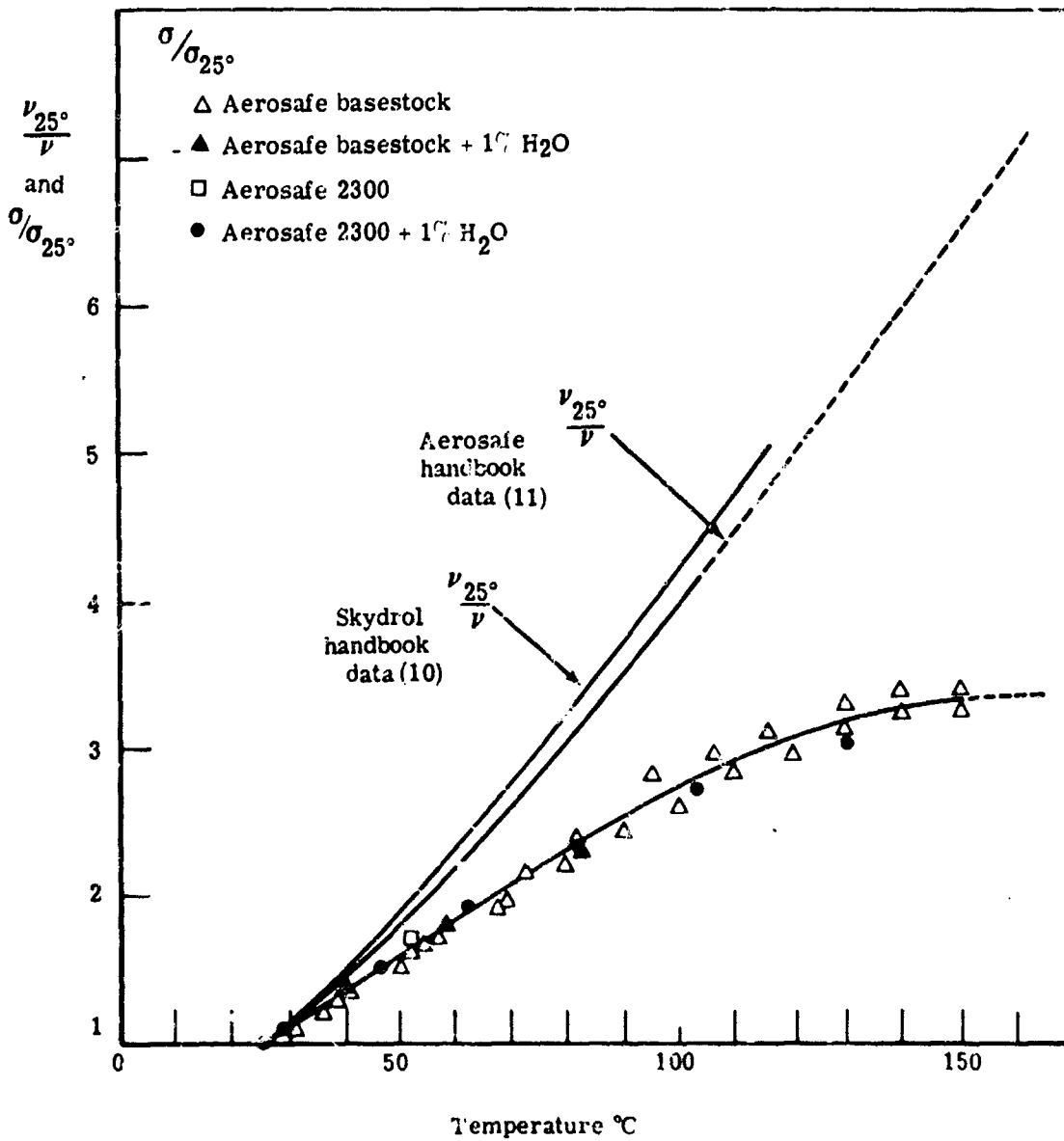


Fig. 8-3. Effect of temperature on relative conductivity of fluids as compared to relative viscosity.

It is not known whether the hydrolysis reaction is rate determined or is at equilibrium but the ionization of the phosphate acid is assumed to be at equilibrium.

Conductivity can be related to concentration by

$$\sigma = \frac{F^2}{RT} \sum z_i^2 D_i C_i \quad 8-1$$

using the Nernst-Einstein approximation for mobility [9]. The solvated hydrogen ion and the acid anion are assumed to have the same structure and molecular weight giving the same diffusivity for each. For this condition,

$$\sigma \approx 2 \frac{F^2}{RT} DC \quad 8-2$$

where C is the concentration of the ionized acid. For a conductivity of  $10^{-7} \text{ ohm}^{-1} \text{ cm}^{-1}$  and a diffusivity of  $10^{-6} \text{ cm}^2/\text{sec}$  at  $25^\circ\text{C}$  (see Appendix 14.3), the concentration of ionized acid is  $\sim 10^{-8} \text{ mole/cm}^3$  by Eq. 8-2.

The degree of ionization of any solute in a low-dielectric-constant fluid like a phosphate ester would be expected to be very small. Dissociation constants can be roughly estimated from the Bjerrum equation [12]:\*

$$K_i = \frac{4\pi N a^3}{3} \exp \left[ - \frac{z_1 z_2 e^2}{4\pi \epsilon \epsilon_0 k T a} \right] \quad 8-3$$

---

\* The  $4\pi$  factor has been included in the exponential term to convert the units of Ref. 12 to the rationalized MKS units used in this report.



The value of the effective radius of the ions,  $a$ , is assumed to be

$$a = \left( \frac{3M}{4\pi\rho_d N} \right)^{1/3} \quad . \quad 8-4$$

For a small degree of dissociation,

$$K_i \approx \left( \frac{C^2}{C_A} \right) \quad . \quad 8-5$$

If it is assumed, for example, that the hydrolysis reaction 8-1 is also at equilibrium

$$K_h \approx \frac{C_A^2}{C_P C_H} \quad . \quad 8-6$$

Eliminating  $C_A$  from Eqs. 8-4 and 8-5 gives

$$C = K_i^{1/2} (K_h C_P C_H)^{1/4} \quad . \quad 8-7$$

Putting Eqs. 8-3 and 8-7 in 8-2 gives for a uni-univalent electrolyte

$$\sigma = 2 \frac{F^2}{RT} D (K_h C_P C_H)^{1/4} \left( \frac{\rho_d}{M} \right)^{1/2} \exp \left[ - \frac{e^2}{8\pi\epsilon\epsilon_0 kTa} \right] \quad . \quad 8-8$$

If the hydrolysis is not at equilibrium (i.e. rate determined)

$$\sigma = 2 \frac{F^2}{RT} D \left( \frac{C_A \rho_d}{M} \right)^{1/2} \exp \left[ - \frac{e^2}{8\pi\epsilon\epsilon_0 kTa} \right] \quad . \quad 8-9$$

For this model, concentrations of the important species and the equilibrium constants can be calculated with Eqs. 8-2 through 8-9. Assuming that R is a butyl group in reaction 8-1 gives a molecular weight for the acid of 210, and a dielectric constant of 8 for the fluid gives  $K_i \approx 5 \times 10^{-10} \text{ mole/cm}^3$  from Eq. 8-3. For a concentration of conducting species of  $\sim 10^{-8} \text{ mole/cm}^3$  the concentration of acid is therefore

$\sim 2 \times 10^{-7}$  mole/cm<sup>3</sup>.<sup>\*</sup> A phosphate ester molecular weight of 266 and a density of one gives a concentration of phosphate ester of  $\sim 4 \times 10^{-3}$  mole/cm<sup>3</sup>. A water content of 0.2% gives for its concentration  $\sim 10^{-4}$  mole/cm<sup>3</sup>. From these numbers Eq. 8-6 gives a hydrolysis equilibrium constant of  $\sim 10^{-7}$  (dimensionless). These numbers appear to form a consistent set, i.e., they have the correct ranking of magnitudes of concentrations.

It can be seen that addition of water has two principal effects in Eq. 8-8. It increases the  $C_H$  term and increases the dielectric constant. Addition of 2% water to a fluid with an initial 0.1% water would increase the conductivity by about a factor of two by the  $C_H$  term. Using a simple additive law for the effect of added water on the dielectric constant gives for 2% water a dielectric constant of  $0.02(79-8) + 8 = 9.4$ . (The additive law appears to be approximately correct based on measurements with Skydrol.) This value gives a factor of three from the exponential term in Eq. 8-8, or a total correction factor about six. The experimental data in Fig. 8-1 show a factor of 2 to 3.

Increased ionization of a solute at constant concentration would be affected only by the dielectric constant in Eq. 8-9. The rate-determined-hydrolysis or the ionized-impurity model would therefore appear to fit the experimental data better than the equilibrium-hydrolysis model, although the accuracy of the data or models may not be sufficient for a

---

\* A typical acid number of 0.03 mg KOH/gm for new fluid corresponds to an acid concentration of  $\sim 5 \times 10^{-7}$  mole/cm<sup>3</sup> which gives an order of magnitude check on the validity of these numbers.

definitive test. The smaller increase in conductivity with added water for Aerosafe fluid as compared to Skydrol is consistent with the known lower molecular weight for the Aerosafe basestock.

Temperature has two principal effects on conductivity in Eqs. 8-8 and 8-9, through the diffusivity and through the dielectric constant. (The effect on  $K_h$  and  $\rho_d$  which have fractional exponents will be neglected.) As indicated in Appendix 14.3, diffusivity varies as absolute temperature over viscosity. This temperature term cancels out the term in the denominator of the  $F^2/RT$  so conductivity should vary as the reciprocal of viscosity. It is seen in Fig. 8-3 that the values of  $\nu_{25^\circ}/\nu$  from handbook data for Skydrol and Aerosafe increase more with temperature than the relative conductivities. It is suspected that this is due to the decrease in the dielectric constant with temperature, which has the relation [13]

$$\epsilon = \epsilon^0 \exp(-LT) \quad . \quad 8-10$$

The value of  $L$  calculated from variation of  $\epsilon$  with temperature shown on the data sheets for Skydrol [10] and Aerosafe [11] is such that the exponential term in Eq. 8-8 could account for the difference between the experimental data and  $\nu_{25^\circ}/\nu$  in Fig. 8-3. The ratio of experimentally determined relative conductivity to handbook relative viscosity is compared to the theoretical correction factor for change of dielectric constant with temperature in Fig. 8-4. The ionizable impurity and the rate controlled hydrolysis models would be affected by temperature in the same way. It is not known how the equilibrium constant for hydrolysis would vary with temperature and affect the equilibrium-controlled hydrolysis model.

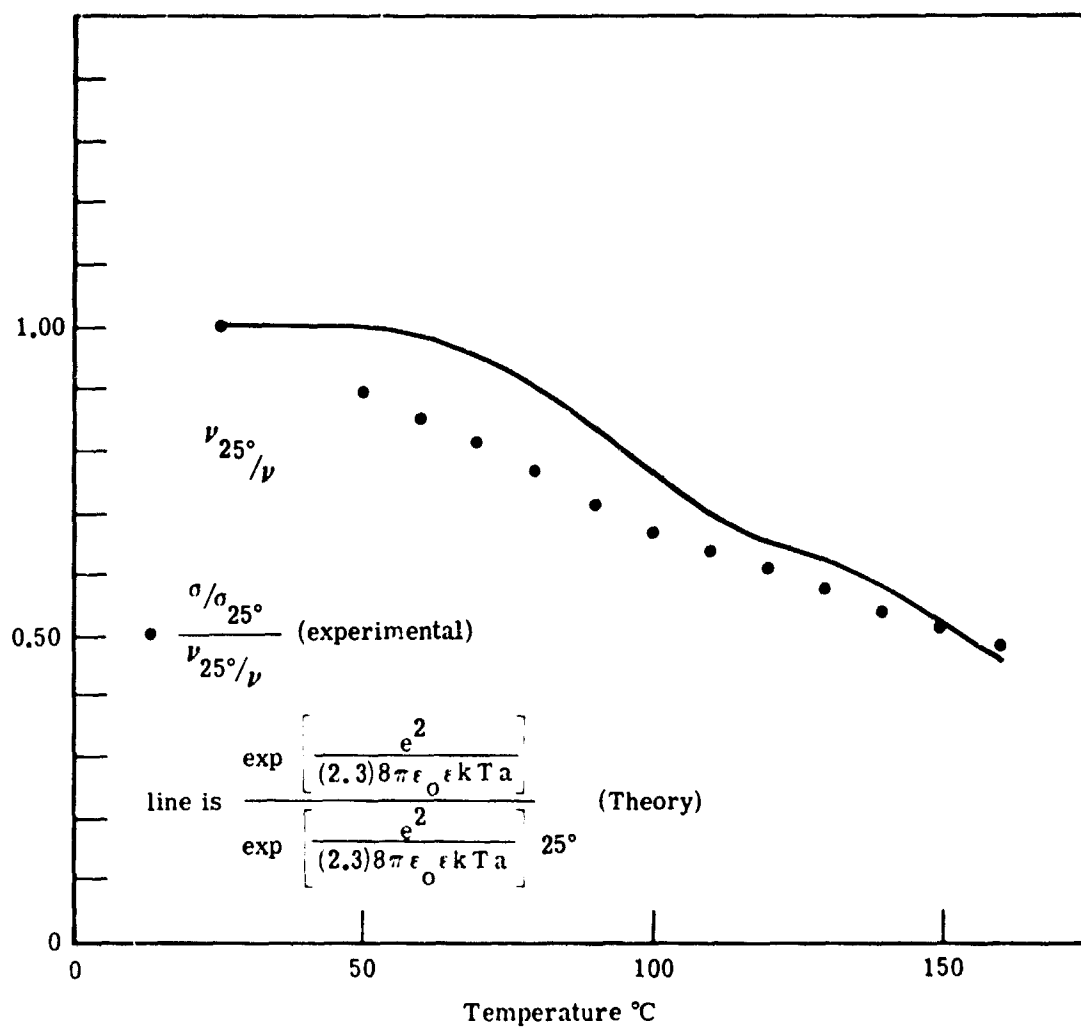


Fig. 8-4. Comparison of theoretical and experimental deviation of relative conductivity from purely viscous effects.

The increased conductivity caused by addition of hydroquinone also appears to be consistent as to order of magnitude with Eqs. 8-2 through 8-5. The calculated ionization constant is  $2.2 \times 10^{-11}$  mole/cm<sup>3</sup> which for a concentration of  $10^{-3}$  mole/cm<sup>3</sup> (1 mole/liter) gives a concentration of dissociated species of  $1.5 \times 10^{-7}$  mole/cm<sup>3</sup> assuming one OH group ionized per molecule. The calculated conductivity, assuming the same diffusivity as for hydrolyzed phosphate ester, is therefore  $1.1 \times 10^{-6}$  ohm<sup>-1</sup>cm<sup>-1</sup> as compared to an increment of  $\sim 0.4 \times 10^{-6}$  ohm<sup>-1</sup>cm<sup>-1</sup> in Fig. 8-1. The important point from the hydroquinone experiment is that a relatively large amount of solute (impurity) is required in order to obtain a conductivity equal to that of the fluid.

The conductivity increase obtained with the tetramethyl ammonium hydroxide addition was larger than calculated. The calculated value from a calculated ionization constant of  $1.4 \times 10^{-11}$  mole/cm<sup>3</sup> was  $6.5 \times 10^{-8}$  ohm<sup>-1</sup>cm<sup>-1</sup> as compared to a measured value of about  $1 \times 10^{-6}$ . Several possible explanations exist: the diffusivity of hydroxyl ion is greater than the assumed  $10^{-6}$ , the dielectric constant of the fluid increases with addition of the polar amine hydroxide, and the formation of a precipitate with the amine may drive the dissociation further, giving a higher concentration of more conductive hydroxyl ions. Table 8-2 gives a summary of calculated and observed conductivities.

The identity of the conducting species has not yet been determined but the preponderance of evidence appears to be in favor of the acid produced by hydrolysis of the phosphate esters as indicated in Table 8-3. A low conductivity persisting for some time after filtration through

Table 8-2  
Comparison of Concentration of Conducting  
Species and Conductivities

<u>Solute</u>	<u>M</u> <u>gm/mole</u>	<u>C<sub>A</sub></u> <u>mole/cm<sup>3</sup></u>	<u>K<sub>i</sub></u> <u>mole/cm<sup>3</sup></u>	<u>C</u> <u>mole/cm<sup>3</sup></u>	<u>σ<sub>calc</sub></u> <u>ohm<sup>-1</sup>cm<sup>-1</sup></u>	<u>σ<sub>meas</sub></u> <u>ohm<sup>-1</sup>cm<sup>-1</sup></u>
Assumed Phosphate Ester Acid	210	$2 \times 10^{-7}$	$5 \times 10^{-10}$	$10^{-8}$	-	$1 \times 10^{-7}$
Hydroquinone	110	$10^{-3}$	$2.2 \times 10^{-11}$	$1.5 \times 10^{-4}$	$1.1 \times 10^{-6}$	$0.4 \times 10^{-6}$
Tetramethyl Ammonium Hydroxide	99	$5 \times 10^{-6}$	$1.4 \times 10^{-11}$	$8 \times 10^{-9}$	$6 \times 10^{-8}$	$1 \times 10^{-6}$

Table 8-3

Consistency of Behavior of Proposed Conducting  
Species in Fluid with Various Treatments of Fluid

Treatment	Impurity Ions	Conducting Species	
		Acid from Hydrolysis of Phosphate Ester	
		Rapid Equilibrium	Slow Equilibrium
Fuller's earth filtration	Yes	No	Yes
Water addition	Yes	No, but not definitive	Yes
Increase temperature	Yes	No, but not definitive	Yes
Purify basestock by distillation	No	Yes	Yes
Hydroquinone addition as compared to fluid additives	No	Yes	Yes

fuller's earth suggests that the rate of hydrolysis is rather slow at room temperature.\*

The effects of various anion-cation combinations added to phosphate ester fluids are summarized in Table 8-4. It would appear at this time that the only suitable additives to increase conductivity are those containing high molecular weight organic anions. It would be desirable that they have low surface activity in order to not increase the  $\zeta$  potential and streaming current. A correlary to this is that the streaming current in phosphate ester fluids may very likely be caused by the acid anion produced by hydrolysis. The phosphate anion is correspondingly one of the more strongly adsorbing anions in aqueous systems.

### 8.3 Conclusions

1. There is a very low degree of ionization of solutes in phosphate ester fluids, consistent with the low dielectric constant.
2. Conductivity of phosphate ester fluids appears to be largely due to the presence of acid formed by hydrolysis.
3. Removal of the acid would not be likely to produce a permanent decrease in conductivity because of continued slow hydrolysis.
4. The most likely candidates for increasing conductivity are acids or salts with high molecular weight organic anions.

---

\* This is consistent with vendor data for change of acid number with time at elevated temperatures.



Table 8-4

## Effects of Various Anion-Cation

Combinations Added to Phosphate Ester Fluid

Anion	Cation	Effect
Inorganic	Inorganic	Not appreciably soluble or dissociated.
$\text{OH}^-$	Amine	Get precipitate with fluid.
Organic	$\text{H}^+$	Slight dissociation. Need high molecular weight anion for conductivity.
Organic	e.g., $\text{Na}^+$	Not tested. Would need high molecular weight anion for conductivity.

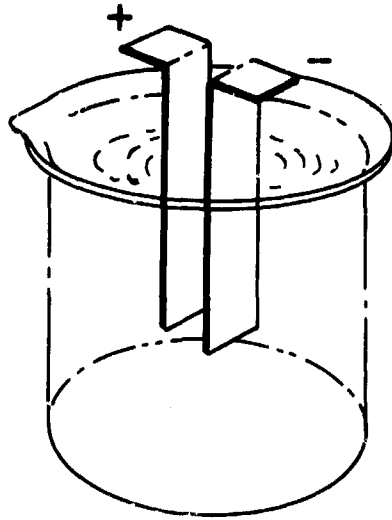
## 9.0 ELECTROCHEMISTRY IN PHOSPHATE ESTER FLUIDS

Experiments were conducted to determine if corrosion of iron surfaces in phosphate ester fluids could be produced by purely electrochemical means in the absence of high velocity flow. The first experiments with parallel-electrode cells did not produce significant corrosion but yielded supplementary information useful in understanding electrochemistry in phosphate-ester fluids. After it was realized that higher current densities than were obtainable with the parallel electrode cells would be required to obtain pitting corrosion, experiments were conducted with a needle-to-plane electrode cell. Some approximate electrode polarization data were also obtained with the needle-to-plane cell.

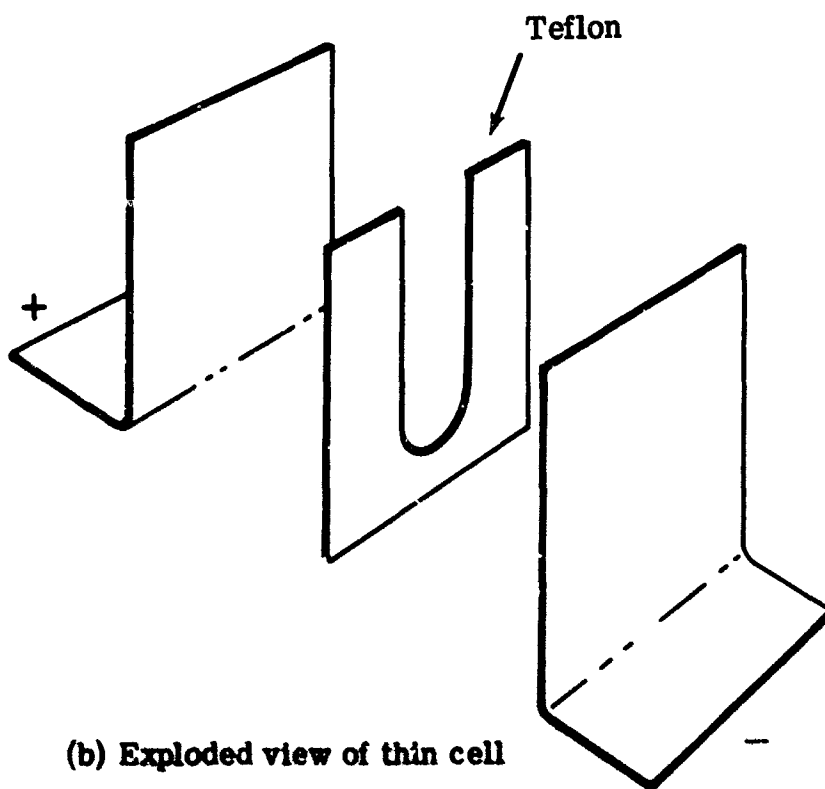
### 9.1 Parallel-Electrode Cell Experiments

The parallel-plate electrode cells are illustrated in Figs. 9-1 and 9-2. The cells of Fig. 9-1 were 100-ml and one-liter beakers with pairs of parallel iron sheet electrodes. The cells of Fig. 9-1b were made by clamping a 0.010 inch thick Teflon sheet, with a cut-out area for electrolyte, between two iron sheet electrodes. These cells with the smaller interelectrode spacing permitted obtaining a higher current density than was attainable for the beaker cells with the 500 volt power supply used. The rotating disk electrode shown in fig. 9-2 had an iron slug pressed into a Teflon fitting attached to a rotating shaft with slip rings.

Conditions and calculated quantities from the results of the parallel electrode cell experiments are given in Table 9-1. It may be noted that the calculated electrolyte conductivity corresponds to the



(a) Beaker cell with iron sheet electrodes



(b) Exploded view of thin cell

Fig. 9-1. Parallel plate cells.

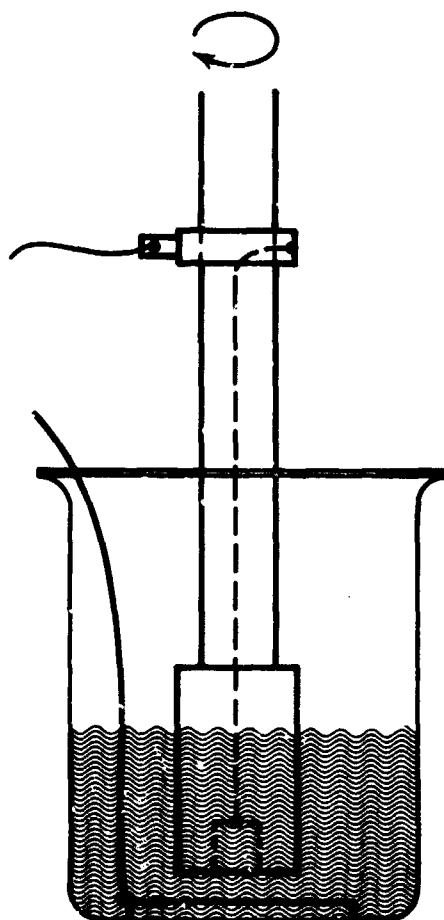


Fig. 9-2. Rotating disk electrode cell.

Table 9-1  
Conditions and Results for Electrolysis Experiments

Experiment No. Cell	with Parallel Electrode Cells					
	1 Thin Cell	2 100 ml Beaker	3 100 ml Beaker	4 1000 ml Beaker	5 1000 ml Beaker	6 Rotating Disk Cell
Potential applied, $\phi$ (volts)	100	500	500	500	500	500
Electrode area, A (cm <sup>2</sup> )	0.7	~1.7	~1.7	24	24	0.283
Interelectrode spacing, d (cm)	0.025	~1	~1	0.4	0.3	0.47
Initial current, $I_1$ (amps)	$300 \times 10^{-6}$	$110 \times 10^{-6}$	$90 \times 10^{-6}$	$2200 \times 10^{-6}$	$2050 \times 10^{-6}$	$33 \times 10^{-6}$
Volume of electrolyte, V (cm <sup>3</sup> )	$2.0 \times 10^{-2}$	70	70	950	850	~50
Duration of electrolysis, $\Delta t$ (sec)	200	$15 \times 3600$	$(65 \times 3600)$	$(270 \times 3600)$	$313 \times 3600$	$(5 \times 3600)$
Total charge per unit volume $\frac{I_1 \Delta t}{V}$ ( $\frac{\text{Coul}}{\text{cm}^3}$ )	3.0	0.08	0.3	2.3	2.7	-
Current density (amp/cm <sup>2</sup> ) $i = I_1/A$	$4 \times 10^{-4}$	$6 \times 10^{-5}$	$5 \times 10^{-5}$	$9 \times 10^{-5}$	$8.5 \times 10^{-5}$	$7 \times 10^{-5}$
Field, $F = \phi/d$ (volt/cm)	4000	500	500	1200	1700	1100
Approximate electrolyte conductivity, $\sigma = 1/F$ (ohm <sup>-1</sup> cm <sup>-1</sup> )	$1 \times 10^{-7}$	$1.2 \times 10^{-7}$	$1 \times 10^{-7}$	$0.8 \times 10^{-7}$	$0.5 \times 10^{-7}$	$0.6 \times 10^{-7}$

measured value with A.C. (Sec. 8-1). The calculation was only accurate to order of magnitude because the current distribution was not perfectly uniform at the electrodes.

The initial current was linearly related to potential as shown in Fig. 9-3 for the 100-ml beaker cell for large applied potentials. The slope of the curve was consistent with an electrolyte conductivity of  $10^{-7} \text{ohm}^{-1} \text{cm}^{-1}$  indicating that current was limited by electrolyte IR drop. After passing current for a period of time the initial open-circuit potential of the cell was 1 to 3 volts indicating that some electrochemically active materials had been deposited on the electrodes. The rotating-disk-electrode experiment at 500 volts applied to the cell produced essentially no change in current when still or at 1000 RPM, consistent with IR-drop control. A white electrodeposited film which formed was thicker at the rim of the iron disk as expected for a primary current density controlled by IR drop.

In all of the parallel-electrode electrolysis experiments the current decreased with time as shown in Fig. 9-4, where the current, scaled with the initial value, is plotted against charge per unit volume at the initial current,  $I_{1T}/V$ . The choice of charge per unit volume rather than per unit area as the abscissa was purely arbitrary in order to fit all of the curves on the same plot. The decrease in current in the one liter cell experiment appeared to be related to the formation of electrode films as indicated in Fig. 9-5. Scraping the films from the electrodes restored approximately the original current-potential relationship.

The amount of charge passed per unit volume is three orders of magnitude larger than the calculated concentration of charge carriers in

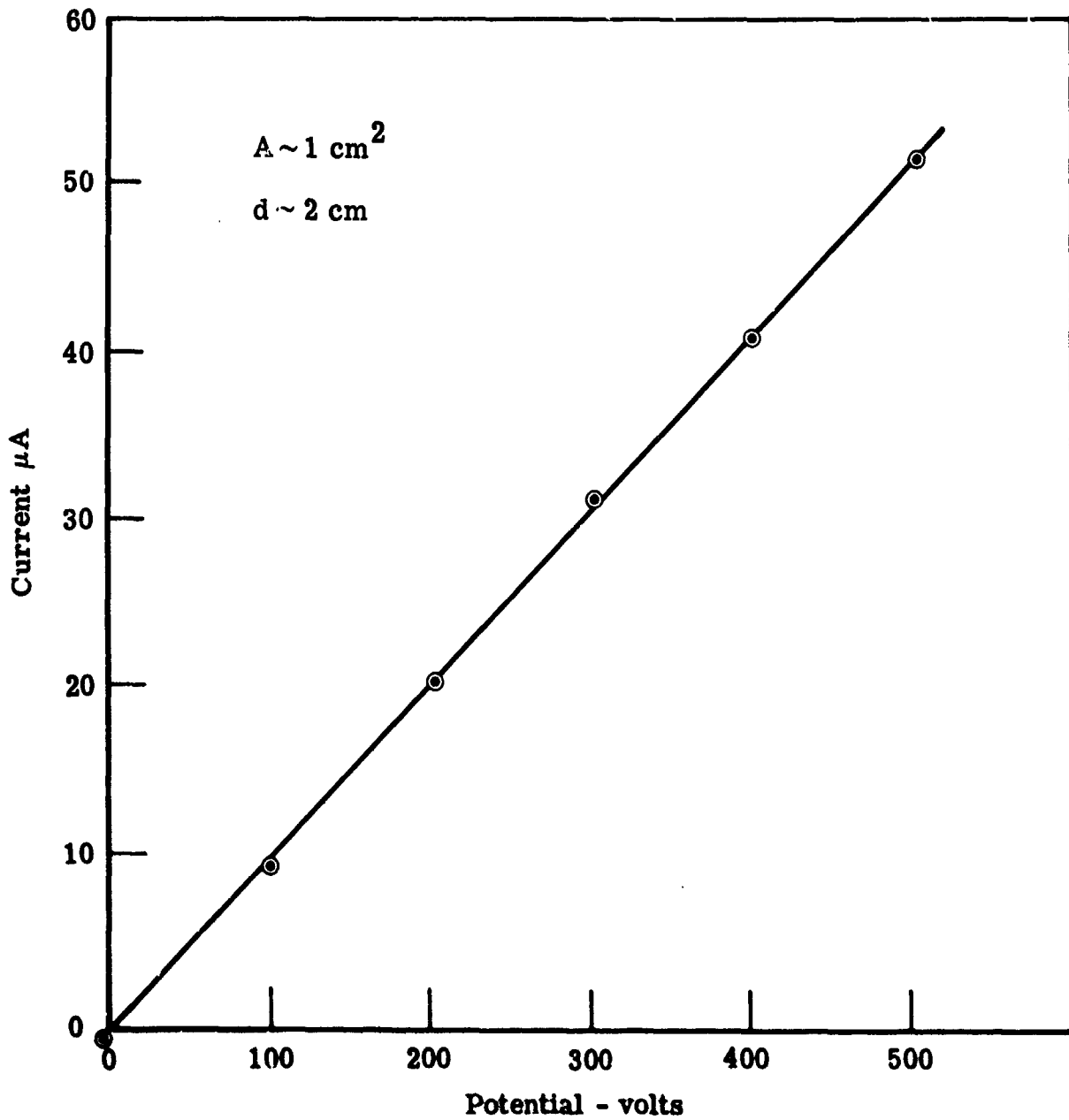


Fig. 9-3. Initial current-potential curve. (Experiment No. 2, Table 9-1)

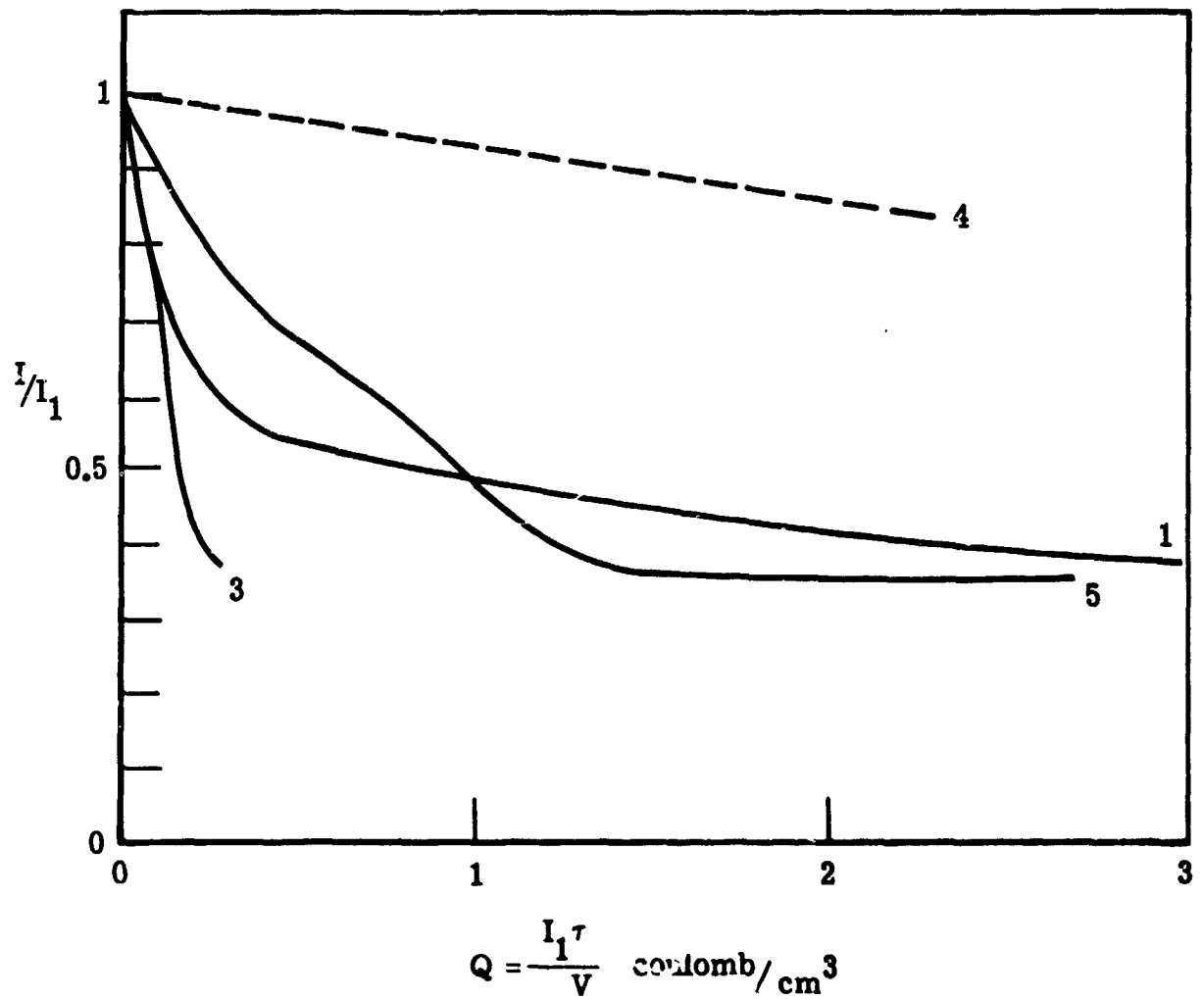


Fig. 9-5. Current-potential curves before and after electrolysis.  
(Experiment No. 5, Table 9-1.)



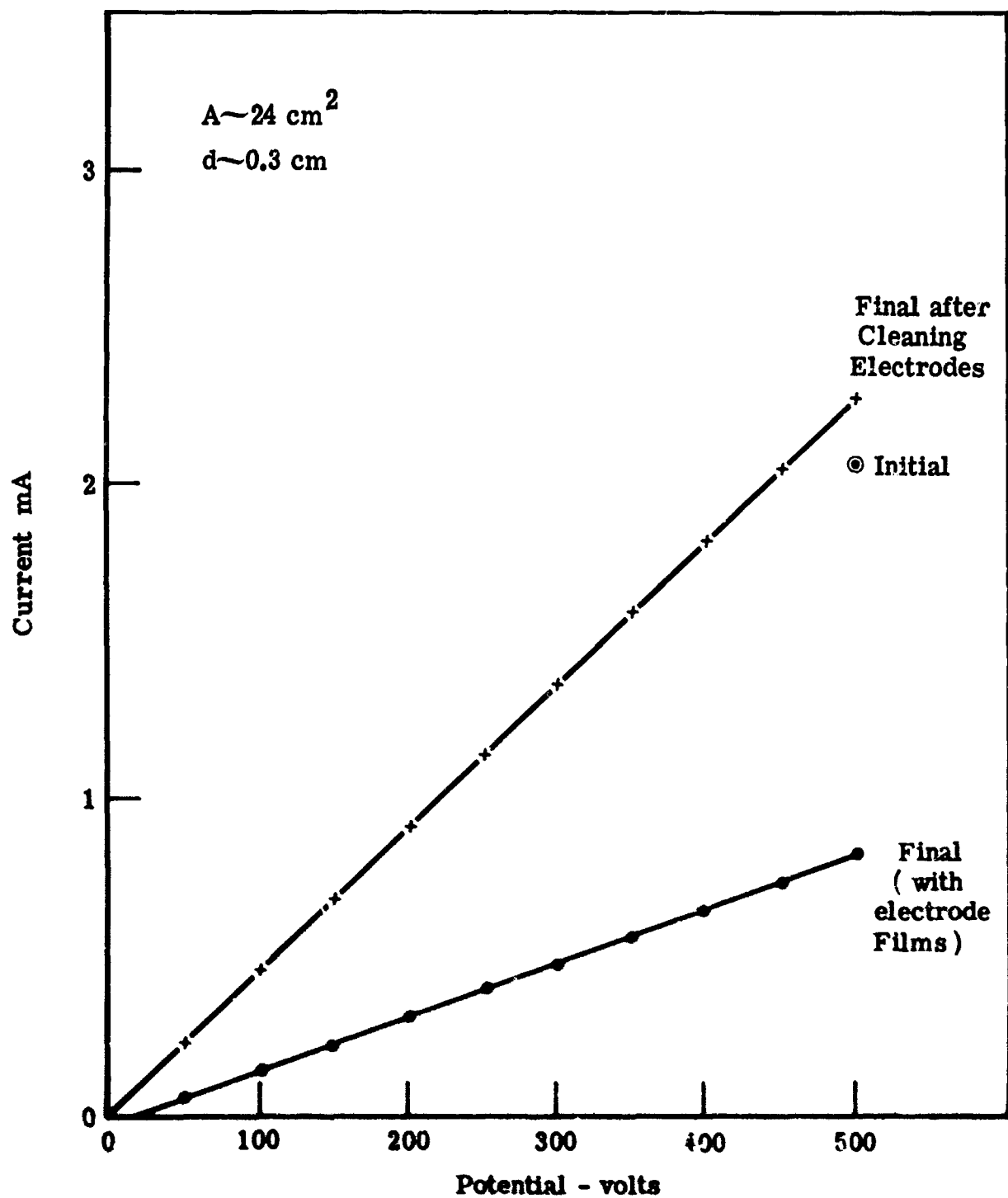


Fig. 9-4. Decay of current with total charge passed. (Number on curve indicates experiment number in Table 9-1.)

solution based on the conductivity (see Sec. 8.2). The conducting species are therefore either not consumed in the anodic or cathodic reactions or they are generated in the cell as fast as they are removed.

Changes in fluid properties as a result of the electrolysis in experiment No. 5, Table 9-1 are given in Table 9-2. The streaming current measured in the Klinkenberg apparatus decreased, indicating that a fraction of the surface-active anions had been removed. The relative conductivity increased indicating a small increase in the concentration or mobility of conducting species. The increase in conductance from Table 9-2 is 24% compared to 11% indicated in Fig. 9-5 which is within experimental error, as the electrodes were not scraped perfectly clean.

Analyses of the anode and cathode films from experiment No. 5, Table 9-1, are given in Table 9-3. The films were washed with acetone *in situ* and then scraped off the electrodes. The anode film cracked (like mud on a dry lake bed) after washing and was easily removed with a Teflon scraper. The total weight of anode material collected was 0.135 gram, which was estimated to account for about 90% of the anode film. It was a light tan color. The amount of cathode film was only about 1 to 10% by volume of the anode film and was very firmly adhering. A steel scalpel was used to scrape it off.

The anode film was amorphous and appeared to have the composition of an iron salt of an organic phosphate. If it is assumed, for example, that iron is oxidized at the anode and forms a salt with the phosphate ester acid, e.g.,

Table 9-2

Changes in  $\epsilon\zeta$  and Conductivity of S drol 500A  
as a Result of Electrolysis

(Experiment No. 5, Table 9-1)

	$\epsilon\zeta$ (mv)	Measured A.C. <u>Relative Conductivity</u>
Initial fluid	400	1
After 313 hours of electrolysis	260	1.24

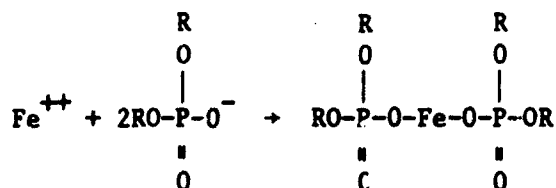
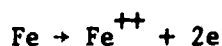
Table 9-3

## Analyses of Anode and Cathode Films

from Electrolysis of Skydrol 500A

(Experiment No. 5, Table 9-1)

<u>Analysis</u>	<u>Anode Film</u>	<u>Cathode Film</u>
X-ray diffraction	Amorphous	-
X-ray emission		
major ( $\sim$ 10%)	Organics	Na
minor ( $\sim$ 1-10%)	Fe, P	
lesser ( $\sim$ 0.1-1%)		Ca, Fe, P, Mg
trace ( $\sim$ 0.1%)	Mn, Mg, Cu, Al, Si, Cr	Cu, Al, Si
Mass spectrograph		
major	C, O, organics	Na, C, O
minor	Fe, P, H	
lesser	Mn, Mg, Al, Si	P
trace	Cu, Cr	Ca, Fe, Mg, Cu, Al, Si, H
Atomic absorption	10.7% Fe	-



then the iron content would be 11.8% for tributyl phosphate acid (MW=210). For a total charge of

$$(2050 \times 10^{-6} \text{ amps})(313 \times 3600 \text{ sec}) = 2320 \text{ coulombs,}$$

this reaction would give

$$\frac{(2320)(2 \times 210 + 55)}{(2)(96500)} = 6.7 \text{ grams}$$

The amount of material collected (0.135 gm) thus accounted for only 2% of this value. It is apparent that either an appreciable fraction of this assumed product was soluble or that other reactions occurred giving soluble products.

The cathode product appeared to have a composition of something like sodium carbonate. The cathode film accounted for an even smaller part of the charge passed.

At high current densities an apparent limiting current density was reached as shown in Fig. 9-6 for the thin electrolyte cell. The initial current peak was consistent with a conductivity of  $10^{-7} \text{ ohm}^{-1} \text{ cm}^{-1}$ , although at applied potentials above 300 volts the current decayed too fast to get a reading on the strip chart recorder. The plateau value (at  $Q > 2 \text{ coulomb/cm}^3$  in Fig. 9-4) initially appeared to increase with

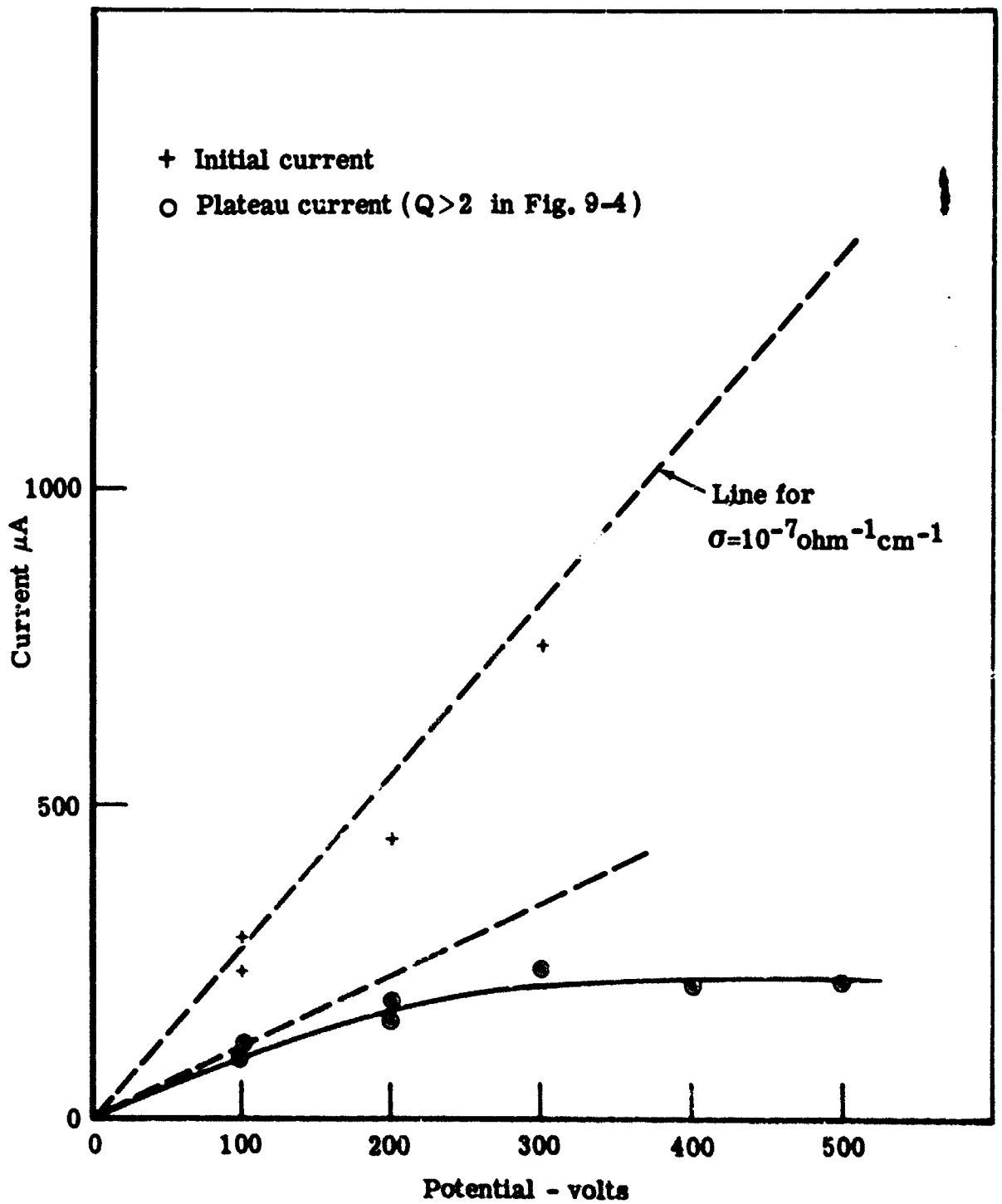


Fig. 9-6. Initial current and plateau current for thin electrolyte cell.

applied potential and then reach a limiting current density of about  $3 \times 10^{-4}$  amp/cm<sup>2</sup>. Further work would have to be done to establish whether this is a mass transport limit in the solid films on the electrodes or in the fluid.

At a potential of 400 volts or more across the thin cell (a field of 16,000 volts/cm), sparking occurred resulting in arc craters in the metal. A brownish and bluish coloration that occurred with or without sparks was sometimes observed on the electrodes at the high current densities. It was similar in appearance to coloration observed on iron surfaces in aircraft hydraulic valves near the damaged areas.

#### 9.2 Needle-to-Plane Cell Corrosion Experiments

After it was recognized that higher current densities would be necessary to obtain corrosion in the phosphate ester fluids the needle-to-plane cell illustrated in Fig. 9-7 was made. One electrode was a phonograph needle with a 0.001 inch tip radius and the opposing electrode was a polished steel block used in the high-pressure flow experiments (Sec. 5). Interelectrode spacing could be adjusted with the micrometer head holding the needle. With a potential of about one volt across the cell the needle was carefully moved down until it touched the block as indicated by a sharp increase in current. It was then backed off to a suitable spacing usually 0.001 inch. As in all of the electrolysis experiments, current was measured with a strip chart recorder connected to a 0.1% decade box as a shunt. In many of the runs a  $10^5$  ohm series limiting resistor was put in the circuit to protect the power supply in the event of arcing.

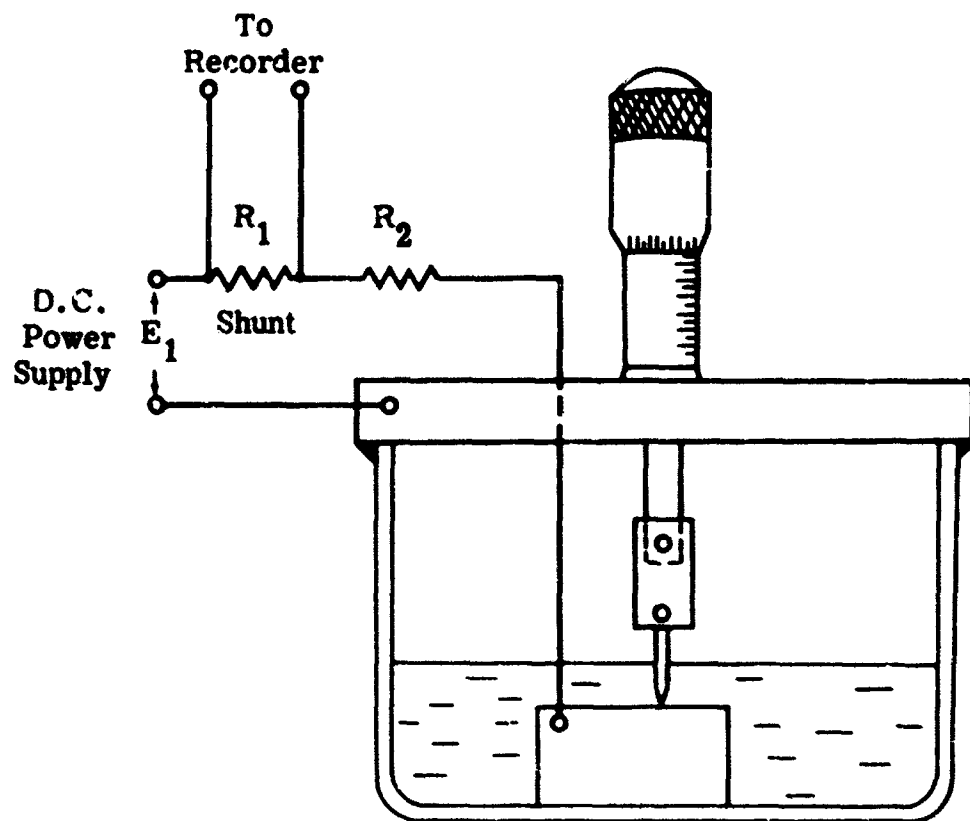


Fig. 9-7. Needle-to-plane cell.



The needle-to-plane cell was modified as shown in Fig. 9-8 to allow polarization studies on a smaller plane surface opposing the needle. Some corrosion experiments were also conducted with this cell.

Observations made during preliminary experiments with the needle-to-plane cell of Fig. 9-7 are summarized in Table 9-4. All of these runs were made at 500 volts and a needle-to-plane spacing of one mil ( $2.5 \times 10^{-3}$  cm). In run 1 with the plane negative the potential was increased stepwise to 500 volts and after a few seconds an audible spark occurred which produced the arc crater illustrated in the photomicrograph in Fig. 9-9. With a  $10^3$  ohm resistor in series in run 2 no sparks occurred in six minutes. A white film formed on the plane surface which could easily be rubbed off with a cotton swab and acetone and the metal surface underneath was undamaged.

When the plane was made positive in run 3, numerous small sparks occurred immediately. Increasing the series resistance to  $10^4$  ohms in run 4 decreased the severity and frequency of sparking further. When the series resistance was increased to  $10^6$  ohms in run 5 pitting corrosion was observed under the white film. A photomicrograph of the surface before cleaning is given in Fig. 9-10. The anodic pitting corrosion was very similar in appearance to the damage observed in aircraft hydraulic valves and was easily distinguished from the arc craters.

A series of experiments then conducted to study the anodic pitting corrosion in more detail is summarized in Table 9-5. Different fluids and additives and a range of applied potential were examined to determine their effect on the amount of pitting corrosion. The test was not really satisfactory in a quantitative sense but a relative scale of

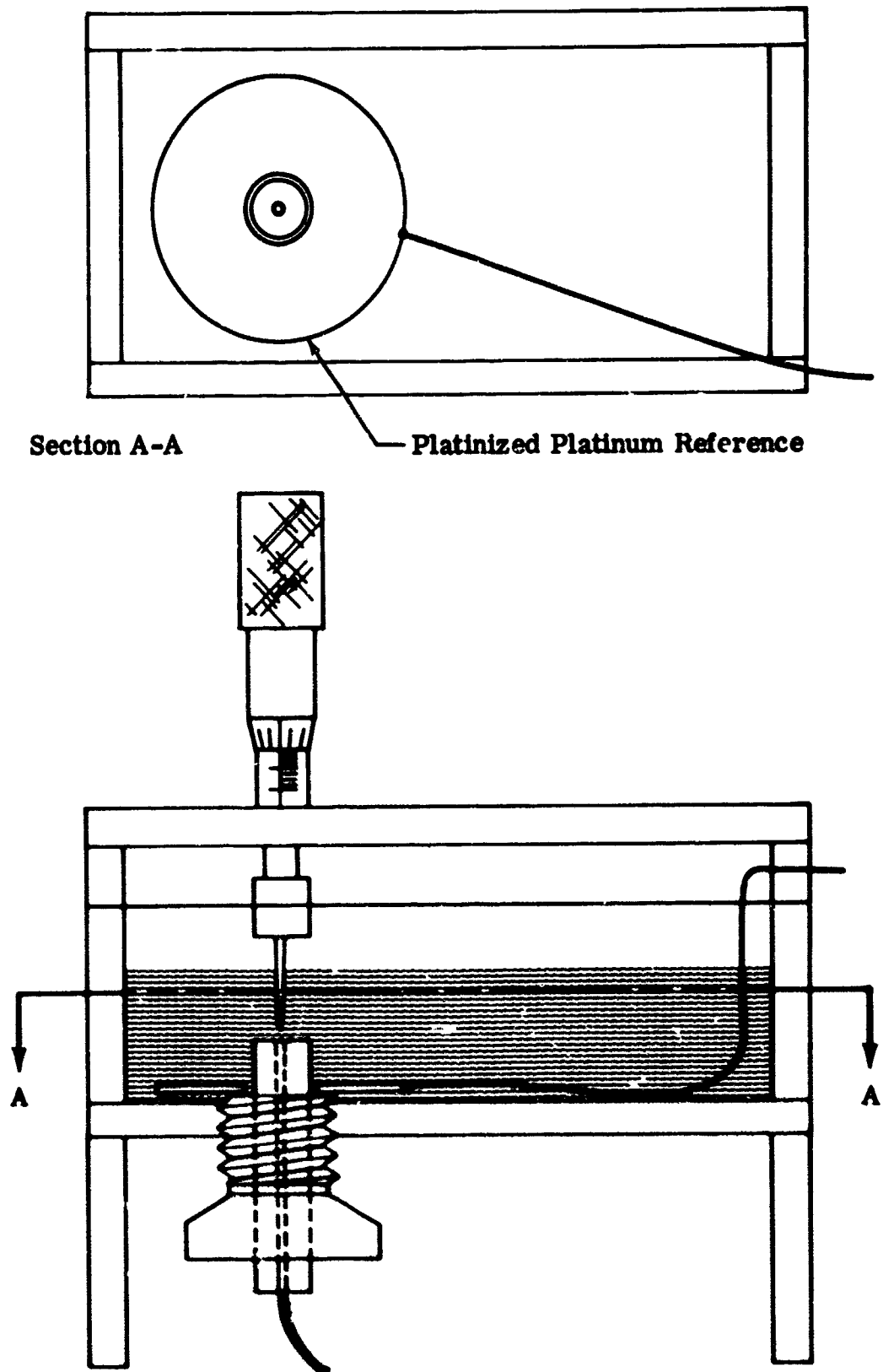
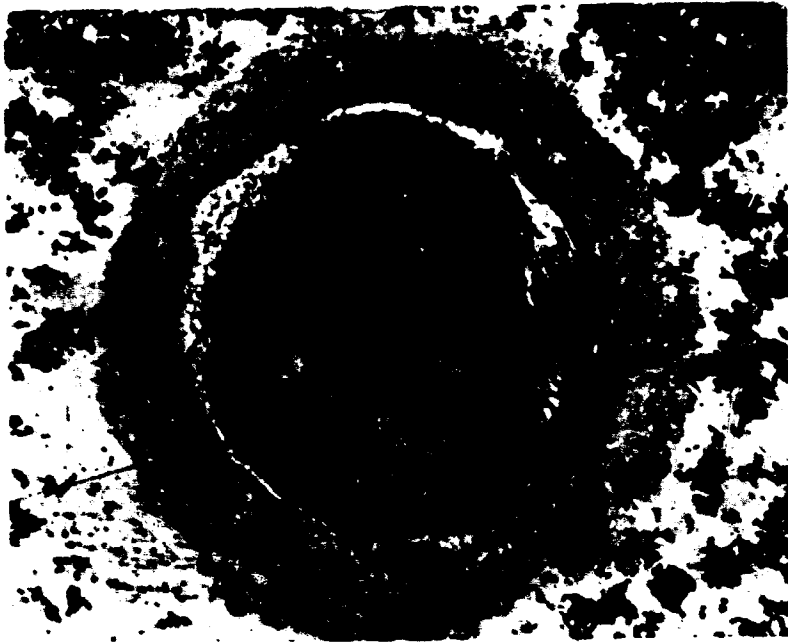


Fig. 9-8. Needle-to-plane cell for polarization studies.



200 X

Fig. 9-9. Arc crater produced in run 1.

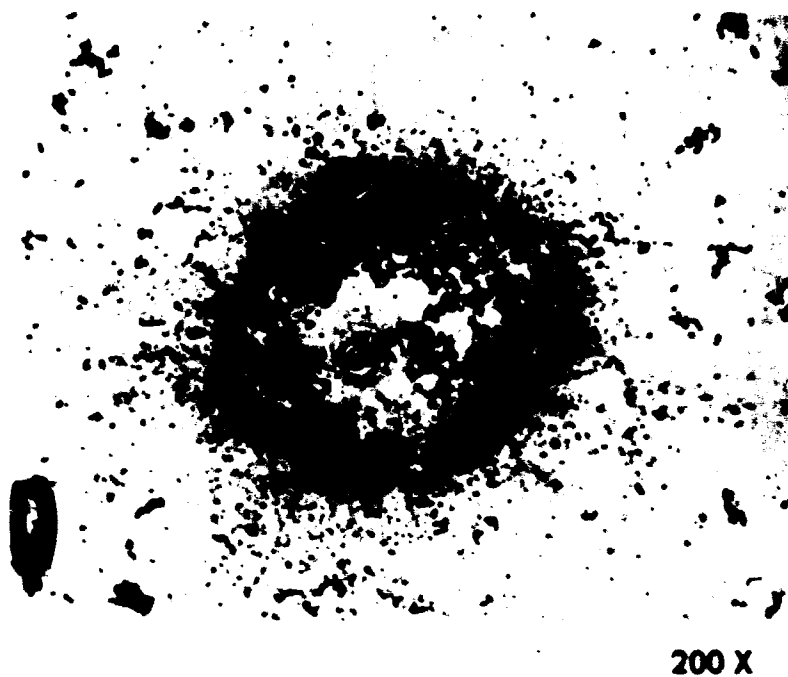


Fig. 9-10. Small arc crater, film deposit and pitting corrosion produced in run 5.

Table 9-4

Conditions and Observations for Preliminary  
Needle-to-Plane Experiments with Skydrol 500A

<u>Run</u>	<u>Polarity of plane</u>	<u>Series Resistance R<sub>2</sub> ohms</u>	<u>Duration of test (min)</u>	<u>Observations</u>
1	-	1	1	large spark and arc crater
2	-	10 <sup>3</sup>	6	white film, no spark, no damage to plane
3	+	10 <sup>3</sup>	(10 sec)	sparks
4	+	10 <sup>4</sup>	(20 sec)	sparks and small arc craters
5	+	10 <sup>6</sup>	1	few sparks and smaller arc craters, evidence of pitting corrosion

Applied potential E = 500 volts and interelectrode spacing

d =  $2.5 \times 10^{-3}$  cm in all runs.

Table 9-5  
Conditions and Observations for  
Needle-to-Plane Electrolysis Experiments

Run	Electrolyte	$\phi$ (volts)	I ( $\mu$ A)	$\tau$ (min)	q (Coulombs)	Cell Conductance $\times 10^6$ (ohm <sup>-1</sup> )	Relative Amount of Pitting
6	Skydrol 500A	250	40	55	0.131	0.16	5
7	"	170	26	70	0.109	0.15	2
8	" +1%CCl <sub>4</sub>	170	26	60	0.094	0.15	5
9	" +2%H <sub>2</sub> O	82	27	60	0.097	0.33	4
10	" +1%CH <sub>3</sub> NO <sub>2</sub>	170	15	95	0.085	0.09	Spark
11	" +0.1%CH <sub>3</sub> NO <sub>2</sub>	215	24	60	0.086	0.11	1
12	"	260	40	10	0.036	0.15	1
13	"	340	50	8	0.036	0.15	2
14	"	200	30	13.5	0.036	0.15	1
15	"	120	20	20	0.036	0.17	0
16	" +1%hydro- quinone	150	32	64	0.123	0.21	2
17	" +11%hydro- quinone	48	35	67	0.141	0.73	0
18	" +1%CCl <sub>4</sub>	80	70	60	0.25	0.9	10
19	Aerosafe base- stock	330	28	60	0.10	0.085	3
20	Aerosafe 2300	350	30- 40	60	~0.13	0.085-0.11	2

Interelectrode spacing  $d = 2.5 \times 10^{-3}$  cm in all runs

Series Resistor  $R_2 = 10^5$  ohms in runs 11-20

amount of pitting corrosion from 0 to 10 based on examination of depth of pitting under the microscope and area of pitting corrosion observed on photomicrographs of the corroded areas illustrates gross effects.

Run 6 produced a significant amount of pitting as indicated in the photomicrograph in Fig. 9-11. The maximum depth of the pitted area, determined by focusing a Reichert metallurgical microscope at 450x on the pitted zone and adjacent area, was about 4 microns. The approximate dimensions of the pitted area in relation to the needle electrode are indicated in Fig. 9-12.

The measured depth of pitting allows an approximate calculation of the current efficiency for the corrosion reaction. The upper limit for current density at the center of the pit would be approximately

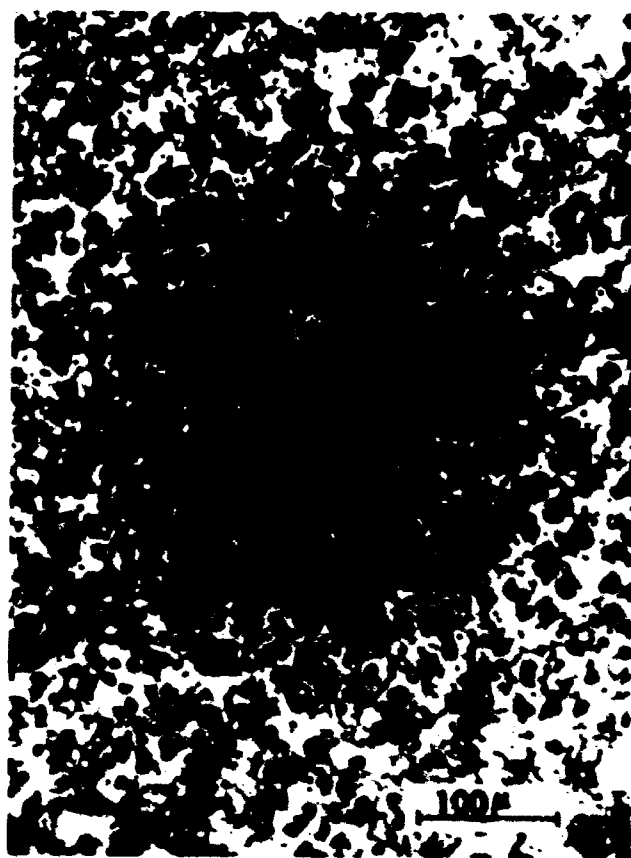
$$i = \sigma \frac{\Delta\phi}{d} \quad 9-1$$

A conductivity  $\sigma = 10^{-7} \text{ohm}^{-1} \text{cm}^{-1}$ , and an applied potential of 250 volts across a 0.0025 cm gap gives a current density  $i_{\text{max}} = 1 \times 10^{-2} \text{amp/cm}^2$ .

The thickness of metal removed by this current density would be

$$t = \frac{iM\tau}{zF\rho_d} \quad 9-2$$

A current density of  $10^{-2} \text{amp/cm}^2$  for 55 minutes assuming the iron corrodes to a valence of two gives  $t = 11$  microns. The minimum current efficiency of corrosion (based on the upper-limit current density) in the center of the pitted area was therefore about  $(4/11)(100) = 36\%$ .



200 X

Fig. 9-11. Pitted area in run 6 after removal of white film.



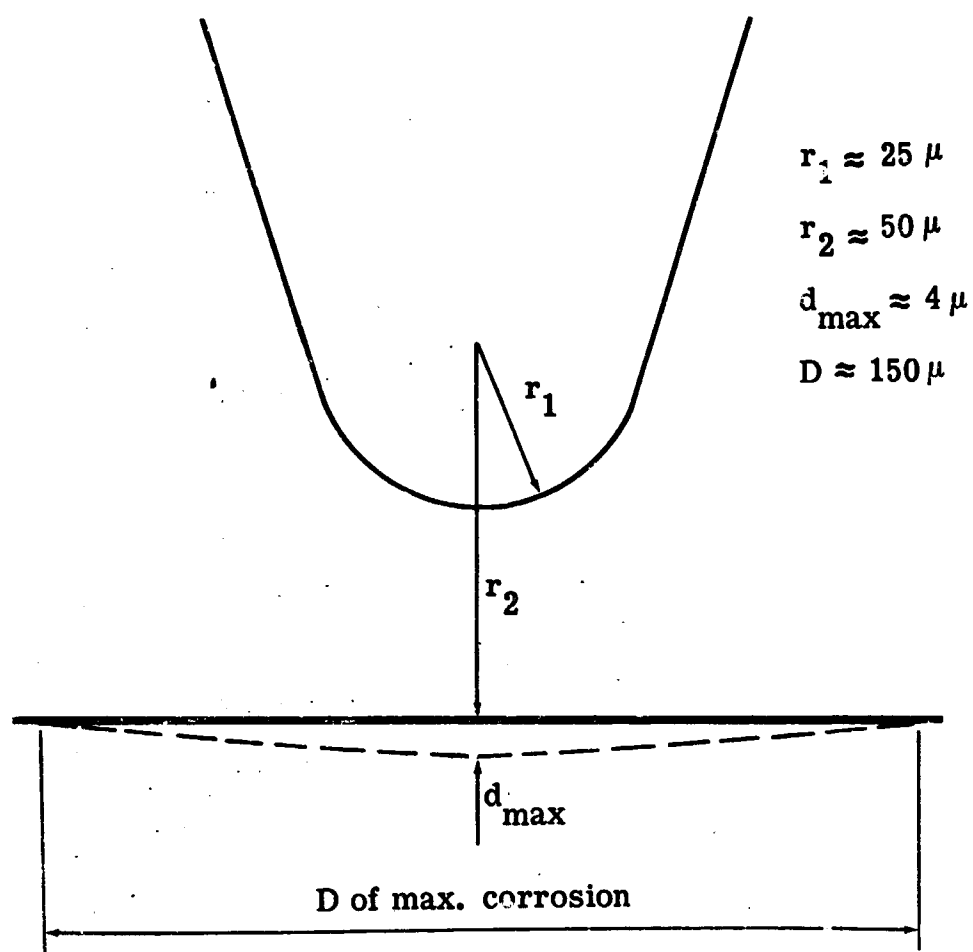
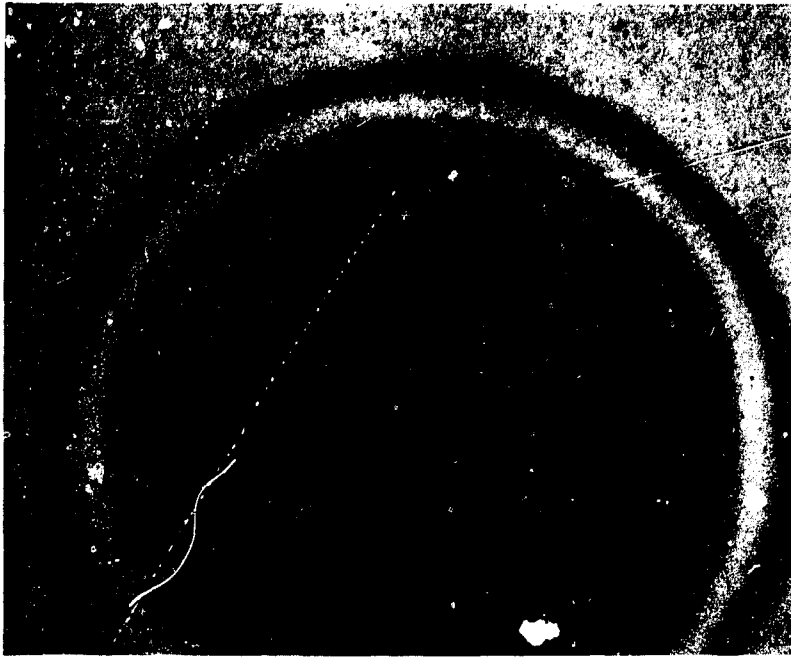


Fig. 9-12. Scale drawing of needle-to-plane experiment showing approximate dimensions of pitted area in run 6.

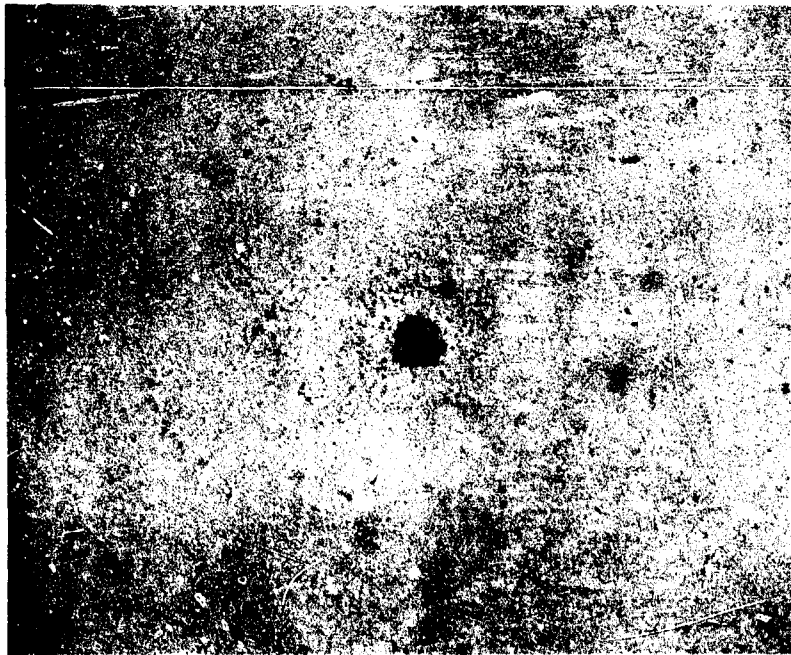
The average corrosion current efficiency for the whole surface based on the total volume of metal removed and the total charge passed was considerably smaller than this figure. The volume of the cone of metal removed as illustrated in Fig. 9-12 is about  $1 \times 10^{-7} \text{cm}^3$ . The amount of iron that would be removed by 0.13 coulombs to form valence-two iron is  $4.8 \times 10^{-6} \text{cm}^3$ , giving an average current efficiency of about 2%. The relatively low average current efficiency compared to the value in the center of the pitted zone may be attributed to the electrochemical formation of the white film in the areas of lower current density. It is shown in Appendix 14.4 that most of the current flows to areas on the steel block around the zone of maximum pitting. The formation of the white film occurs in preference to significant corrosion of the iron at low current densities as observed in the parallel-electrode cell studies.

The amount of pitting decreased significantly at a lower applied potential and current in run 7. The depth of pitting was less than one micron and could not be determined with the microscope. Photomicrographs of the white film and the pitted area after removal of the film are shown in Fig. 9-13. The diameter of the area covered with deposited film is seen to be more than ten times that of the area of maximum pitting. The film is for the most part white except for color fringe areas around the edge and for a brown coloration over the pitted zone. The brown coloration is presumably due to iron corrosion products.

The similar appearance of pitting of iron in the phosphate ester fluid to pitting of iron in aqueous solutions suggested that the phenomena might be similar. Pitting corrosion of iron in aqueous solutions is known



50 X



50 X

Fig. 9-13. White film and corroded area from run 7.

to occur in the presence of halide ions. It was reasoned that carbon tetrachloride, an organic halogen compound, might be a pitting corrosion agent in an organic electrolyte.\* One percent of carbon tetrachloride added to the electrolyte in run 8 increased the amount of corrosion compared to run 7 for otherwise the same conditions. Photomicrographs of the surface after cleaning are shown in Fig. 9-14. The average maximum depth of pitting was 3.1 microns giving a current efficiency of 35% in the center of the pitted zone based on Eqs. 9-1 and 9-2. This experiment has an important bearing on the valve damage problem as it suggests that decreasing the concentration of residual chlorine compounds might avoid pitting corrosion even with the generation of a streaming current. Further experiments are reported later in this section.

The effect of water addition was investigated in run 9 with 2% added water. The electrolyte conductivity increased by about a factor of two and a lower applied potential was used in order to obtain the same current as in runs 7 and 8. This addition of water appeared to have increased the amount of white film and the tendency for pitting in respect to the as-received fluid as noted in the photomicrograph in Fig. 9-15. A small arc crater is also observed on one side of the deeply pitted zone. A significant difference between this run and the conditions in the valves is that a constant current was maintained here, whereas in the valves the wall current may decrease due to the white film (see Sec. 11.3 and Appendix 14.6.3). More work should be done to evaluate the effect of water additions.

---

\* Although carbon tetrachloride is not appreciably ionized in solution it may react in the high field at the electrode surface.

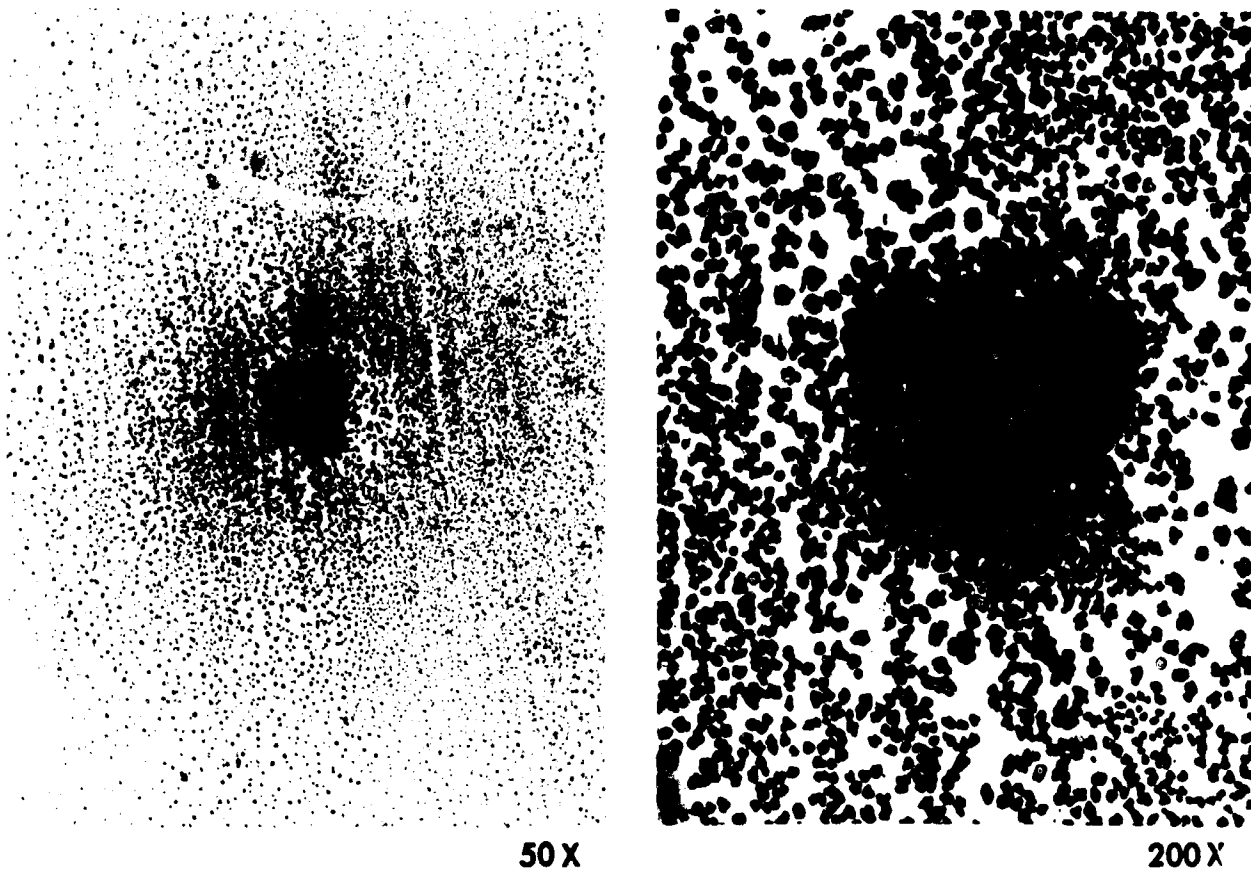


Fig. 9-14. Pitted area in run 8 with 1%  $\text{C Cl}_4$  after removal of the solid film.

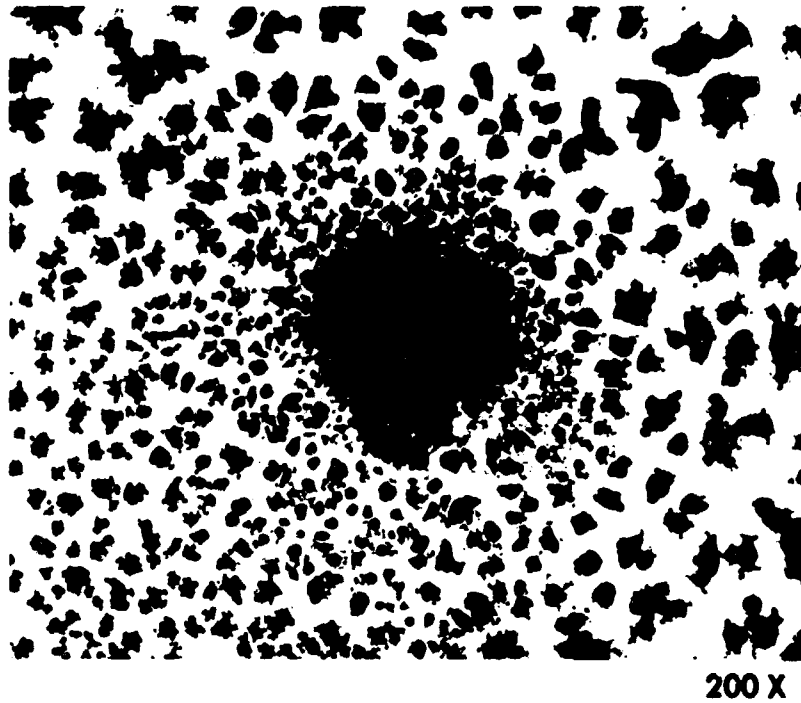


Fig. 9-15. Corroded area from run 9 with 2% added water, after removal of film.

Nitrates and other oxyanions are inhibitors for pitting corrosion in aqueous solutions so nitromethane, an organic analog, was tested in runs 10 and 11. At the one-percent level in run 10 the conductivity was significantly decreased. Sparking occurred and it was not possible to increase the level of current to that of runs 7 to 9. No corrosion was evident around the spark crater. At the 0.1 percent level in run 11 and nearly the same current level as in runs 7 to 9 the pitting appeared to be somewhat decreased but the results were not definitive. Further more-careful work would have to be done to establish if nitromethane is a pitting corrosion inhibitor in phosphate ester fluids.

Runs 12 to 15 were made for further verification of the effect of current density on the amount of pitting. These runs were made at different applied potential and current but with the same total charge passed. The amount of pitting was negligible at a current of 20 A but increased rapidly with increasing current suggesting a threshold current density for corrosion. The threshold level for corrosion was not accurately determined, however, because runs 12 to 15 were too short for accurate evaluation.

Additions of hydroquinone were made in runs 16 and 17 to determine if an easily oxidizable material would consume current in preference to pitting corrosion. At the 11% level (approximately one mole/liter) in run 17 pitting was virtually eliminated for a condition of current density and time which would otherwise have produced a large amount of pitting. It was also noted earlier that the conductivity of the fluid was increased several fold by the 11% hydroquinone addition.

A second run with 1% carbon tetrachloride set up as a demonstration run is also reported here. For an unknown reason the conductivity of this fluid was about six times higher than normal. The fluid containing the added carbon tetrachloride had been in an open beaker exposed to the laboratory atmosphere for several days and may have absorbed some HCl fumes. Whatever the cause of the increased conductivity, the current was high and a large amount of damage occurred as indicated in Fig. 9-16.

Aerosafe basestock and formulated fluid were used in runs 19 and 20. The experiments were not sensitive enough to determine if there was a significant difference between the formulated fluids from the two vendors (i.e., run 20 versus runs 6 and 7) but significantly more corrosion was obtained with the basestock as shown in Fig. 9-17. The damage was greater with the basestock in spite of a lower current density. It might be concluded from these experiments that some of the additives are preferentially oxidized in respect to basestock or iron or that they inhibit corrosion.

Further corrosion experiments were conducted with the needle-to-plane cell of Fig. 9-8 to determine if the distillation-purified, low-chlorine, basestock produced less corrosion. The purified tributyl phosphate gave essentially no corrosion as indicated in Fig. 9-18. The small dark area is where the needle electrode poked into the disk during adjustment of the spacing. The spots strung like beads along the polishing scratches were not pits but were seen to be bluish stains at higher magnification. The current averaged only 3 1/2  $\mu$ amps rather than the desired 4  $\mu$ amps during this experiment because the fluid had a high resistivity



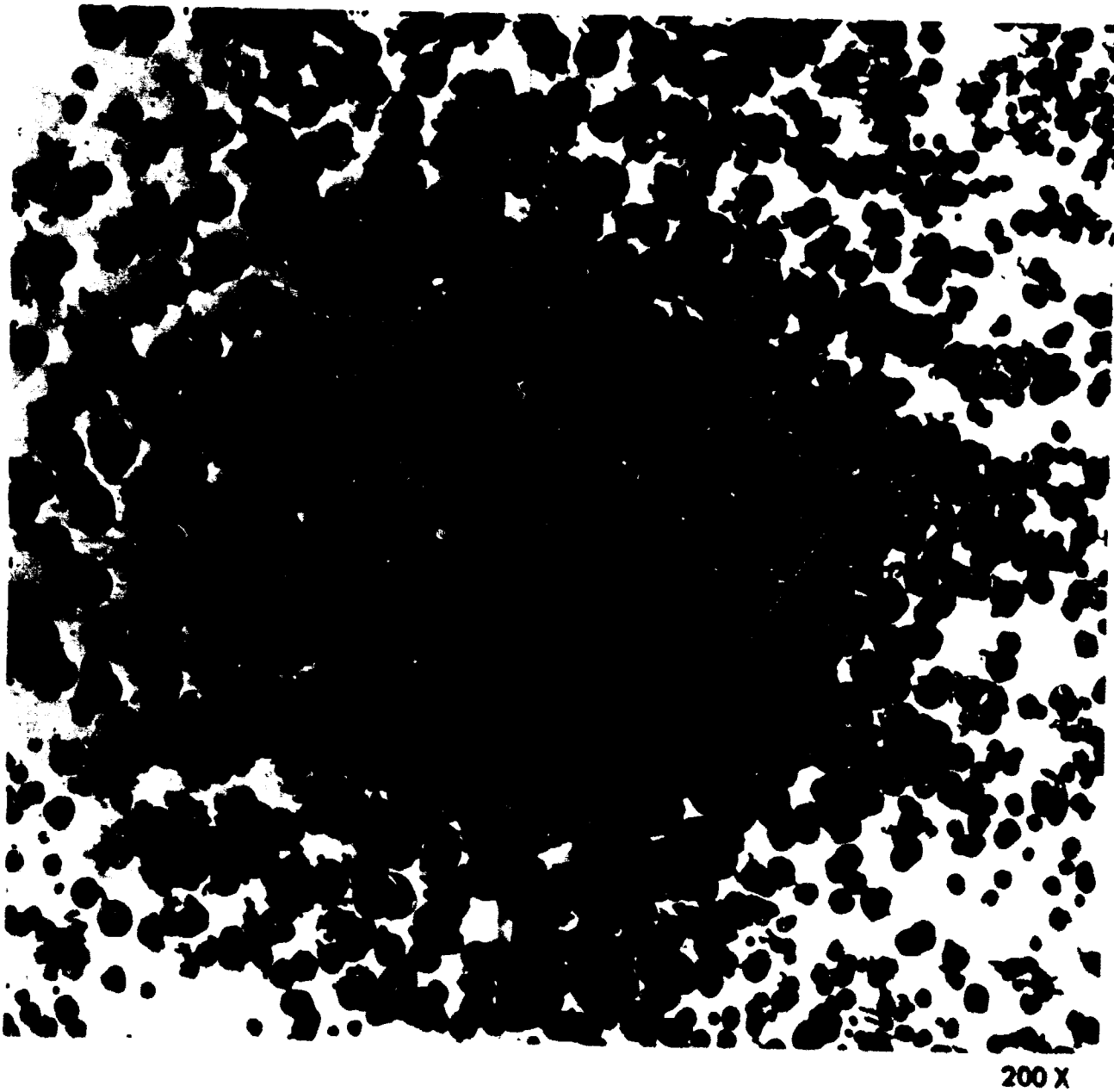
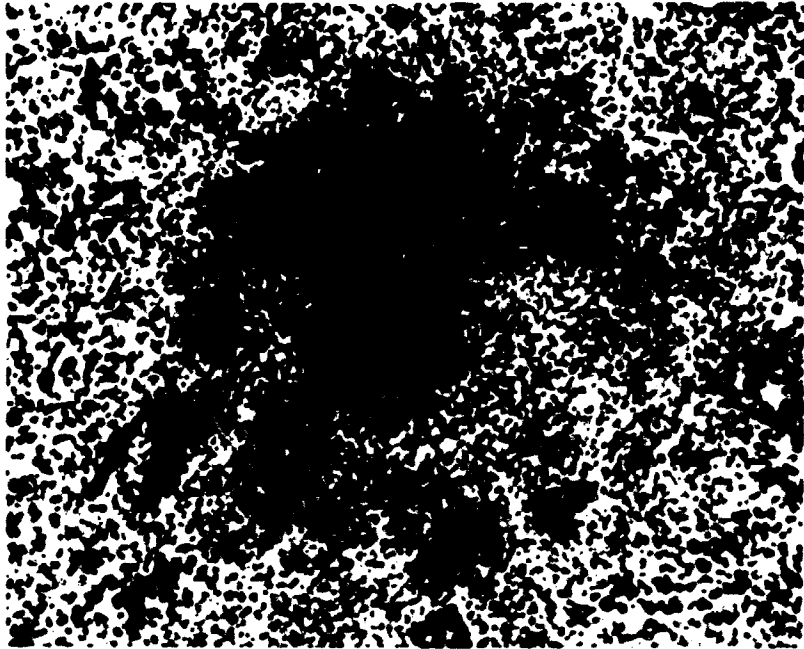


Fig. 9-16. Pitted area in run 18 with 1X C Cl<sub>4</sub> after removal of film.

9-85

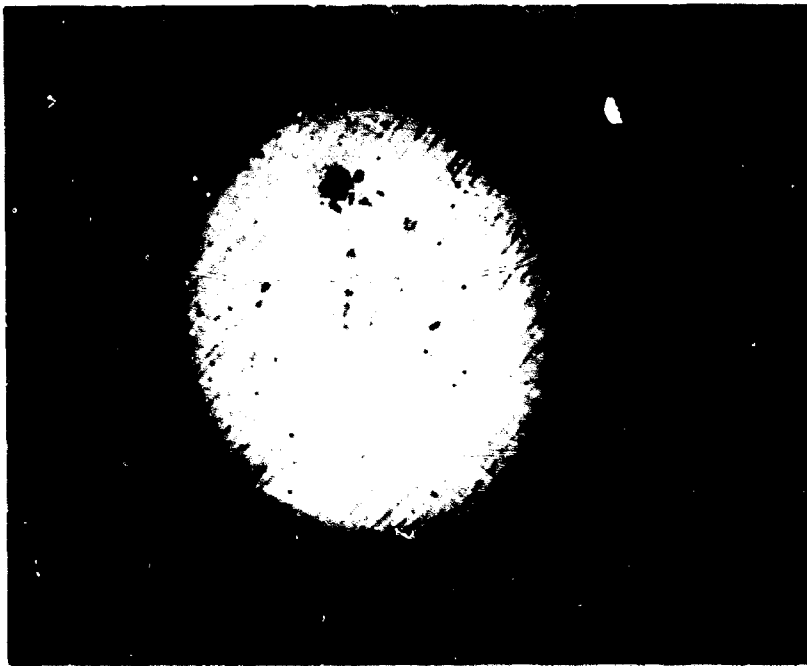


200 X



200X

Fig. 9-17. Pitted areas in runs 19 and 20 after removal of film.



60X

Fig. 9-18. Result of run in purified tributyl phosphate  
at 3.5uamp for one hour.

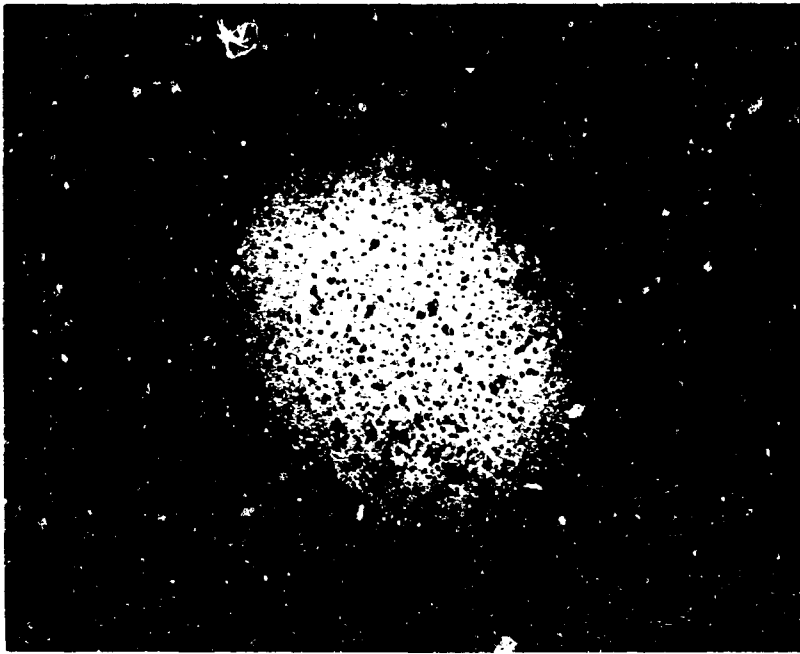
and this was the maximum current obtainable with the 500 volt power supply. The current fluctuated wildly during this experiment as if sparking were occurring.

The resulting corrosion from one-hour electrolyses in tributyl phosphate with 21 ppm chlorine is shown in Fig. 9-19 for comparison. (It is noted that the amount of corrosion more than doubled at a current of 4  $\mu$ amp compared to 2  $\mu$ amp, consistent with earlier findings. The maximum depth of corrosion in the heavily pitted area under the needle in the 4  $\mu$ amp experiment was about one micron.) Corrosion in basestock (a mixture of phosphate esters containing 46 ppm chlorine) was similar to that in tributyl phosphate shown in Fig. 9-19. The results of these experiments suggest that valve damage might be eliminated in low-chlorine fluids even if a streaming current is generated.

Some 1-chlorobutane equivalent to 250 ppm chlorine was added to the purified basestock to determine if chlorine in this form is damaging. Only slight corrosion occurred in a one-hour run at 3 1/2  $\mu$ amps, indicating that it is necessary to have the chlorine present in a more reactive form for corrosion to occur.

### 9.3 Anode Polarization in Phosphate Ester Fluids

Measurement of the working electrode potentials in the high resistivity phosphate ester fluids posed difficult problems that were only partially solved. Because cell potentials of up to several hundred volts were required to obtain the desired current density, even with a 0.001 inch spacing, a current interrupter technique was necessary to measure working electrode potential. Further, the small wick area of a



60X



60X

Fig. 9-19. Corrosion in tributyl phosphate.

saturated calomel reference electrode (SCE) gave such a large resistance on the phosphate ester electrolyte side of the junction that it was not acceptable. Capacitance coupling between the SCE and the micrometer head when the cell circuit was opened gave unacceptable spurious signals. A platinized platinum electrode in the form of a ring located axially in respect to the working electrode was found to be a more satisfactory reference. It established a reasonably constant rest potential that by coincidence was usually within  $\pm 100$  mv in respect to SCE. Steady-state calibrations of the reference potential were made against SCE with a Keithley 610 BR electrometer during each experiment.

The circuit used in the measurements of electrode polarization is given in Fig. 9-20. The current in the anode-cathode circuit was switched off and the electrometer was switched on to the platinum reference electrode by the ganged toggle switches  $S_1$  and  $S_2$  respectively. It was necessary that the electrometer be disconnected while current flowed through the cell because the reference electrode located in the electrolyte between the anode and cathode assumed a potential which overloaded the electrometer. Because of the high impedance of the electrolyte the toggle switches were insulated and shielded from each other by mounting on a 1/4 inch Plexiglas sheet on a two-compartment grounded metal box. They were ganged by means of a Plexiglas block cemented to their handles.

In order to avoid a sudden jump in potential when  $S_2$  was connected to the electrometer,  $S_2$  was connected to an adjustable bias potential while  $S_1$  was in the closed position. The IR-free potential of the electrode under study was taken as the bias potential at which there was

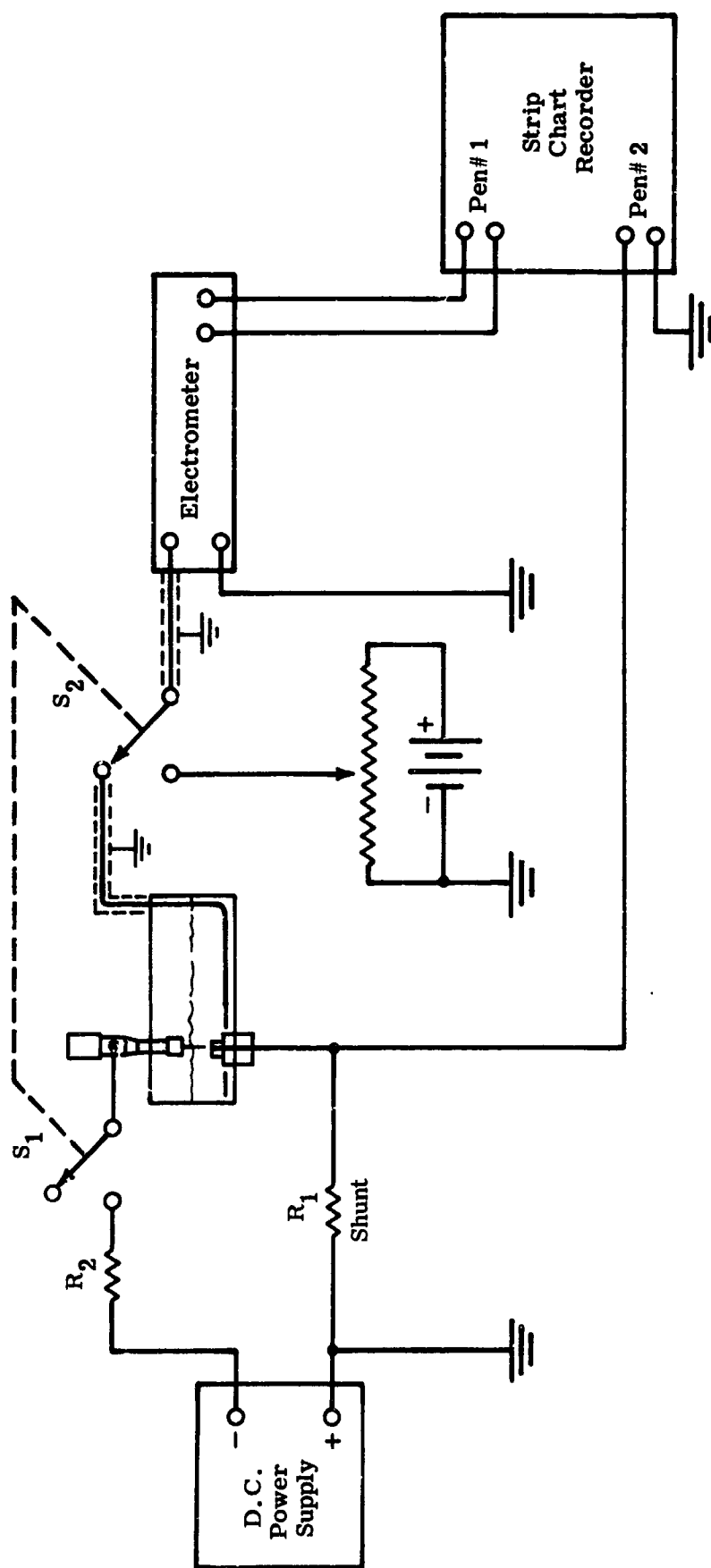


Fig. 9-20. Electrical circuit for electrode polarization studies.

no blip on the strip chart recorder at switching. For small polarization this was satisfactory but for larger polarizations (greater than 2 volts) the initial decay of overpotential was so fast that the reading was very inaccurate. A repetitive switching circuit in which relays driven by a signal generator were substituted for  $S_1$  and  $S_2$  and the signal was displayed on an oscilloscope was tried but solving the transient problems associated with the high impedance cell was considered to be beyond the scope of the present investigation.

Anodic current-potential curves for Aerosafe 2300 fluid and the phosphate ester basestock are shown in Fig. 9-21. The anode was an iron wire potted in epoxy resin and polished on the exposed end. The exposed end had a diameter of  $10^{-1}$  cm and area of about  $10^{-2}$  cm<sup>2</sup>. Both fluids were said by the vendor to contain about 50 ppm of chlorine in the form of chlorobutane.

The anode polarization became too large to measure for both the formulated fluid and basestock at a current density of about  $3 \times 10^{-5}$  amps/cm<sup>2</sup> based on the total anode area. The polarization appeared to decrease at higher current densities in the basestock. A significant amount of pitting occurred in the basestock experiment but little pitting occurred in the experiment with formulated fluid. This suggested that the decrease in polarization at higher current densities and the lower polarization with decreasing current for basestock may have been due to onset of pitting corrosion. Higher polarization and less pitting in formulated fluid perhaps could be attributed to corrosion inhibiting additives.

Anodic current-potential curves for distillation-purified basestock with 2 ppm residual chlorine and the same material with approximately



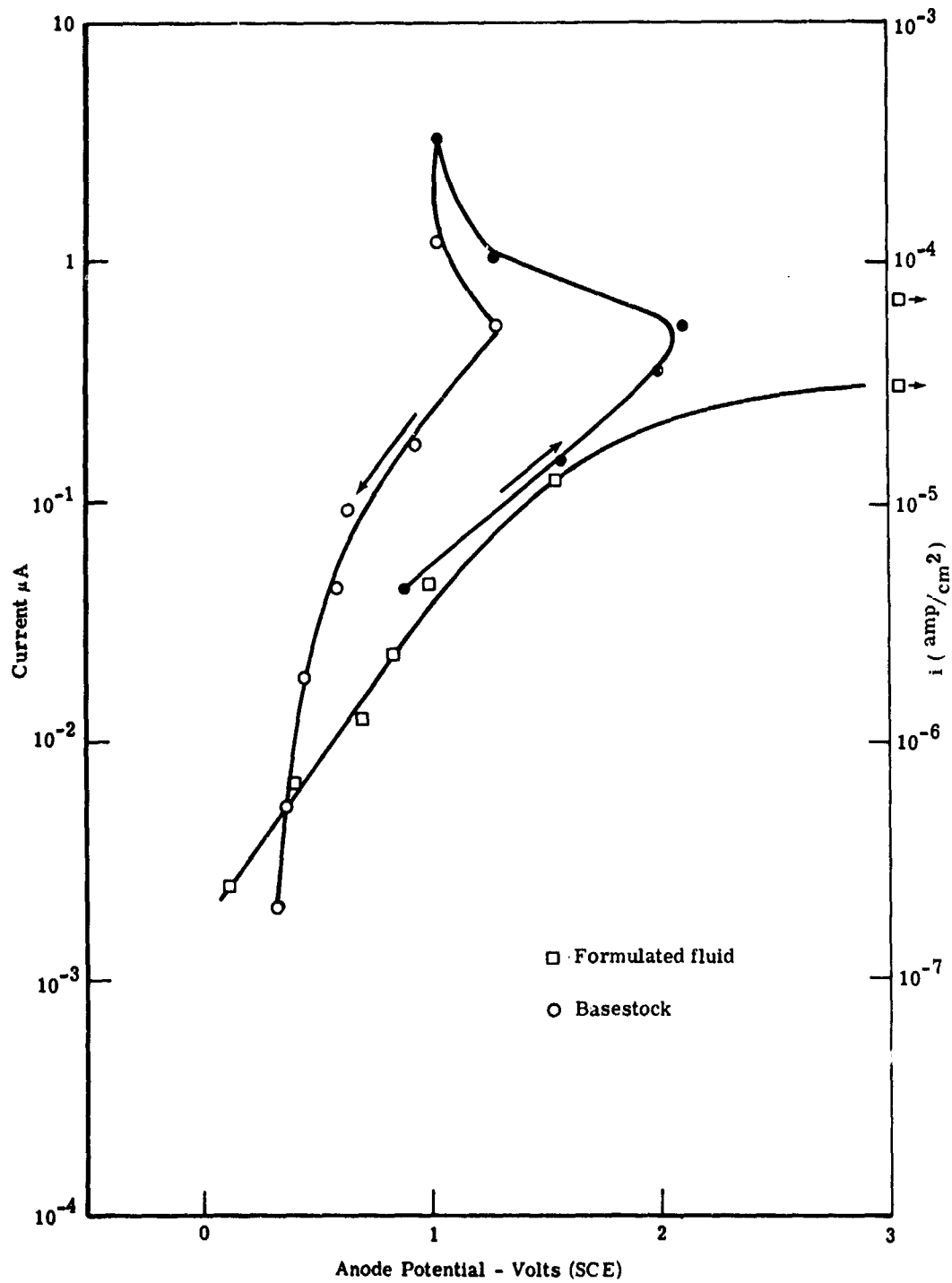


Fig. 9-21. Anodic current-potential curves for iron in phosphate ester fluids. Anode area  $10^{-2} \text{cm}^2$ , solid symbols for increasing current, open symbols for decreasing current.

2000 ppm added chlorine in the form of 1 chlorobutane are shown in Fig. 9-22. The purified basestock had a polarization curve similar to the formulated fluid as shown in Fig. 9-21. The solution with added 1 chlorobutane in general produced a lower polarization. Pitting was observed in the latter solution but not in the pure purified basestock. (The amount of added 1 chlorobutane here was nearly 10 times greater than in the experiment described in Sec. 9-2 in which no significant pitting occurred.)

#### 9.4 Conclusions

The following conclusions are made for electrolysis of phosphate ester fluids under non-flow conditions.

1. Solid high-resistance films form on iron electrodes in phosphate ester fluids at low current density, e.g.,  $10^{-4}$  amp/cm<sup>2</sup>. The anode film is amorphous, contains about 10% iron and has a composition otherwise similar to the phosphate ester. The current efficiency for oxidation of iron is about 2%. The cathode deposit contains predominantly sodium, carbon and oxygen.
2. There is a limiting current density of  $\sim 3 \times 10^{-4}$  amp/cm<sup>2</sup> at which a steep increase in potential occurs.
3. Pitting corrosion of iron occurs at an anodic current density greater than  $\sim 5 \times 10^{-5}$  amp/cm<sup>2</sup>. The current efficiency for corrosion is at least 35% at a current density of  $10^{-2}$  amp/cm<sup>2</sup>.
4. Pitting corrosion is promoted by addition of carbon tetrachloride to the fluid but is essentially eliminated when the chlorine content of the fluid is decreased by distillation to 2 ppm.

5. Corrosion can be inhibited by addition of an easily oxidizable material such as hydroquinone.

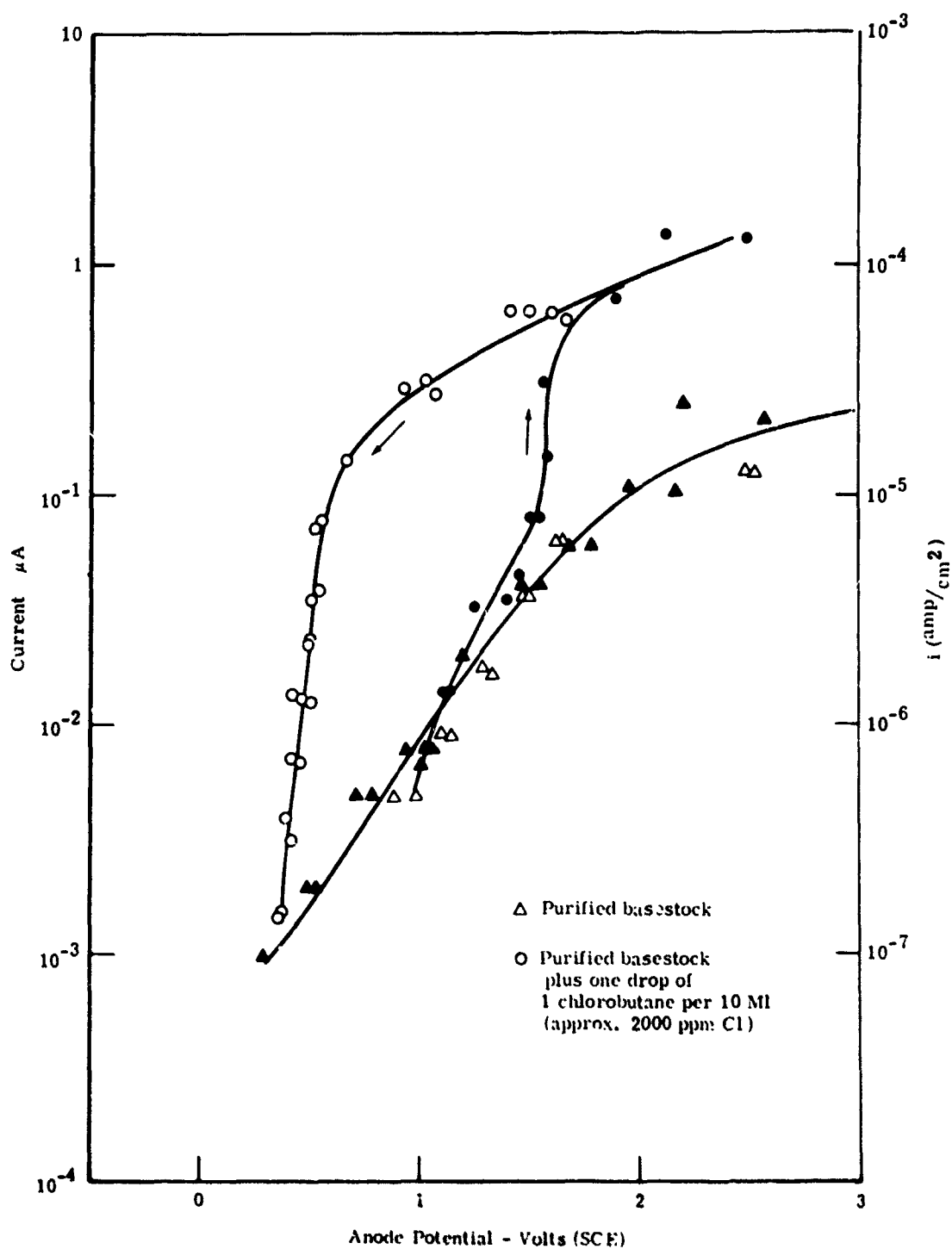


Fig. 9-22. Anodic current-potential curves for iron in phosphate ester fluids. Anode area  $10^{-2}\text{cm}^2$ , solid symbols for increasing current, open symbols for decreasing current.

### 10.0 COUPLED STREAMING CURRENT AND SPARK DISCHARGE

If a streaming current generated by fluid flow is carried into a container, for example, when a storage tank is being filled with a pipe, high potentials can be generated and electrical breakdown may occur [5]. It was considered possible that a similar process may be occurring in hydraulic valve systems, resulting in some form of unwanted electrical discharge machining.

When an electrical charge is deposited in a liquid of conductivity  $\sigma$  and dielectric constant  $\epsilon$ , contained in a grounded metal can, approximately half of the charge will leak to ground in a time given by [5] as

$$\tau = \frac{\epsilon \epsilon_0}{\sigma} \quad 10-1$$

$\tau$  is known as the relaxation time, and is essentially independent of the geometry or size of the container.

A rough indication of the average charge in the system may be obtained from

$$Q = I_s \tau \quad 10-2$$

where  $I_s$  is the streaming current. Dividing  $Q$  by  $l_s$ , some characteristic dimension of the system gives a measure of the potentials which may be generated. Obviously, the larger  $I_s$  and the smaller  $\sigma$  are the greater is the possibility of breakdown.

For highly refined petroleum products  $\tau$  can have values as large as  $10^4$  sec. Skydrol 500A with a conductivity of approximately  $10^{-7}$  mhos/cm and a dielectric constant  $\epsilon$  of about 8 has a value for  $\tau$  of approximately  $10^{-6}$  sec.

Rough estimates of the magnitude of the potentials generated in the valve orifices indicated that spark breakdown would be unlikely, however, a search was made for sparks in the apparatus of Fig. 5-1 by inserting a small sapphire window in one of the metal blocks near the metering orifice. Observations through the window with a photomultiplier indicated no sparks. The window was replaced with a fine wire embedded in epoxy, to be used as an antenna to detect electrical noise from sparks. No such noise was found, further eliminating the possibility of spark damage. However, a small steady positive electrical current was found to flow from the wire into the liquid.

The mechanism for the generation of this wall current is described in Sec. 7.

## 11.0 COUPLED STREAMING CURRENT AND CORROSION

### 11.1 High Pressure Flow Experiments

#### 11.1.1 Disk to Ring Current

In order to determine if the actual wall current generated in the orifice in the high pressure flow experiments (Sec. 7.2.2) was consistent with the measured amount of corrosion, the ring-disk electrode system shown in Fig. 11-1 was built. The steel ring and disk were cemented with epoxy resin and the surface was lapped as described earlier (Sec. 5). The ring-disk electrodes were aligned axially with the orifice within 1/2 thousandth of an inch by means of the alignment pin and shims. Streaming current was determined by measuring the potential across a  $10^5$  ohm resistor connected between ring and disk.

At a gap of 0.001 inch and a pressure drop of 2300 psi across the orifice, the ring-disk electrode system (Fig. 11-1) generated a current between ring and disk of 5 microamperes. On open-circuit at a pressure of 1900 psi across the orifice a potential of 70 volts was measured between ring and disk with a Keithley 610 electrometer. Current-potential curves with and without flow obtained for the ring-disk system by applying a potential between ring and disk with an external battery are shown in Fig. 11-2. The resistances calculated from the slopes are consistent with the value estimated from the fluid conductivity and system geometry (see Appendix 14.4). The apparent lower resistance with flow is probably due to the lip of the orifice getting into the circuit at the high potential gradient developed in the fluid with flow. Corrosion was observed on the downstream side of the lip in this experiment,

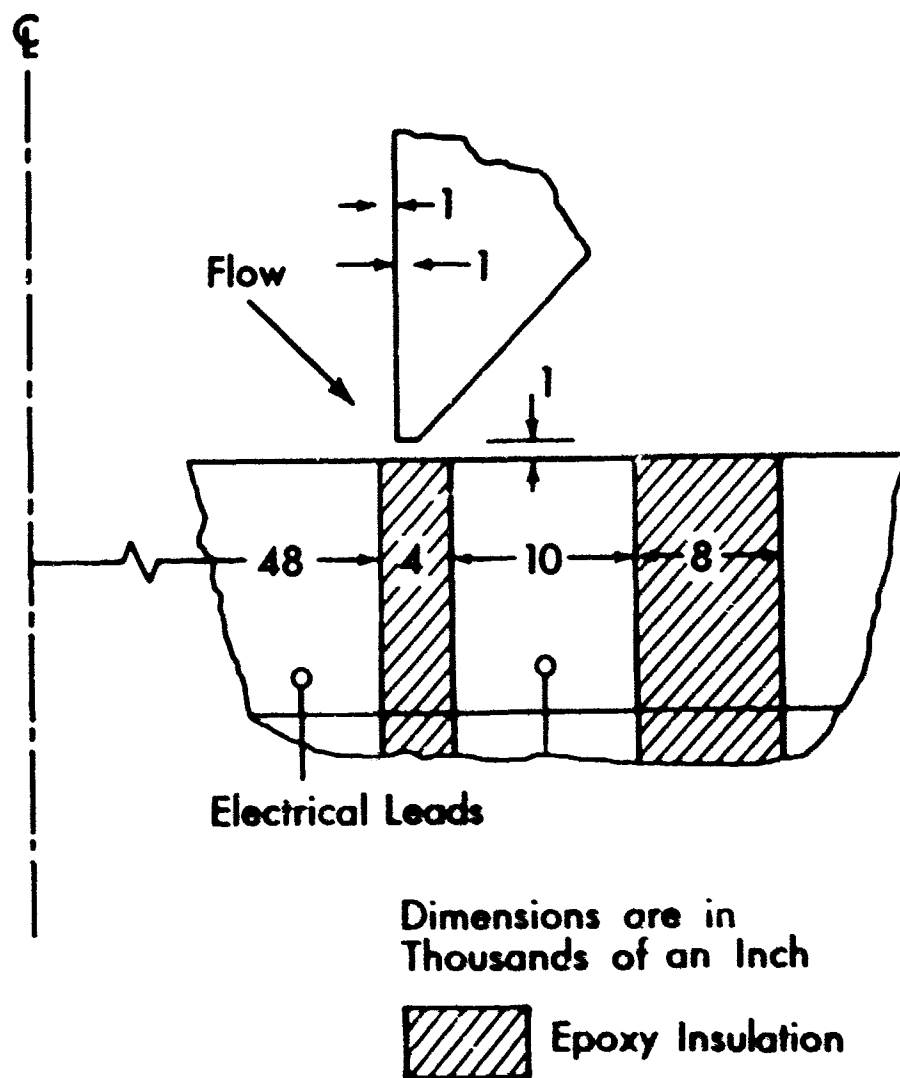


Fig. 11-1. Ring-disk electrode system for measurement of wall current.



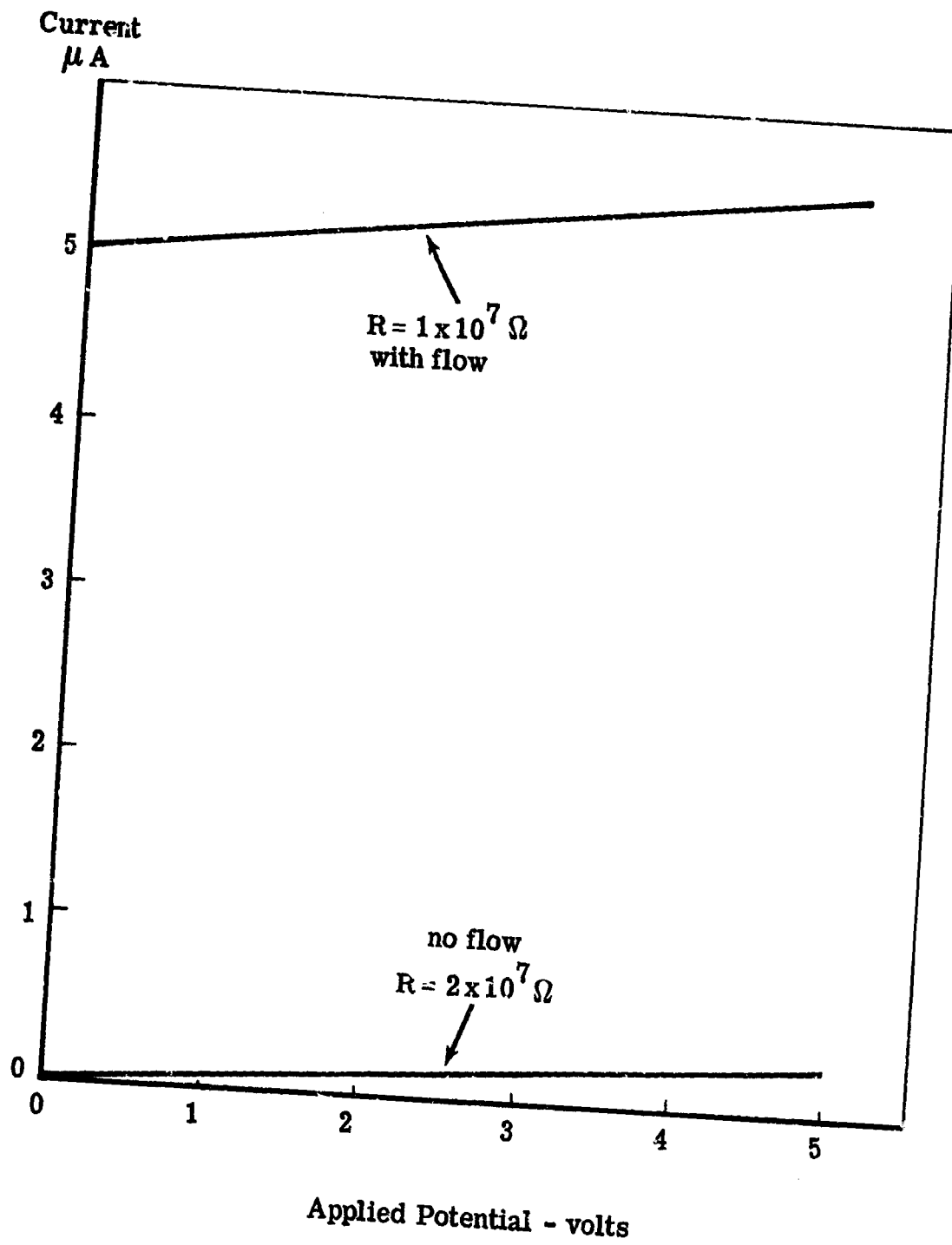


Fig. 11-2. Current-potential curves for ring-disk system with and without flow.

consistent with the lip getting into the ring-disk electrical circuit. It may be noted that the current-potential curve with flow extrapolates to a zero-current intercept of 100 volts, which is a rough check on the 70 volts measured at a lower flow rate. Unfortunately the corrosion was not uniform enough on the disk to make an estimate of the amount of metal removal to check with the total charge passed in the experiment but the current measured affords a means of comparison to the 28 1/2 hour wear test as is described in Sec. 11.2.1.

#### 11.1.2 Cathodic Protection

As a further test of the idea that the current flow was producing the damage by electrochemical corrosion, the apparatus of Fig. 5-1 was run with 90 volts applied between the flat specimen and the block containing the lip. After 6 hours of flow of Skydrol 500A with 2000 psi upstream and atmospheric pressure downstream, no damage was observed on the cathodic specimen. The anodic lip was damaged far more than usual.

This demonstration that cathodic protection is possible is of interest only as further evidence in support of the proposed damage mechanism. Cathodic protection of the valves would be very difficult and is not suggested.

#### 11.1.3 Insulating Specimen

As yet another test of the validity of proposed damage mechanism an aluminum oxide ceramic insert was set into the flat specimen block of Fig. 5-1 and run for 22 hours from 3000 psi to atmospheric pressure with Aerosafe 2300. At the end of the test no sign of damage was

observed on the ceramic as expected, and the metal lip had clearly been damaged. In ultrasonic cavitation experiments this same ceramic was more easily damaged than the hardened 52100 steel.

## 11.2 Comparison of Theory and Experiment

### 11.2.1 Comparison of Actual Metal Removal to Theory

The amount of metal removal occurring in a 28 1/2 hour wear experiment with Skydrol 500A under the conditions described in Sec. 5 is compared here to predictions from the theory of the streaming current coupled to a corrosion reaction.

The amount and the pattern of metal removal were determined by profile measurements with a Talysurf Model 3 instrument. An average profile determined from measurements for sixteen radial profiles is given in Fig. 11-3. (See Appendix 14.5 for data.) Comparing the metal loss pattern to shorter runs (see Fig. 5-2) it appears that corrosion starts at the upstream side of the lip but moves downstream as the leading edge of the lip is corroded away and the flat surface becomes pitted. Current densities corresponding to the amount of corrosion of iron along the average profile were calculated from

$$i = \frac{zF\rho_d t}{M\tau} \quad 11-1$$

in which the parameters listed in Table 11-1 were used. A plot of Eq. 11-1 is compared to the theoretical current density distribution, Eq. 7-11 (for the parameter values listed in Table 11-1) in Fig. 11-4. The current density for corrosion is in reasonable agreement with the streaming current theory in the range of 50 to 180 microns upstream

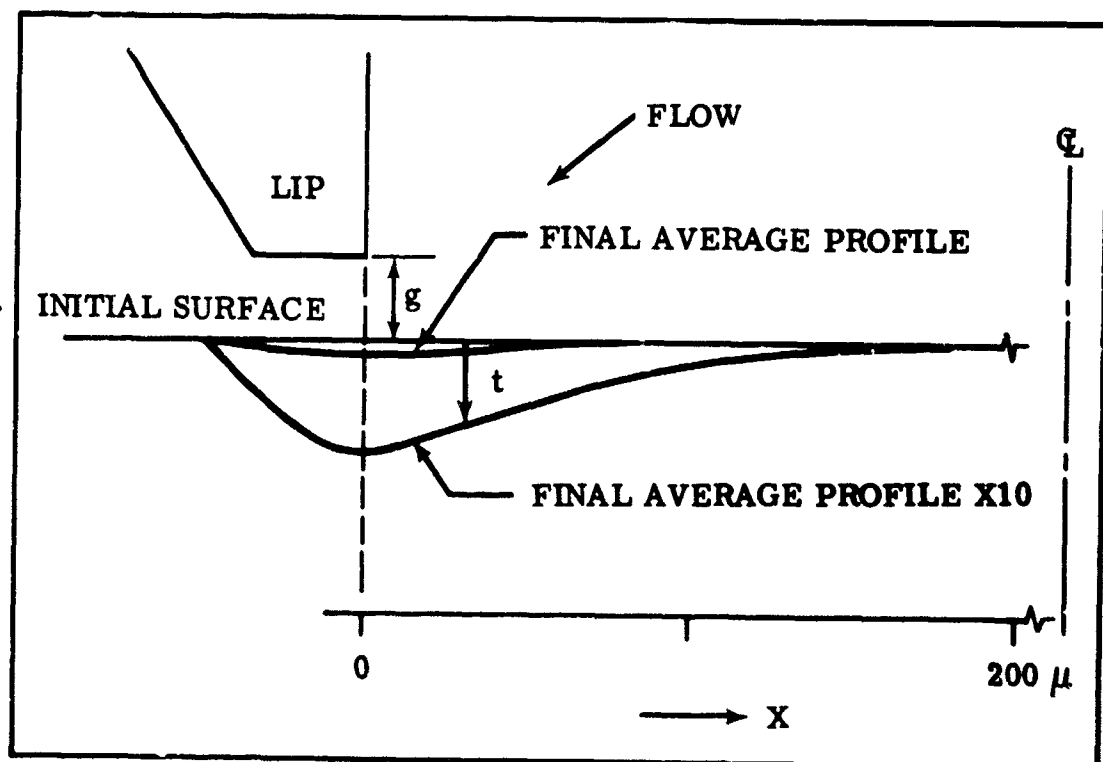


Fig. 11-3. Scale drawing of orifice showing final average profile.

Table 11.1

Values of Parameters used in Eqs. 11-1 and 7-11

for Fig. 11-4

---

$z$	= 2 (assumed that $\text{Fe}^{2+}$ formed)
$F$	= 96,500 Coulomb/equiv.
$\rho_d$	= 7.86 gm/cm
$M$	= 55.8 gm/mole
$\tau$	= $28.5 \times 3600$ sec
$\epsilon\epsilon_0$	= $7.1 \times 10^{-13}$ Coulomb/volt cm (for dielectric constant = 8)
$\zeta$	= 0.050 volt (for Skydrol, see Sec. 7.2)
$v$	= $0.1 \text{ cm}^2/\text{sec}$
$Q_{\text{initial}}$	= $19.5 \text{ cm}^2/\text{sec}$
$Q_{\text{final}}$	= $36.2 \text{ cm}^2/\text{sec}$
$Q_{\text{avg}}$	= $30.5 \text{ cm}^2/\text{sec}$ , $Q_{\text{avg}} = \frac{\sum_{i=0}^{i=n} Q_i^{3/2}}{n}$

---

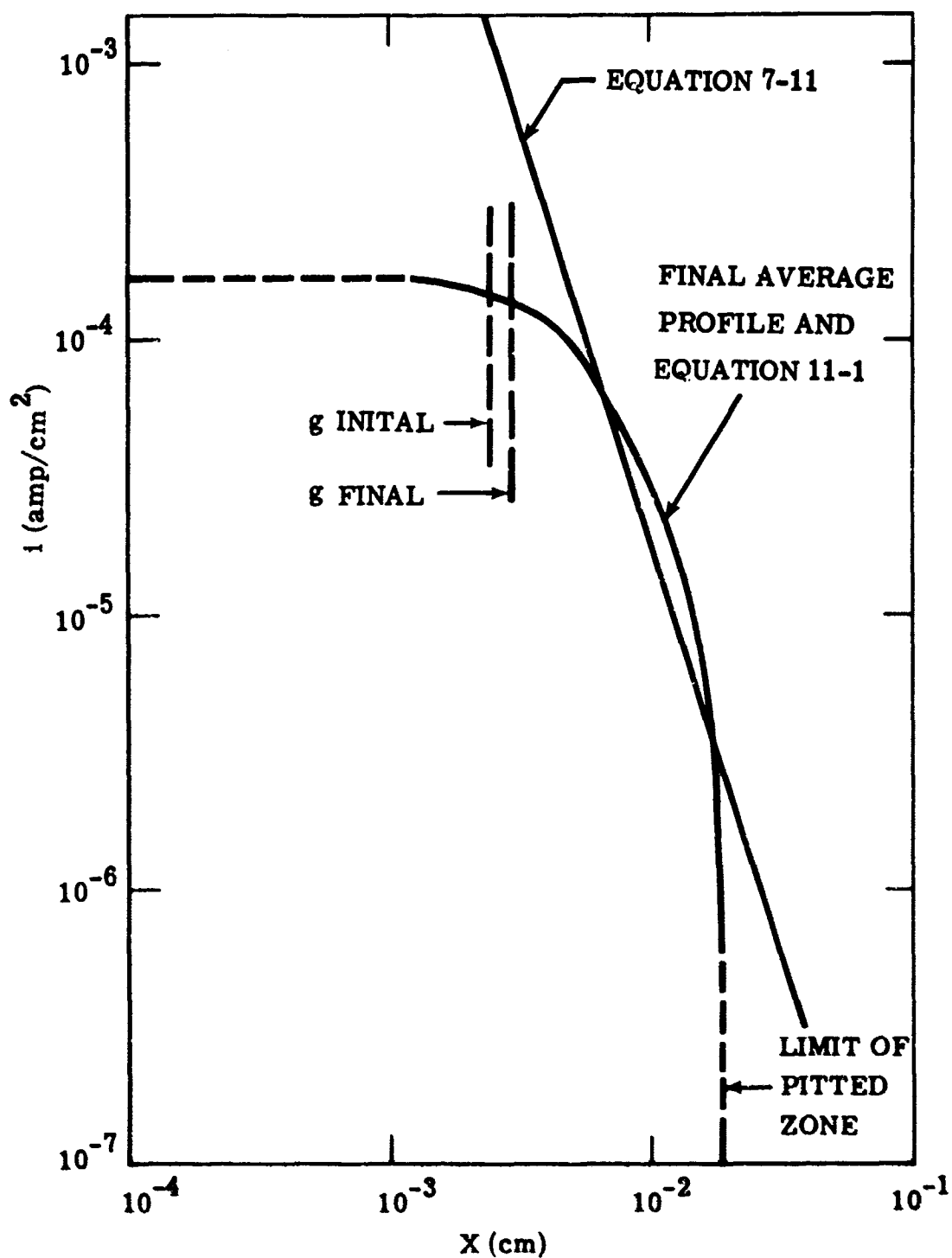


Fig. 11-4. Comparison of measured corrosion current density and streaming current theory.

from the lip. At about 190 microns from the lip there is a sharp cut-off in the pitting, suggesting that the wall current can be supplied by another electrochemical reaction at low current density. The limiting current density for this reaction appears to be  $\sim 3 \times 10^{-6}$  amp/cm<sup>2</sup> from the value of Eq. 7-11 at 190 microns.

The current density based on the profile also deviates below equation close to the lip. In part this is certainly due to the departure from the point-sink assumption in Eq. 7-11 at a position several gap widths upstream. Other factors may also be operating because the average current efficiency for pitting based on the total metal removed as compared to the wall current measured in the ring-disk experiment is only 20% as shown in Table 11-2. A disparity of this magnitude must occur in the high current density zone near the gap rather than in the low current density zone, suggesting that there may be a limit to the rate of pitting. This could be related to the concentration of chlorine containing compounds present or to conductivity of the fluid (see Appendix 14.6). Further work needs to be done to clarify this.

#### 11.2.2 Flow Damage in Various Fluids

Flow damage experiments were performed with two fluids other than phosphate esters and the results are shown in Table 11-3. The table shows that neither damage nor deposit formation occurs with fluids exhibiting little or no wall current as measured by the method of Sec. 7.2.1.

Table 11-2  
 Estimation of Average Current Efficiency  
for Corrosion in 28 1/2 hour Run

$$\text{C.E.} = \frac{\text{Volume of metal removed}}{\text{Calculated volume based on average current and time}} = \frac{V_m}{V_I}$$

$$V_m \approx \pi D A$$

$$\begin{aligned} D &= \text{diameter at inner edge of lip} \\ &= 0.23 \text{ cm} \end{aligned}$$

$$\begin{aligned} A &= \text{area of final average profile} \\ &= 6.57 \times 10^{-6} \text{ cm}^2 \text{ (Fig. 11-3 and} \\ &\quad \text{Appendix 14.5)} \end{aligned}$$

$$\therefore V_m = 4.75 \times 10^{-6} \text{ cm}^3$$

$$V_I = \frac{I T M}{z F \rho_d}$$

$$\text{(Eq. 11-1)}$$

$$\begin{aligned} I &= I_{R-D} \left( \frac{P}{P_{R-D}} \right)^{3/4} \\ &= (5 \times 10^{-6}) \left( \frac{3300}{2300} \right)^{3/4} = 6.5 \times 10^{-6} \text{ amp} \\ &\text{(Figs. 11-2 and 7-8)} \end{aligned}$$

Values of other parameters in Table 11-1

$$\therefore V_I = 24.6 \times 10^{-6} \text{ cm}^3$$

$$\therefore \text{C.E.} = 0.19$$



Table 11-3

Flow Damage in Various Fluids

<u>Type of Fluid</u>	<u>Wall Current</u>	<u>% Flow Reduction from Deposit</u>	<u>Relative Damage</u>
Phosphate Ester	2.0 $\mu$ A	30%	Appreciable* in 2 1/2 hours
SST (Humble WSK-759)	.002 $\mu$ A	0	None in 24 hours
MIL-H-5606	less than .001 $\mu$ A	0	None in 24 hours

\* Damage shown in Fig. 5-2

### 11.3 The Effect of Water Addition

The mechanism by which water added to the fluid reduces damage is not fully understood. However, the data seem to indicate that the mechanism is related to the formation of films. These films were first noticed when the flow decreased with time and finally ceased while using the apparatus of Fig. 5-1 with Skydrol 500A and a .0005" gasket. This decrease was not observed after the Skydrol had been dried by bubbling dry nitrogen through it for several days.

Figure 11-5 shows the decrease of flow and wall current with time as measured in Aerosafe 2300 with the streaming current device of Fig. 7-7.\* The flow rate should vary linearly with the area open to flow, that is, linearly with  $g$  appearing in Eq. 7-12. Equation 7-12, then, predicts that the wall current should go up as the flow drops due to gap closure from film formation, a prediction that is not observed. Evidently, the deposit has an effect other than purely mechanical reduction of flow.

This other effect may be related to the film resistivity as observed in electrolytic cells. Appendix 14.6 describes a measurement which shows the resistivity of the deposit to be about one hundred times that of the fluid. The film may act as an insulator on the metal causing  $J_f$  (see Fig. 7-2) to carry the main portion of the current, thus reducing the wall current,  $J_w$ , available for driving the corrosion. The increase

---

\* The authors wish to thank Joan Schneider of CAD for providing this data.

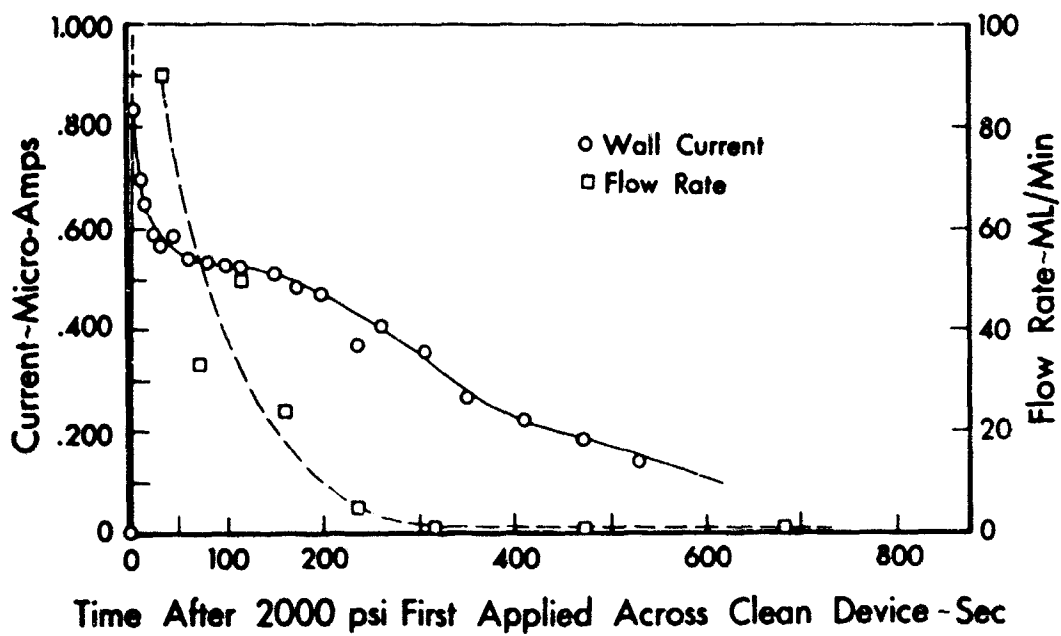


Fig. 11-5. Variation of wall current and flow rate versus time.

of fluid conductivity with water content (Fig. 8-1) would enhance the effectiveness of the film in lowering  $J_w$ .

#### 11.4 Electrochemical Mechanism of Corrosion

A proposed relationship between corrosion of steel and oxidation of other species in phosphate ester fluids is shown in Fig. 11-6. It is based on the electrochemical experiments and high pressure flow experiments and is considered to be a tentative model on which to plan further work.

At low anodic potentials oxidation of species in the fluid occurs according to curve  $i_{ox}$ , beginning at a potential,  $\phi_{ox}$ . There is a limiting current density  $i_{oxL}$  above which another reaction must occur. The value of  $i_{oxL}$  is apparently not determined by a hydrodynamic mass transport limitation because the value appeared to be larger under non-flow conditions than with high shear rates at the wall. For example,  $i_{oxL} \approx 3 \times 10^{-4} \text{ amp/cm}^2$  in the thin electrolyte cell without forced convection (Fig. 9-6), whereas the limiting current density for the initiation of pitting under high shear conditions was  $\approx 3 \times 10^{-6} \text{ amp/cm}^2$  (Fig. 11-4). These data suggest that the white anodic film which adheres to the metal under non-flow conditions may protect the metal from corrosion. At a potential greater than  $\phi_{ox2}$  other oxidation reactions may occur as indicated by the dashed curve.

By analogy to pitting corrosion of iron in aqueous solutions it is proposed that pitting begins at a potential  $\phi_p$  and that the current density increases rapidly with potential. The pitting potential is related to halide ion concentration in aqueous solutions and analogous behavior

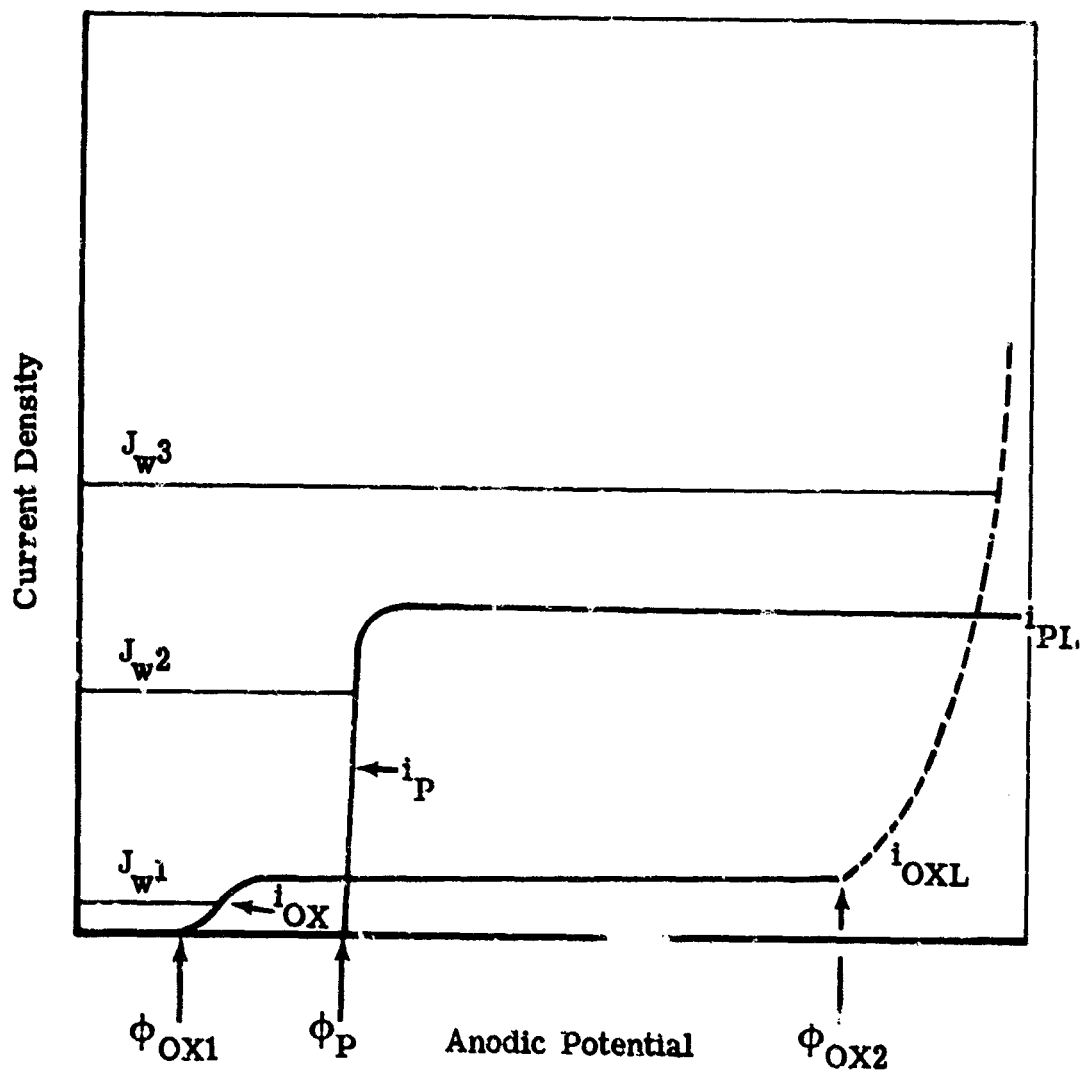


Fig. 11-6. Schematic showing proposed relationship between corrosion and oxidation of fluid species.

is proposed for phosphate ester fluids. The data from the 28 1/2 hour high-pressure flow experiment (Fig. 11-4) indicate that there may be a limiting current density for corrosion indicated by  $i_{pL}$ . The electrolysis experiments with purified basestock and with additions of carbon tetrachloride suggest that  $i_{pL}$  is related to the concentration of a chlorine containing species.

This picture of the relationship of corrosion to oxidation of fluid species allows a mathematical expression of the corrosion current density in relation to the wall current density:

$$@ 0 < J_w < i_{oxL}, \quad i_p = 0$$

$$@ i_{oxL} < J_w < i_{pL}, \quad i_p = J_w - i_{oxL}$$

$$@ i_{pL} < J_w, \quad i_p = i_{pL}$$

It is desired to minimize the pitting corrosion current density to minimize valve damage. For this model, the pitting corrosion damage can be decreased by the following means:

1. Decrease  $J_w$ . This might be done by removal of the surface active anionic species that establish the  $\zeta$  potential or by adding a strongly adsorbing neutral species that displaces the anions. There is strong evidence that fuller's earth filtration removes surface active anions. Decreasing the streaming current by addition of strongly adsorbing neutral species is yet to be definitively demonstrated. The wall current density might also be decreased by increased conduction in the fluid (see Appendix 14.6).

2. Increase  $i_{oxL}$ . Addition of hydroquinone prevented pitting in a static electrolysis experiment but the concept is yet to be demonstrated in a high-pressure flow experiment.
3. Decrease  $i_{pL}$ . Purification of basestock by distillation with decrease of chlorine to 2 ppm level eliminated damage in a static electrolysis experiment but it is yet to be tested in a high pressure flow experiment.

### 11.5 Conclusions

The following conclusions were drawn from the high pressure flow experiments designed to test the streaming current-pitting corrosion model of damage.

1. The damage is primarily due to electrochemical pitting corrosion driven by a streaming current. All of the tests that were done support this model.
2. The corrosion profile is consistent with the values of the wall current density predicted by theory.
3. More than adequate current is generated to account for all of damage; the overall current efficiency for corrosion was ~20%.
4. Corrosion of the polished block under flow conditions could be completely eliminated by cathodic protection; the lip which was polarized anodically was corroded much more severely than without polarization by an external source.
5. No damage occurred on a polished  $Al_2O_3$  ceramic block (an insulator) opposite the orifice lip even though this brittle ceramic is more susceptible to cavitation damage.

12.0 ACKNOWLEDGMENT

The authors wish to express their appreciation to many people, both inside and outside The Boeing Company, who were or are associated with the investigation described in this document.

We were first introduced to the problem, through G. Hollingsworth (BSRL) by J. Kirkbride (CAD). The number of people involved precludes listing all by name, but we would like in particular to thank R. Church, C. Hansen, J. Howard and H. Paul, all of CAD.

Also acknowledged are helpful discussions and cooperation with representatives of Chevron Chemical Company, Monsanto Chemical Company, and Stauffer Chemical Company.

Many members of BSRL contributed and among these are T. Hooper, R. Pelloux and W. Smyrl. We also thank D. Botz, R. Fisher, R. Lee and A. Knudson, who helped with many of the experiments, and B. Thomas and R. Burwell who constructed some of the apparatus.



13.0 REFERENCES

1. Boeing document D6-15854-33 TN (A reproduction of General Electric Report R 66 MSD 311, September 27, 1966).
2. W. Hampton, Aircraft Engineering, p. 1, December 1966.
3. J. F. Judge, American Aviation, p. 25, November 11, 1963.
4. S. S. Shu, Proc. First National Congress Appl. Mech., ASME, 1952, pp. 823-825.
5. A. Klinkenberg and J. van der Minne, "Electrostatics in the Petroleum Industry," Elsevier, New York, 1958.
6. G. B. Jeffery, Phil. Mag., Ser. 6, 29, 455 (1915).
7. G. Hamel, Jahresbericht der Deutschen Math. Vereinigung 25, 34 (1916).
8. K. Millsaps and K. Pohlhausen, J. Aero. Sci. 20, 187 (1953).
9. V. G. Levich, "Physicochemical Hydrodynamics," Prentice-Hall, Englewood Cliffs, N. J., 1962.
10. Boeing Design Manual.
11. "Aerosafe 2300," Stauffer Chemical Company, 1968.
12. R. A. Robinson and R. H. Stokes, "Electrolyte Solutions," Butterworth, London, 1959, p. 398.
13. E. A. Moelwyn-Hughes, "Physical Chemistry," 2nd Ed. Pergamon Press, New York, 1961, p. 880.
14. C. R. Wilke and P. Chang, AIChE Journal 1, 264 (1955).
15. M. Jakob, "Heat Transfer," Vol. I, John Wiley, New York, 1949.
16. C. Kaspar, Trans. Electrochem. Soc., 77, 353 (1940).

14.0 APPENDIX14.1 Nomenclature

a	Radius of tube or ionic radius
A	Electrode area
C	Concentration, circumference
d	Electrode spacing
D	Diameter of metering slit
e	Electronic charge
$F(\theta)$	$\theta$ Dependence of V in Jeffrey-Hamel flow
$F'$	$\partial F / \partial \theta$
F	Faradays Number, 96,500 coulombs/equivalent
g	Width of metering slit (gap)
i	Current density
I	Current
J	Current density
$J_f$	Current density from fluid
$J_w$	Current density from metal wall
$J_s$	2D surface current within double layer
k	Boltzmann constant
K	Velocity gradient normal to wall
$K_h$	Hydrolysis constant
$K_i$	Ionization constant
M	Molecular weight
$l$	Length
L	Constant in Eq. 8-10
N	Avogadro's number

P	Fluid pressure
q	Amount of charge
Q	Flow per unit length of metering slit
r	Radial coordinate
R	Gas constant/mole or electrical resistance
s	Dimensionless surface current divergence
t	Thickness of metal removed
T	Absolute temperature
V	Fluid velocity or volume of electrolyte or metal
$\tilde{V}$	Molar volume
x	Cartesian coordinate
y	Cartesian coordinate
z	Valence
$\epsilon$	Fluid dielectric constant, or current efficiency
$\epsilon_0$	Permittivity of free space
$\zeta$	Interface zeta potential
$\theta$	Angular coordinate
$\nu$	Kinematic viscosity
$\rho$	Charge density
$\rho_d$	Density
$\sigma$	Electrical conductivity
$\tau$	Time
	Potential, volts

## Subscripts:

A	Associated species
h	hydrolysis
H	Hydrogen ion
I	Based on current
L	Limiting
m	Measured
OX	Oxidation
p	Phosphate ester, pitting

## 14.2 Errors in the Theory due to Fluid Conductivity

The theoretical results of Sec. 7 are based on the assumption that the diffuse part of the electrical double layer is thin (high fluid conductivity) compared to the hydrodynamic length scales, and that the resistance to current flow in the fluid is high compared to the resistance to flow from the metal to the fluid. Dry phosphate ester fluids have properties consistent with these assumptions. However, other fluids with lower conductivity do not meet the first condition above. A fluid conductivity increase or an increase in the metal to fluid resistance would cause phosphate ester fluids to violate the second condition.

### 14.2.1 Errors due to Low Conductivity

The electrical double layer thickness [5] is given by

$$\delta = \sqrt{\frac{D\epsilon\epsilon_0}{\sigma}} \quad 14-1$$

If  $\delta$  is very small compared to the length scale of variations along a surface, charge conduction and diffusion along the surface will be small compared to conduction and diffusion normal to the surface. If  $\delta$  is not small, a current opposite to the convected streaming current will appear to reduce the surface current  $J_s$  flowing within the double layer. The wall current will then be lower than predicted by Eq. 7-7.

A second error in the same direction arises if  $\delta$  is thick compared to the hydrodynamic boundary layer. The velocity field cannot be represented by  $Ky$  except near the wall. Far from the wall it drops below  $Ky$  and consequently the surface current is reduced by

$$J_s = \int_0^{\delta} \rho v \, dy \quad 14-2$$

is less than the approximate value obtained by substituting  $K_y$  for  $v$  in Eq. 14-2. Again the true wall current is less than predicted by Eq. 7-7.

The boundary layer thickness can be estimated by use of an approximate relation for  $F(\theta)$  good for large Reynolds numbers [8],

$$F/R_o = 3 \tanh^2 \left[ \sqrt{\frac{R_o}{2}} (\alpha - \theta) + \tanh^{-1} \sqrt{\frac{2}{3}} \right] - 2 \quad 14-3$$

where  $\alpha - \theta$  is the angle between the wall and the point in question.

$F/R_o$  comes within a few percent of being one at

$$\alpha - \theta = 3 \sqrt{\frac{R_o}{2}} \quad 14-4$$

If we take this to be the angular boundary layer thickness, the minimum dimension would occur at about  $r = g$ . The hydrodynamic boundary layer thickness is then

$$\delta_H = 3g \sqrt{\frac{R_o}{2}} \quad 14-5$$

For a Reynolds number  $Re = 200$  in the wall current measuring device of Fig. 7-7, the boundary layer thickness is about 1 micron. Calculated values for the electrical double layer thickness for three different fluids are shown in Table 14.1. The double layers in the SST fluid and MIL-H-5606 are thick compared to the hydrodynamic boundary layer consistent with the observed low wall current.

Table 14-1

Diffuse Double Layer Thickness of Three Fluids

Phosphate Ester	$10^{-2}$ microns
SST (Humble WSX 7597)	1 micron
MIL-H-5606	greater than 10 microns

#### 14.2.2 Errors due to High Conductivity

When current paths through the fluid have a lower resistance than paths through the metal and metal-to-fluid interface, the wall current is lowered by a short circuit through the fluid. Equation 7-7 is based on the premise that the paths in the fluid have a very much larger resistance than those in the metal. If the wall current in a phosphate ester fluid is stopped by opening the circuit between the metal slug and ground in the wall current device (Fig. 7-7), about 50 volts appears on the slug. That is, 50 volts is required to drive a conduction current equal to the wall current through the fluid.

If at any point on the wall a voltage of the order of 50 volts is required to drive the wall current across the metal to liquid interface, then conduction through the fluid will lower the wall current below that calculated from Eq. 7-7. Alternatively, if the fluid conductivity were increased sufficiently, a low voltage across the interface would be sufficient to drive an appreciable current through the fluid so that the wall current would again be below that calculated from Eq. 7-7.

From the data of Sec. 9.3 we can estimate the potential drop across the liquid to metal interface to be a few volts at the current densities calculated from Eq. 7-7. If no resistive film formed on the surface, as with very dry phosphate ester fluids, then only a small portion of the current would be shorted out through the liquid. The fluid conductivity would have to be increased by a factor of 10 before a significant wall current reduction would occur.

If a resistive film forms on the surface, as with high water content fluids, then higher voltages would appear. In Sec. 14.6 the voltages



across the films are estimated to be 50 to 500 volts at current densities calculated for the wall current device by Eq. 7-7. Therefore, in wet phosphate ester fluids a significant portion of the current may be conducted through the fluid rather than appearing as wall current so that Eq. 7-7 would predict a wall current higher than observed.

### 14.3 Diffusivity of Charge Carriers in Phosphate Ester Fluids

An estimate of the diffusivity of charge carriers in phosphate ester fluids was needed for calculations. The equation of Wilke and Chang [14] was used:

$$D_{AB} = 7.4 \times 10^{-8} \frac{(\psi_B M_B)^{1/2} T}{\mu V_A^{0.6}} \quad 14-6$$

It was assumed that the predominate charge carrier is an organic ion of the same molecular weight as the phosphate ester. The following values:  $\psi_B = 1$  [14],  $M_B = 266$  (for tributyl phosphate),  $T = 298^\circ\text{K}$ ,  $\mu = 10$  centipoise and  $V_A = M_A/\rho = 266/1$  give  $D_{AB} = 1.06 \times 10^{-6} \text{cm}^2/\text{sec}$ .

### 14.4 Electrolyte Resistance in Cells

The electrolyte resistances in the needle-to-plane cells and the ring-disk electrode system were calculated from the fluid conductivity and cell geometry in order to compare to the slope of the measured voltage-current curves.

#### 14.4.1 Needle-to-Plane Cells

The work required to obtain an exact solution of the Laplace equation for the complex geometry of the cells does not appear justified, so reasonable approximations will be made. The needle-to-plane cell with

epoxy-potted anode (Fig. 9-8) will be considered first. The method of curvilinear squares [15] will be used. Mutually orthogonal equipotential and current flow lines were drawn by trial and error in such a manner that they formed approximately equal sided squares as shown in Fig. 14-1 for the needle-to-plane system. It can be shown that the resistance can be approximated by

$$R_1 = \frac{n}{2\pi\sigma \sum_{i=1}^m \bar{r}_i} \quad 14-7$$

for cylindrical symmetry, where  $\sigma$  = fluid conductivity,  $n$  = number of squares in the direction of flow,  $m$  = number of "flow channels," and  $\bar{r}$  = average radial distance of each "flow channel." For Fig. 14-1 and a conductivity of  $10^{-7} \text{ ohm}^{-1} \text{ cm}^{-1}$  the resistance is  $2 \times 10^7 \text{ ohm}$  compared to 3 to  $4 \times 10^7 \text{ ohm}$  measured for the cell. It may be noted from the spacing of the flow channels that a high current density occurs under the needle and at the periphery of the disk in agreement with the pattern of pitting (Fig. 9-19).

In the needle-to-plane experiments using the polished block (Fig. 9-7) the resistance was lower than calculated above due to conduction from the upper part of the needle to the larger area of the block. This resistance may be approximated by cylindrical conduction [16]

$$R_2 = \frac{1}{2\pi\sigma l} \ln \frac{r_2}{r_1} \quad 14-8$$

The radius of the needle shaft ( $r_1$ ) was  $\sim 0.05 \text{ cm}$  whereas  $r_2$  varied from  $\sim 0.1 \text{ cm}$  at the outer boundary of Fig. 14-1 to  $\sim 2 \text{ cm}$  at the upper part of the needle. The depth of immersion,  $l \approx 0.5 \text{ cm}$ . These values

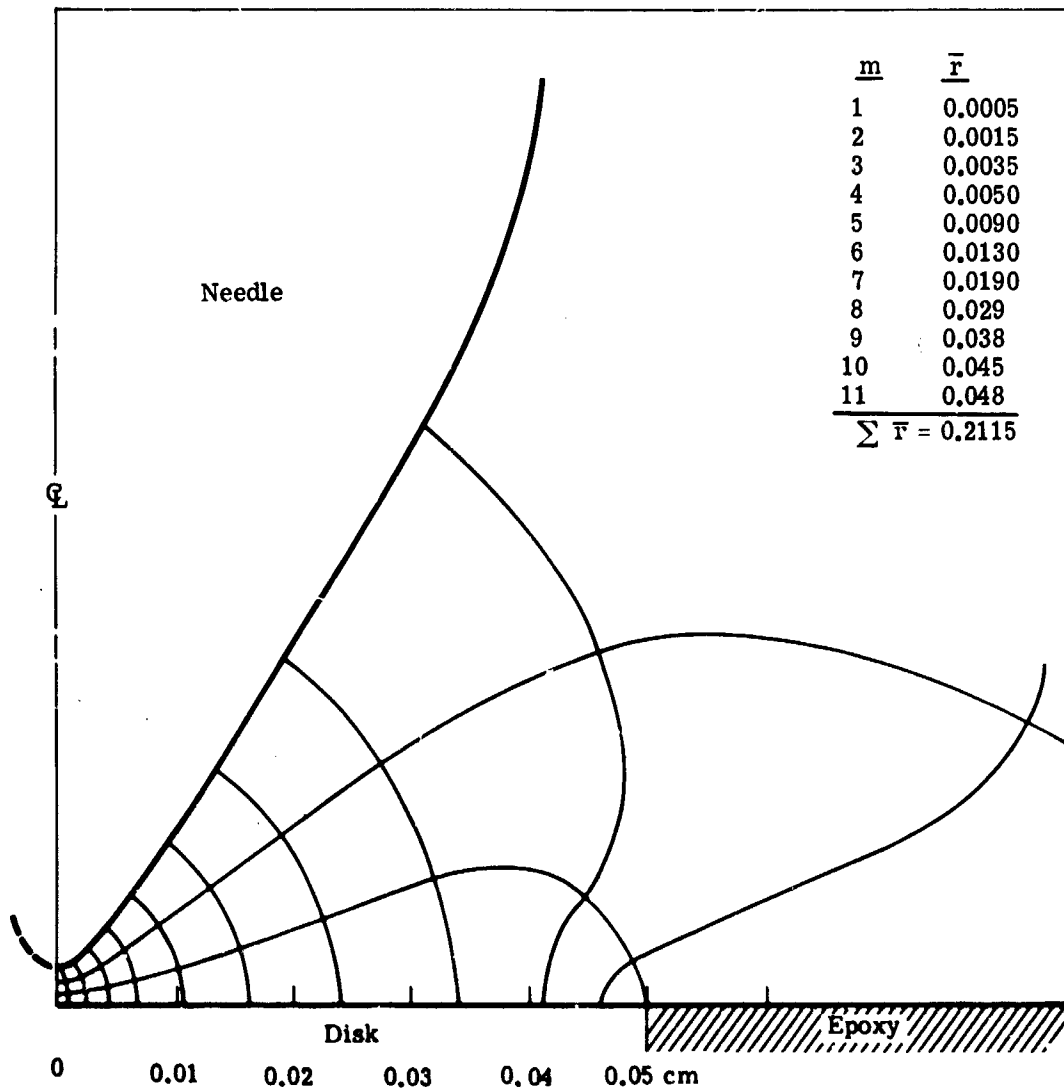


Fig. 14-1. Method of curvilinear squares applied to needle-to-plane cell.

and a conductivity of  $10^{-7} \text{ohm}^{-1} \text{cm}^{-1}$  give  $2.2 \times 10^6$  and  $12 \times 10^6 \text{ohms}$  respectively or an average of  $7 \times 10^6 \text{ohms}$ . The total resistance of the cell would therefore be

$$R_T = \frac{1}{1/R_1 + 1/R_2} \approx 5 \times 10^6 \text{ohms} \quad 14-9$$

compared to  $\sim 6 \times 10^6 \text{ohms}$  measured for Skydrol as shown in Table 9-5.

#### 14.4.2 Ring-disk Electrode System

The geometry of the ring-disk electrode system is shown in Fig. 11-1. Because the circumference of the disk is large compared to the gap it can be treated as a two-dimensional case of current flow for which

$$R = \frac{n}{C\sigma m} \quad 14-10$$

for the method of curvilinear squares. From Fig. 11-1, the circumference of the orifice is  $\sim 0.8 \text{ cm}$  and choosing  $m = 5$  flow channels gives  $n \approx 17$  series squares by the method of curvilinear squares and  $R \approx 4 \times 10^7 \text{ohm}$  compared to  $\sim 2 \times 10^7 \text{ohm}$  measured at no flow (Fig. 11-2).

#### 14.5 Measurement of Corrosion Profile from 28 1/2 hour Run

An average profile of the corroded ring on the polished block from the 28 1/2 hour run was measured in order to determine current density distribution and to estimate current efficiency for corrosion (Sec. 11.2.1). Figure 14-2 shows the approximate position of the lip and the traverses made with the Talysurf Model 3 instrument in respect to the corroded ring. Eight traverses were made with the diamond stylus giving

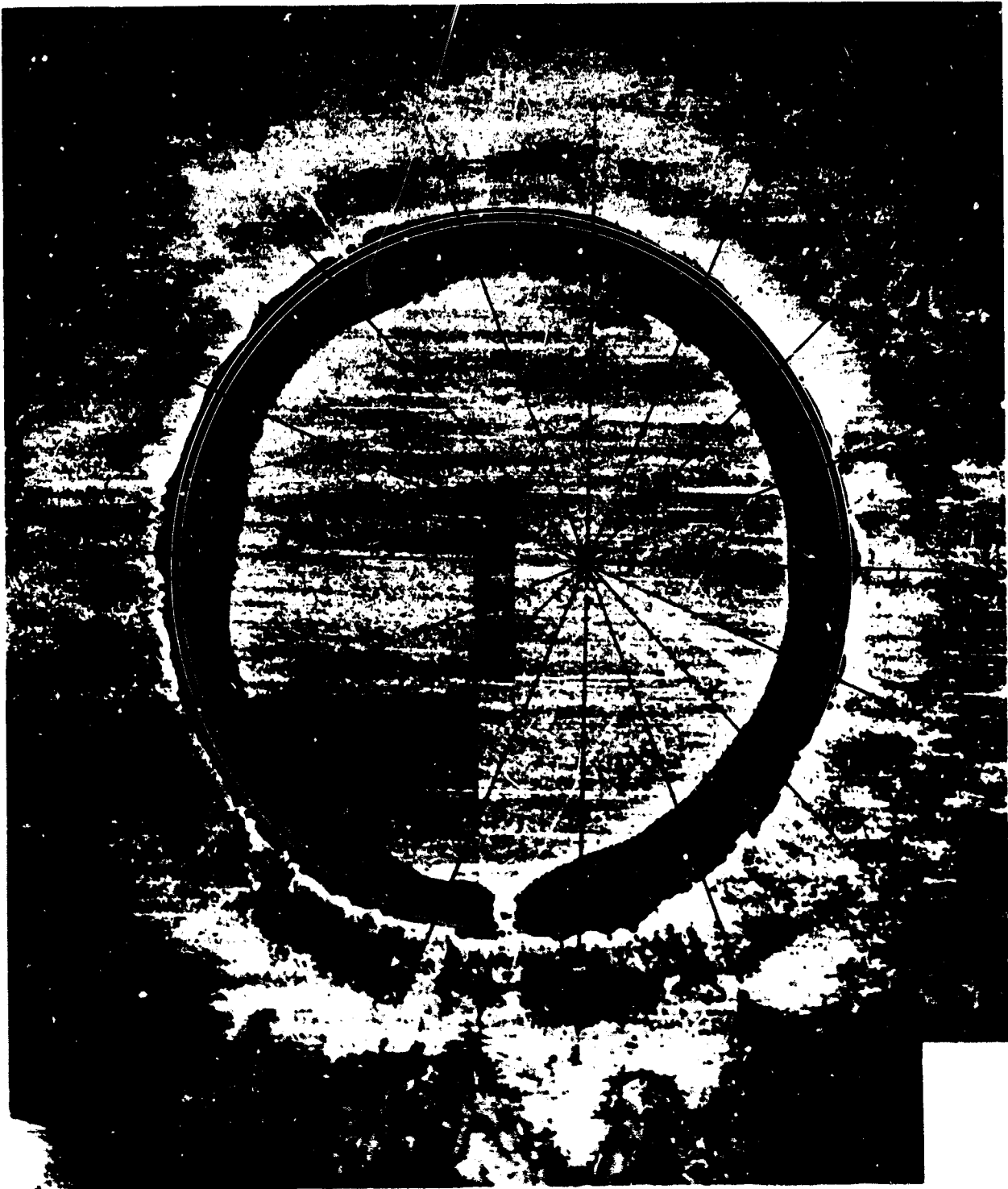


Fig. 14-2. Position of lip and traverses with Talysurf in respect to corroded ring from 28 1/2 hour run.

sixteen profiles  $22\frac{1}{2}$  degrees apart. The stylus was a pyramid with  $90^\circ$  included angle and  $2\frac{1}{2}$  micron flat at the tip. Comparison of the measured profiles to the photomicrograph indicated that the center of rotation for the measurements was slightly eccentric to the ring, but this should cause little error in the average profile.

A typical profile (traverse #7) is shown in Fig. 14-3. Each traverse was divided into 25 micron intervals and the average depth was measured at each interval on the profile and listed in Table 14-2. The profile measurement was started in each case at the outer edge of the corroded zone. (The exact positions of the lip and the traverses were not known accurately enough to scale the position from Fig. 14-2.) This technique caused some error in the final average curve but there appeared to be no better way. The average profile and cross section were determined as shown in Table 14-2. A measurement of the average distance on the sixteen profiles from the inner edge of the lip to the outer boundary of the corroded ring gave approximately 50 microns as shown in Fig. 11-3 in the text.

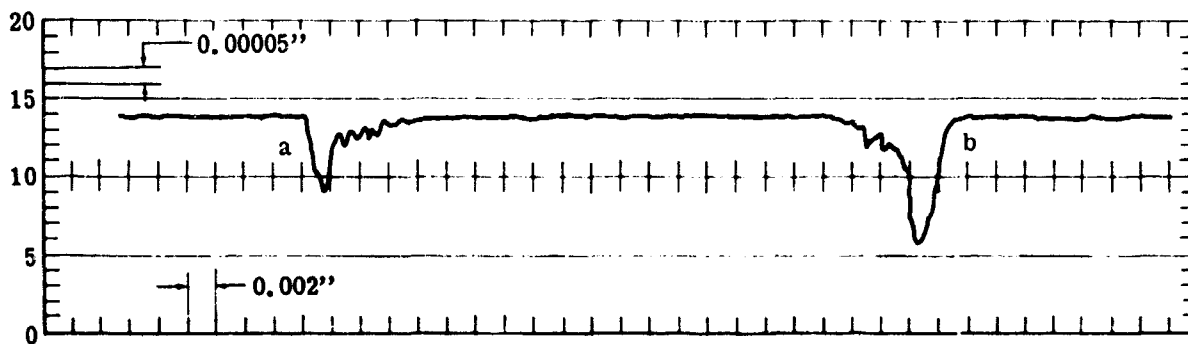


Fig. 14-3. Typical profile (traverse #7) measured with Talysurf instrument.

Table 14-2

Computation of Average Profile

Trace	Position From Edge Microns											$\Sigma$
	0	25	50	75	100	125	150	175	200	225	250	
1a	4.5	4.5	3.7	3.1	1.8	0.9	0.4	0.3	0.1	-	-	
b	2.2	8.5	12.8	14.3	9.2	1.4	0.7	1.3	0.9	0.1	-	
2a	2.4	3.0	1.5	2.0	1.8	1.0	0.3	0.1	-	-	-	
b	2.2	7.6	9.4	9.1	4.5	0.8	1.8	0.6	0.5	0.1	-	
3a	2.3	3.3	2.6	1.9	1.2	0.6	0.7	0.4	0.1	-	-	
b	0.5	2.3	6.0	5.8	2.0	1.6	1.5	0.6	0.2	-	-	
4a	3.1	4.2	2.0	1.3	1.4	0.7	0.4	0.3	0.1	-	-	
b	2.6	6.7	9.0	4.4	1.5	1.0	0.8	0.5	0.1	-	-	
5a	3.0	8.5	8.3	4.6	2.6	1.8	1.7	1.2	0.8	0.1	-	
b	1.7	3.7	3.3	2.0	2.0	1.0	0.5	0.6	0.1	-	-	
6a	1.7	3.1	1.3	0.8	1.0	1.2	0.2	-	-	-	-	
b	1.1	3.7	3.8	2.2	0.9	1.2	0.3	0.1	-	-	-	
7a	2.2	3.3	1.5	1.2	1.0	0.5	0.3	0.1	-	-	-	
b	1.4	6.5	7.0	2.5	1.8	1.6	0.7	0.4	0.1	-	-	
8a	3.6	5.7	3.0	1.5	0.8	1.2	0.5	0.2	-	-	-	
b	2.1	5.8	6.0	3.6	4.1	2.0	0.3	0.2	-	-	-	
Avg.	2.28	5.02	5.06	3.76	2.35	1.15	0.69	0.43	0.19	0.04	-	

Avg.

depth in

Microns 2.86 6.27 6.35 4.70 2.94 1.45 0.87 0.54 0.23 0.05 26.26

$$\text{Average cross section} = (26.26 \times 10^{-4}) (25 \times 10^{-4})$$

$$= 6.57 \times 10^{-6} \text{ cm}^2$$



#### 14.6 Electrode Film Resistivity and Growth Rate

Reported problems of deposits formed in airplane hydraulic systems using phosphate ester fluids with added water suggested making a further analysis of electrochemical growth of films. A further study became particularly pertinent when it was realized that these films may play a role in limiting the amount of damage occurring.

##### 14.6.1 Resistivity of Anode Film

In Fig. 9-5 of the text it is observed that the electrodes with films gave about three times as high a cell potential as the cleaned electrodes for a given current. The resistance of the electrode films was therefore about twice the electrolyte resistance, assuming that the deposit resistance and electrolyte resistance are in series, i.e.,

$$R_T = R_f + R_e \quad 14-11$$

and

$$R_f = 2R_e \quad 14-12$$

It will be assumed that all of the film resistance can be attributed to the anode deposit in the form of a uniform film of thickness,  $t$ .

$$\frac{t}{\sigma_f A} = 2 \frac{d}{\sigma_e A}$$

or

$$\sigma_f = \frac{\sigma_e t}{2d} \quad 14-13$$

The anode film thickness can be estimated from

$$t = \frac{W}{\rho_d A} \quad 14-14$$

Using the values (see Sec. 9.1):  $W = 0.135 \text{ gm}$ ,  $\rho_d = 1 \text{ gm/cm}^3$ ,  $A = 24 \text{ cm}^2$ ,  $d = 0.3 \text{ cm}$  and  $\sigma_e = 10^{-7} \text{ ohm}^{-1} \text{ cm}^{-1}$  gives from Eqs. 14-13 and 14-14 that  $\sigma_f \approx 10^{-9} \text{ ohm}^{-1} \text{ cm}^{-1}$ . The anode film conductivity thus appears to be about a factor of one hundred smaller than the fluid conductivity (for experiment No. 5 in Table 9-1).

#### 14.6.2 Film Growth Rate

Having a film conductivity allows an analysis of the decrease in cell current with time observed in Fig. 9-4. The film growth rate can be expressed as

$$\frac{dt}{d\tau} = \frac{IM}{zF\rho_d A} c_f \quad 14-15$$

where  $c_f$  is the current efficiency for film deposition. The current through the cell can also be expressed as

$$I = \frac{\phi}{t/\sigma_f A + d/\sigma_e A} \quad 14-16$$

from which, if  $d \gg t$ ,

$$\frac{dt}{d\tau} = - \frac{\phi A \sigma_f}{I^2} \frac{dI}{d\tau} \quad 14-17$$

The initial decrease in current with time can be obtained from Fig.

9-4

$$\left( \frac{dI}{d\tau} \right)_{\tau=0} = S_1 \frac{I_1^2}{V} \quad 14-18$$

where  $S_1$  is the initial slope, i.e.,

$$S_1 = \left( \frac{d(I/I_1)}{d\left(\frac{I_1 \tau}{V}\right)} \right)_{\tau=0} \quad 14-19$$

Combining Eq. 14-17 for the initial growth rate with Eq. 14-18 gives

$$\left( \frac{dt}{d\tau} \right)_{\tau=0} = - \frac{\phi A \sigma_f}{V} S_1 \quad 14-20$$

The film growth rates calculated from Eqs. 14-15 and 14-20 are compared in Table 14-3. The film growth rate determined from the initial rate of decrease in current and Eq. 14-20 is seen to be within a factor of 8 larger to a factor of 16 smaller than the value calculated from Eq. 14-15. This is perhaps not unreasonable in view of the uncertainties in the value of some of the parameters. For example, the ratio of the film growth rate of Eq. 14-20 to Eq. 14-15 is

$$R_1 \equiv \frac{(dt/d\tau) \text{ Eq. 14-20}}{(dt/d\tau) \text{ Eq. 14-15}} = \left[ \frac{\phi A^2 S_1 z^2 \rho_d}{V I_1} \right] \left[ \frac{\sigma_f}{M \epsilon_f} \right] \quad 14-21$$

The terms that are known with reasonable accuracy are grouped in the first brackets and the terms that are less accurately known are grouped in the second brackets. If the current efficiency for deposition was constant at 2% throughout experiment No. 5 (curve 4, Fig. 9-4) the value of the  $R_1$  would be 3 instead of 0.06. A value of  $R_1$  larger than unity as for experiment No. 1 suggests either that the actual film conductivity is smaller than assumed or that the molecular weight of the deposited species is larger than assumed.

Table 14-3

Comparison of Film Growth Rates from

Eqs. 14-15 and 14-20

Curve (Fig. 9-4)	1	3	4
Experiment No.	1	4	5
$I_1$ , amps	$3 \times 10^{-4}$	$9 \times 10^{-5}$	$2 \times 10^{-3}$
$\phi$ , volts	100	500	500
$A$ , $\text{cm}^2$	0.7	1.7	24
$V$ , $\text{cm}^3$	$2 \times 10^{-2}$	70	850
$S_1$ , $\text{cm}^3/\text{coul}$	-2	-2	-0.8
$(dt/d\tau)_{\tau=0}$ , cm/sec (Eq. 14-20)	$7.0 \times 10^{-6}$	$2.5 \times 10^{-8}$	$1.1 \times 10^{-8}$
$(dt/d\tau)_{\tau=0}$ , cm/sec (Eq. 14-15)*	$8.6 \times 10^{-7}$	$1.1 \times 10^{-7}$	$1.7 \times 10^{-7}$
$\frac{(dt/d\tau) \text{ Eq. 14-20}}{(dt/d\tau) \text{ Eq. 14-15}}$	8	0.23	0.06
$i_1 = I_1/A$ , amp/ $\text{cm}^2$	$4 \times 10^{-4}$	$5 \times 10^{-5}$	$8.5 \times 10^{-5}$

\* for  $M = 200$ ,  $z = 10$ ,  $F = 10$ ,  $\rho_d = 1$  and  $\epsilon_f = 1$ .

### 14.6.3 Time to Plug Orifice Gap by Film Growth

The time to grow a film thick enough to block the gap in the wear apparatus at a constant initial wall current density is approximately

$$\tau_p = \frac{g}{(dt/d\tau)_1} = \frac{gzF\rho_d\epsilon_f}{iM} \quad 14-22$$

Assuming  $g = 2.5 \times 10^{-3}$  cm (one mil gap),  $z = 1$ ,  $\rho_d = 1$  gm/cm<sup>3</sup>,  $\epsilon_f = 1.0$ ,  $i = 10^{-3}$  amp/cm<sup>2</sup> (see Fig. 11-4) and  $M \approx 200$  gm/mole gives  $\tau_p \approx 20$  minutes. This is within a factor of 10 of the value estimated from the initial decrease in flow rate observed in experiments (see Fig. 11-5).

### 14.6.4 Potential Drop Through Film Near Orifice

The potential drop normal to the wall in the anode film in the vicinity of the orifice is

$$\Delta\phi_f = \frac{it}{\sigma_f} \quad 14-23$$

For a corrosion current density of  $\sim 2 \times 10^{-4}$  amp/cm<sup>2</sup> under the film (see Fig. 11-4), a film conductivity of  $10^{-10}$  to  $10^{-9}$  ohm<sup>-1</sup>cm<sup>-1</sup> and a film thickness of  $2.5 \times 10^{-4}$  cm (assuming 1/10 of the gap width), gives  $\Delta\phi_f = 50$  to 500 volts. A corresponding potential drop which must occur in the fluid in the direction of flow is of the same magnitude as the open-circuit potential drop measured with the ring-disk electrodes (Sec. 11.1). The significance of this finding is that the film growth and increased fluid conductivity may decrease the wall current and thus corrosion. This probably explains the large deviation from theory observed in the corrosion rate near the gap in Fig. 11-4. It may also explain the effect of water addition which both increases the tendency to film formation and increases fluid conductivity.

#### 14.7 High Pressure Flow System

All high pressure experiments were performed with the apparatus shown schematically in Fig. 14-4 or minor variations of it. The fluid temperature was held near room temperature by a cooling coil wound on the muffler for the pump. The cooling was provided by the cold air exhausted from the pump. An accumulator reduced pressure pulsations to about 20 psi. The flow damage apparatus was installed in the position of the wall current drive shown in the schematic. No flow meter was used, but a rough indication of flow rate was provided by measuring the period of the pump pulsation. More accurate flow data were obtained by measuring the time to fill a graduate to a fixed level.

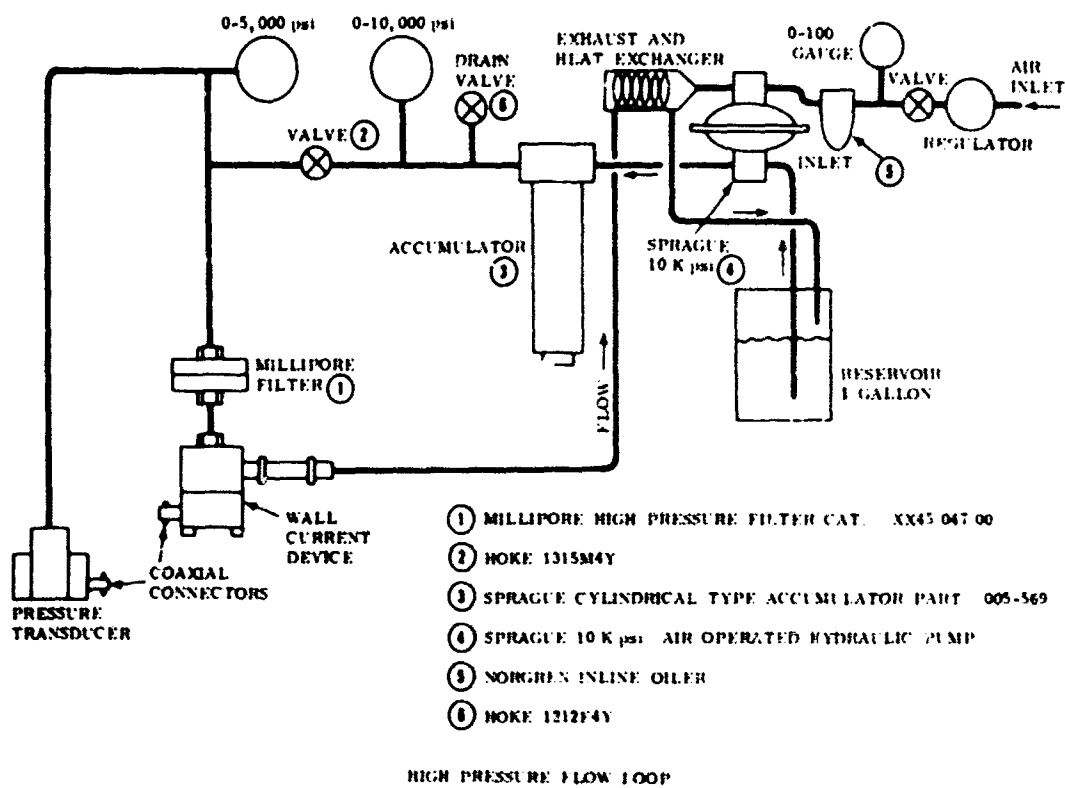


Fig. 14-4. High pressure flow system.